Microparticle Dynamics in Strongly Magnetized Low Temperature Plasmas

by

Brian Robert Lynch Jr.

A dissertation submitted to the Graduate Faculty of
Auburn University
in partial fulfillment of the
requirements for the Degree of
Doctor of Philosophy

Auburn, Alabama
August 5, 2017

Keywords: complex/dusty plasma, dust charge, plasma drift

Approved by

Uwe Konopka, Associate Professor of Physics
Edward Thomas, Professor of Physics
Marcelo Kuroda, Assistant Professor of Physics
Gregory Hartwell, Associate Research Professor of Physics

Abstract

Dusty plasma systems consist of charged microparticles (usually called dust grains) embedded in a background plasma. The dust component can significantly modify the background plasma by collecting electrons and ions, thus modifying the plasma density and the local electrostatic potential. Similarly, due to their net electric charge, the dust grains also respond to local perturbations in the background plasma. In this way, the behavior of the dust grains and the background plasma are closely coupled with each other. The vast majority of experimental dusty plasma studies have been performed under conditions where there is no magnetic field. However, in many plasma systems — particularly fusion and astrophysical plasmas, magnetic fields play a crucial role. Therefore, in recent years there has been an increased effort to study modifications to dusty plasma systems under the influence of large external magnetic fields. Modifications of the dust component may manifest themselves directly as guiding center drifts or indirectly by altering the background plasma and dust grain charging processes.

In this dissertation, the dust grain $\mathbf{g} \times \mathbf{B}$ drift magnetization effect was directly observed using the Magnetized Dusty Plasma Experiment (MDPX) device. The MDPX device was rotated to a horizontal configuration so that the magnetic and the gravitational fields were oriented perpendicular to each other. Dust grain $\mathbf{g} \times \mathbf{B}$ drift motion in a radio-frequency (RF) plasma bulk several centimeters away from any space charge sheaths was then observed and used to calculate the dust grain charge. It was found that the calculated dust grain charge was much smaller than the estimates obtained by extrapolating from situations where the background plasma was unmagnetized. The large reduction in the dust grain charge is believed to be due to the onset of strong electron magnetization where the electron Larmor radii become comparable to the dust grain diameter. In this situation, the electron charging current to the grain becomes flux-tube limited whereas the ion charging current remains relatively unaffected. The measurements performed in this dissertation are a large step forward in understanding the nature of dust grain charging in strongly magnetized plasmas and lay a substantial experimental framework for future theoretical studies.

Acknowledgments

In no particular order, I would like to thank the following people: My advisors, Edward Thomas and Uwe Konopka, for being a constant source of both inspiration and frustration. Robert Merlino and Marlene Rosenberg for their insightful suggestions. My committee members for taking time away from their research specialties to provide invaluable feedback on this project. Darrick Artis for his extreme patience when dealing with mysteriously broken lab equipment. David Patrick for his sanity checks. Patrick Stringer for teaching me to machine my own experiment hardware and letting me learn the hard way — by remaking components. Daniel King for being an outstanding mentor and friend. Ivan Arnold for just being Ivan. Spencer LeBlanc for his (mostly welcomed) distractions in the office and his wife, Maggie Abeyta, for her assistance editing this dissertation.

I would like to thank my family: My father, Brian Lynch Sr., for letting me leave academic high school and make my own mistakes — just to teach me the value of a hard day's work. My mother, Bette Lynch, for always finding a way to look on the bright side. My brother, Dan Lynch, for his "just suck it up" attitude. Brian Goodhue, for encouraging my young 18-year-old, knucklehead self to quit working construction and go back to school.

Most of all, I would like to thank my wife, Kate Lynch, for her support and encouragement. I cannot imagine what my life would be like if I had not met her five years ago and somehow tricked her into marrying me. My son, Chandler Lynch, for not only being a constant source of fun and laughter, but also the sleepless nights that helped prepare me for writing this dissertation. And, last but not least, my German Shepherd dog, Brenda, for making sure that no hamburger is ever forgotten on the kitchen counter.

Table of Contents

List of Figures

List of Tables

List of Abbreviations and Constants

MDPX	The Magnetized Dusty Plasma Experiment
CoPlA	The Complex Plasma Analysis Software
ODE	Ordinary Differential Equation
MHD	Magnetohydrodynamics
OML	Orbit motion limited
FPS	Frames per second
RF	Radio-frequency
RHS	Right-hand side
LHS	Left-hand side
ID	Inner diameter
OD	Outer diameter
GB	Gigabyte
TB	Terabyte
m_{s}	Mass of plasma species s
I_{s}	Current of plasma species s
ρ_{s}	Mass density of plasma species s
n_{s}	Number density of plasma species s

q_{s}	Charge of plasma species s
μ_{s}	Mobility of plasma species s
λ_{s}	Mean free path of plasma species s
$k_{\mathrm{B}}T_{\mathrm{s}}$	Temperature of plasma species s
$v_{\mathrm{th,s}}$	Thermal speed of plasma species s
$r_{\mathrm{L,s}}$	Larmor radius of plasma species s
Z_{d}	Number of electrons on a dust grain
a_{d}	Dust grain radius
$\mathbf{E}$	Electric field
$\mathbf{B}$	Magnetic field
$g = 9.8\ \mathrm{m/s^2}$	Earth's gravitational acceleration
$k_{\mathrm{B}}T = 0.025\ \mathrm{eV}$	Room temperature in eV
$\sigma_{\mathrm{e,n}} \approx 4.0 \cdot 10^{-20}\ \mathrm{m}^2$	$k_{\mathrm{B}}T_{\mathrm{e}} = 2\ \mathrm{eV}$ electron - neutral collision cross section from [1, 2, 3]
$\sigma_{\mathrm{i,n}} \approx 1.0 \cdot 10^{-18}\ \mathrm{m}^2$	$k_{\mathrm{B}}T_{\mathrm{i}} = 0.025\ \mathrm{eV}$ ion - neutral collision cross section from [1, 2, 4]

Chapter 1

Introduction

1.1 Motivation and scope

Dusty plasmas are four-component plasmas consisting of not only the usual microscopic plasma components (i.e., the electrons, ions, and neutral particles), but also a fourth micron-sized dust component. Because the dust component (usually called "grains") is subject to collisions with the ambient plasma, the dust grains can collect a large amount of electric charge. In most low-temperature laboratory plasmas, the dust grains usually obtain a net negative charge due to the higher mobility of electrons compared to ions.

The dynamics of dusty plasmas are typically categorized based on the ratio of the electrostatic to the kinetic energy of the system. Based on this ratio, the dynamical behavior ranges from displaying weakly-coupled collective effects such as waves and fluid-like behavior to displaying strongly-coupled effects such as phase transitions and crystal structure formation where the inter-dust Coulombic interactions dominate. Due to this wide variety of dynamical behavior, dusty plasmas provide a unique testing ground to study multi-particle systems on timescales that can often be observed with the naked eye (milliseconds to seconds). Furthermore, in both the weakly- and the strongly-coupled limits, the addition of a magnetic field significantly changes the behavior of the system. The magnetic field not only acts directly on the dust grains via the magnetic force but also significantly modifies the dynamics of the electrons and ions. In this way, it is important to study the coupling between the dust, the microscopic plasma components, and the magnetic field.

Dusty plasmas span a wide range of length scales and scope. The largest scale at which dusty plasma systems have been observed, is perhaps, the largest length scale possible — astrophysical scales on the order of many thousands of light years. Dust permeates the interstellar medium and absorbs photons, thus providing a degree of opacity for the light emitted from distant galaxies and stars [5, 6]. It has also been shown that magnetic fields play a strong role in star formation within galactic dust clouds [7] and even planet formation through the growth of agglomerate dust grains [8, 9]. Dusty plasmas are also a major component of Saturn's rings [10] and circulating dust has also been observed in the exosphere of the Earth's moon [11, 12]. Dust within our solar system is also known to disrupt spacecraft operation [13, 14]. Even closer to the ground, although not a dusty plasma in a rigorous sense, [15] measured the charge to mass ratio of individual blowing snow particles by observing snow deflection in an externally applied electric field. They observed that individual snow flakes with a size of approximately 200 μm may obtain both negative and positive charge to mass ratios between -200 μC/kg and 70 μC/kg.

In laboratory experiments, the dust is seen mainly as a contaminant in high temperature thermonuclear fusion plasma experiments where dust grains can be ablated from plasma-facing material within the device [16, 17]. In industrial applications, dust grains can nucleate (i.e., "grow") from the constituent gas and contaminate the thin-films used in integrated circuit processing [18] and magnetron etching [19]. In fact, methods have been devised specifically to remove the nuisance dust grains from plasma processing reactors to improve production yield [20, 21].

Regardless of the scale and specific application of dusty plasmas, the driving factor behind most dusty plasma phenomena is the fact that a substantial charge can reside on the dust grain surface. In the case of laboratory dusty plasmas, the net charge can reach several thousand electrons for a single 1 μm diameter dust grain. Despite the extreme importance of the dust grain charge, its measurement is a notoriously difficult task. This dissertation takes on that task by directly observing the so-called $\mathbf{g} \times \mathbf{B}$ magnetization effect on the dust grains to obtain a measurement of the dust grain charge. As a segue into the details of dust grain charging and magnetization effects, a brief review of basic plasma and dusty plasma physics phenomena is provided in the following discussion.

1.2 Plasma and dust characteristics

1.2.1 Quasi-neutrality

In most areas of plasma physics, the plasma is typically treated as being macroscopically quasi-neutral — meaning that there is no large scale separation of electric charge and thus no electric fields are present. The quasi-neutrality condition can be expressed as

$$\sum_{s} n_{\mathrm{s}} q_{\mathrm{s}} = 0 \tag{1.1}$$

where s is used to denote a particular plasma species, n_{s} is the number density, and q_{s} is the charge. Qualitatively, Eq. (1.1) is simply a statement that charged plasma particles are free to move and rearrange in response to the presence of electric fields. For example, the introduction of a charged test particle into an otherwise quasi-neutral plasma will causes a slight displacement of the electrons and ions in the vicinity of the test particle. In the case of a negatively charged test particle, the electrons are repelled leaving behind a positive space charge region. On large length scales, the positive space charge region will exactly cancel the negative charge of the test particle — thus shielding far away plasma particles from the electric field of the test particle. This shielding effect is called Debye shielding and is discussed in more detail in Sec. (1.2.2).

In the context of dusty plasmas, the test particle is a charged dust grain, and the quasi-neutrality condition is given by

$$\sum_{s} n_{\mathrm{s}} q_{\mathrm{s}} = -n_{\mathrm{e}} e + n_{\mathrm{i}} e + n_{\mathrm{d}} q_{\mathrm{d}} = 0 \tag{1.2}$$

where n_{e} is the electron density, e is the electronic charge, n_{i} is the ion number density, q_{d} is the dust grain charge, and n_{d} is the dust number density where $n_{\mathrm{d}} = \delta(\mathbf{r})$ for an isolated grain located at the origin. In most laboratory plasmas, $q_{\mathrm{d}} < 0$ due to the much higher thermal speed of electrons compared to ions. A common expression that is used to account for the negative charge of a dust grain is

$$q_{\mathrm{d}} = -eZ_{\mathrm{d}} \tag{1.3}$$

where Z_{d} is a dimensionless positive integer.

1.2.2 Debye shielding

In this section, the derivation of a well known result for the shielding length of an isolated dust grain [22, 23] is reviewed. The shielding length can be obtained by considering the following Poisson's equation for the electrons, ions, and dust:

$$\nabla^2 \Phi = \frac{-e}{\epsilon_{\mathrm{o}}} \left(-n_{\mathrm{e}} + n_{\mathrm{i}} - Z_{\mathrm{d}} n_{\mathrm{d}}\right) \tag{1.4}$$

where Φ is the electrostatic potential and ϵ_{o} is the permitivity of free space. It is also assumed that the electrons and ions each obey the Boltzmann relation

$$n_{\mathrm{s}} = n_{\mathrm{s,o}} \exp\left(-\frac{q_{\mathrm{s}}\Phi}{k_{\mathrm{b}} T_{\mathrm{s}}}\right) \tag{1.5}$$

where k_{b} is Boltzmann's constant and T_{s} is the temperature of plasma species s. In the limiting case where $k_{\mathrm{b}} T_{\mathrm{s}} \gg |q_{\mathrm{s}}\Phi|$, Eq. (1.5) simplifies to

$$n_{\mathrm{s}} \approx n_{\mathrm{s,o}} \left(1 - \frac{q_{\mathrm{s}}\Phi}{k_{\mathrm{b}} T_{\mathrm{s}}}\right), \tag{1.6}$$

which is the linearized density for the electrons and ions. However, it is important to note that the assumption $k_{\mathrm{b}} T_{\mathrm{s}} \gg |q_{\mathrm{s}}\Phi|$ does not apply in the region of space close to the grain. In order to take this into account, it is necessary to apply the Vlasov description of plasmas [24] where it is shown that the electron density stills obeys the Boltzmann relation of Eq. (1.5); however, the ion density is significantly modified and the resulting Poisson's equation is highly nonlinear. A more detailed discussion of these situations can be found in [25, 26], and in the rest of this section we proceed under the assumption that Eq. (1.6) is valid.

By substituting the quasi-neutrality condition far from the dust grain $Z_{\mathrm{d}} n_{\mathrm{d}} = -n_{\mathrm{e,o}} + n_{\mathrm{i,o}}$ and the linearized Boltzmann equation for the electrons and the ions into Eq. (1.4), we get

$$\nabla^2 \Phi - \left(\frac{e^2 n_{\mathrm{e,o}}}{\epsilon_{\mathrm{o}} k_{\mathrm{b}} T_{\mathrm{e}}} + \frac{e^2 n_{\mathrm{i,o}}}{\epsilon_{\mathrm{o}} k_{\mathrm{b}} T_{\mathrm{i}}} \right) \Phi = 0, \tag{1.7}$$

which is more concisely written as

$$\nabla^2 \Phi - \frac{1}{L_{\mathrm{d}}^2} \Phi = 0, \tag{1.8}$$

where

$$\frac{1}{L_{\mathrm{d}}^2} = \frac{1}{L_{\mathrm{e}}^2} + \frac{1}{L_{\mathrm{i}}^2} \tag{1.9}$$

is the dust grain Debye length and

$$L_{\mathrm{s}}^2 = \frac{\epsilon_{\mathrm{o}} k_{\mathrm{b}} T_{\mathrm{s}}}{e^2 n_{\mathrm{s,o}}} \tag{1.10}$$

is the expression for the Debye length of the electrons and the ions. Eq. (1.8) is the Helmholtz equation with well known solutions [27, 28] of the form

$$\Phi(r) = -\frac{Z_{\mathrm{d}} e}{4\pi\epsilon_{\mathrm{o}} r} \exp\left(-\frac{r}{L_{\mathrm{d}}} \right). \tag{1.11}$$

Eq. (1.11) is often called the Debye potential or the shielded Coulomb potential. When $r \ll L_{\mathrm{d}}$, Eq. (1.11) becomes the usual Coulomb potential, whereas for $r \gg L_{\mathrm{d}}$, the potential decays exponentially. Physically, this means that far from the grain, the positive space charge surrounding the grain will exactly cancel the negative charge of the grain — thus shielding the far away plasma from the local plasma perturbations near the grain. The characteristic spatial dimension of the shielding region is the dust grain Debye length given by Eq. (1.9).

The Debye length is the characteristic length at which plasmas maintain the quasi-neutrality condition, Eq. (1.1).

1.2.3 Hall parameter

In low temperature weakly-ionized plasmas where plasma-neutral collisions dominate, the magnetization of the electrons and the ions is usually quantified according to the Hall parameter. The method for quantifying dust grain magnetization must be handled differently and the discussion is postponed until Sec. (2.1). The electron and ion (denoted with the subscript s) Hall parameter is defined as the ratio of the Larmor frequency to the neutral collision frequency and is given by

$$H_{\mathrm{s}} = \frac{\omega_{\mathrm{c},s}}{\nu_{\mathrm{n},s}} \tag{1.12}$$

where

$$\omega_{\mathrm{c},s} = \frac{q_s B}{m_s} \tag{1.13}$$

is the Larmor frequency, B is the magnetic field strength, m_s is the mass,

$$\nu_{\mathrm{n},s} = \frac{v_{\mathrm{th},s}}{\lambda_{\mathrm{p},s}} \tag{1.14}$$

is the neutral collision frequency,

$$v_{\mathrm{th},s} = \sqrt{\frac{8 k_{\mathrm{b}} T_{\mathrm{s}}}{\pi m_{\mathrm{s}}}} \tag{1.15}$$

is the thermal speed,

$$\lambda_s = \frac{1}{n_s \sigma_s} \tag{1.16}$$

is the mean free path, and σ_s is the scattering cross section between either the electrons or the ions and the neutral species. When the Larmor frequency exceeds the neutral collision frequency such that the Hall parameter exceeds unity, the plasma species is considered magnetized. When a plasma species is magnetized, collisions with neutral particles will, on average, displace the center of the charged particle circular orbit by approximately one

Larmor radius

$$r_{\mathrm{L},s} = \frac{m_s v_{\perp,s}}{q_s B} = \frac{v_{\perp,s}}{\omega_{\mathrm{c},s}} \tag{1.17}$$

where $v_{\perp,s}$ is the velocity perpendicular to the magnetic field. As a result, the perpendicular mean free path of the electrons and ions becomes of the order of the Larmor radius whereas the parallel mean free path remains relatively unchanged.

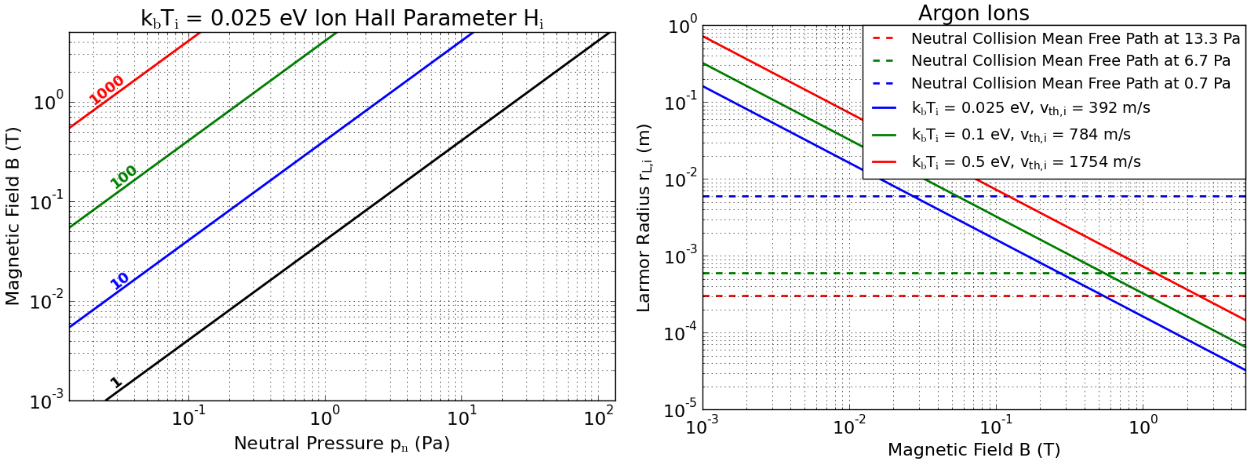

(a) (b)

Figure 1.1: a) Contours of constant Argon ion Hall parameter plotted according to Eq. (1.18) where $k_\mathrm{b}T_\mathrm{i} = 0.025$ eV. b) Argon ion Larmor radius versus magnetic field strength for several values of $k_\mathrm{b}T_\mathrm{i}$.

The Hall parameter is more easily understood when expressed in terms of experimental quantities by substituting the definitions from Eqs. (1.13 – 1.14). The result is

$$H_\mathrm{s} = \frac{q_\mathrm{s} B}{m_\mathrm{s}} \sqrt{\frac{\pi m_\mathrm{s}}{8 k_\mathrm{b} T_\mathrm{s}}} \frac{k_\mathrm{b} T_\mathrm{n}}{p_\mathrm{n}} \frac{1}{\sigma_n} \tag{1.18}$$

where σ_n is the collision cross-section between plasma species s and a neutral particle, T_n is the temperature of neutrals, and p_n is the neutral gas pressure. To magnetize an electron or ion, Eq. (1.18) shows that the neutral gas pressure should be minimized and the magnetic field maximized. A nominal value for the electron-neutral scattering cross-section is taken from [1, 2, 3] as $\sigma_{\mathrm{e,n}} \approx 4.0 \cdot 10^{-20}$ m^2, and the ion-neutral scattering cross-section is taken from [1, 2, 4] as $\sigma_{\mathrm{i,n}} \approx 1.0 \cdot 10^{-18}$ m^2. Several illustrative values for the electron and ion Larmor

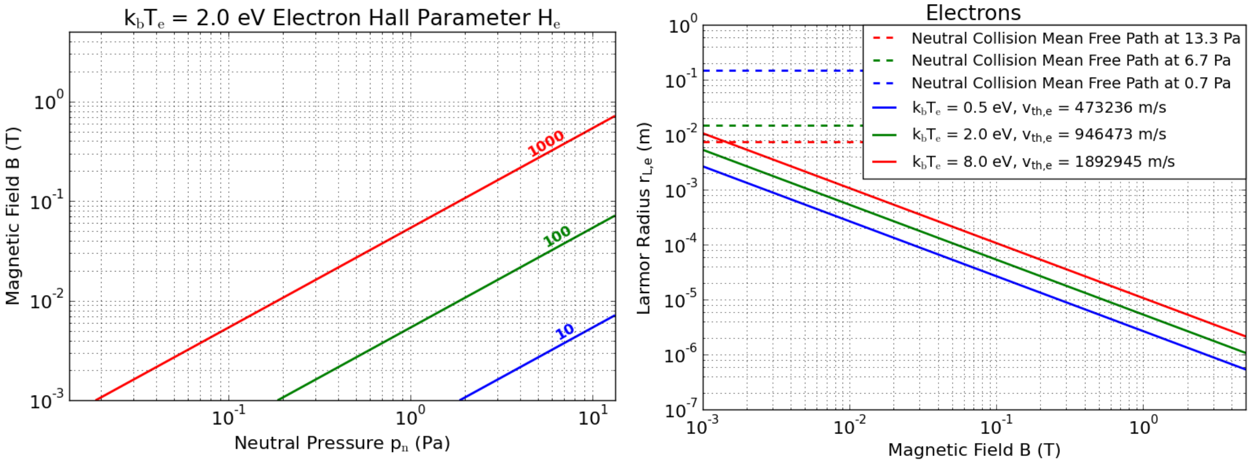

(a) (b)

Figure 1.2: a) Contours of constant electron Hall parameter plotted according to Eq. (1.18) where $k_\mathrm{b}T_\mathrm{e} = 2.0$ eV. The range of neutral pressure p_n shown here is smaller than Fig. (1.1a). b) Electron Larmor radius versus magnetic field strength for several values of $k_\mathrm{b}T_\mathrm{e}$.

radii and Hall parameters under typical experimental conditions are shown in Figs. (1.1 – 1.2).

1.2.4 Coulomb coupling parameter

In dusty plasmas where many dust grains are present, the collective dynamics of the dust component is typically categorized based on the ratio of the electrostatic potential energy E_pot between adjacent grains to the thermal kinetic energy of the grains E_therm. This ratio is called the Coulomb coupling parameter is usually expressed as

$$R_\mathrm{C} = \frac{E_\mathrm{pot}}{E_\mathrm{thermal}} = \frac{e^2 Z_\mathrm{d}^2}{4\pi\epsilon_\mathrm{o} d_\mathrm{d} k_\mathrm{b} T_\mathrm{d}} \exp\left(-\frac{d_\mathrm{d}}{L_\mathrm{d}}\right) \tag{1.19}$$

where T_d is the dust temperature and d_d is the average inter-grain distance. When $R_\mathrm{C} \gg 1$, the electrostatic potential energy of the dust component is much larger than the kinetic energy and the dust motion is dominated by the inter-dust electrostatic interactions. In this state, the system is said to be strongly-coupled. In ground-based laboratory experiments, strongly-coupled systems often exhibit crystalline behavior where the dust grains can self-organize into disc-shaped 2D hexagonal structures that may be vertically stacked as one to a few layers [29, 30]. These crystalline systems often exhibit structure effects such as pattern formation, grain boundaries, and crystal defects [31, 32, 33]. On the other hand, when $R_\mathrm{C} \ll 1$, the inter-dust electrostatic interactions are weak compared to the thermal energy of the system. In this case, the dust is in a more fluid-like state [34, 35] and often exhibits collective dynamic behaviors such as waves [36, 37, 38, 39], streams [40], and shear [41]. The thermodynamic behavior of weakly-coupled systems has also been extensively studied [42, 43, 44, 45, 46, 41].

1.2.5 Forces on dust grains

In this section, the most common forces that act upon dust grains is reviewed according to other discussions commonly found in textbooks such as [22, 23, 47].

Electromagnetic force

The force on a charged moving dust grain in the presence of electric and magnetic fields is

$$\mathbf{F}_\mathrm{E} = q_\mathrm{d}(\mathbf{E} + \mathbf{v} \times \mathbf{B}) \tag{1.20}$$

where q_d is the total charge of the dust grain, $\mathbf{E}$ is the electric field, $\mathbf{v}$ is the velocity of the dust grain, and $\mathbf{B}$ is the magnetic field. The first term on the right hand side (RHS) of Eq. (1.20) is usually referred to as the electrostatic force, and the second term on the RHS is usually referred to as the magnetic force.

Gravitational force

In laboratory dusty plasmas, the gravitational force acting on a dust grain is

$$\mathbf{F}_\mathrm{g} = m_\mathrm{d}\mathbf{g} = \frac{4}{3}\pi a_\mathrm{d}^3 \rho_\mathrm{d}\mathbf{g} \tag{1.21}$$

where m_{d} is the mass of the dust grain, a_{d} is the radius of the grain, ρ_{d} is the mass density of the grain, and $\mathbf{g}$ is the gravitational acceleration ($g = 9.8$ m/s^2) on the Earth's surface. The radius and mass density of dust grains are usually provided by the manufacturer.

Neutral drag force

The neutral gas drag is often treated by the well-known Epstein formulation [48]. The Epstein neutral drag expression is

$$\mathbf{F}_{\mathrm{n}} = -\gamma \mathbf{v} \tag{1.22}$$

where

$$\gamma = \delta \frac{4}{3} \pi a_{\mathrm{d}}^2 m_{\mathrm{n}} v_{\mathrm{th,n}} n_{\mathrm{n}}, \tag{1.23}$$

n_{n} is the number density of neutrals, $v_{\mathrm{th,n}}$ is the thermal speed of neutrals, m_{n} is the mass of an individual neutral atom, and δ is the Epstein coefficient. δ is a dimensionless constant based on the nature of the collisions between the neutral gas atoms and the dust grain. Experiments [49, 50, 42, 51] and theory [48] have shown that typical values for δ are $1 < \delta < 2$.

The Epstein neutral drag model given by Eqs. (1.22 – 1.23) is subject to two constraints: First, the dust grain size must be much smaller than the mean free path, λ_{n}, of neutral gas particles. In most low temperature dusty plasma experiments, a typical neutral Argon gas pressure (on the high end) is $p_{\mathrm{n}} = 66.7$ Pa. This neutral pressure corresponds to a mean free path of $\lambda_{\mathrm{n}} \sim 500$ μm, which is much greater the typical dust grain diameters of $a_{\mathrm{d}} \leq 15$ μm. Second, the dust grain speed must be much smaller than the thermal speed of the neutral gas. A typical dust gain speed is $v_{\mathrm{dust}} \leq 40$ cm/s, which is well below the thermal speed of room temperature neutral Argon gas where $v_{\mathrm{th,n}} \sim 400$ m/s.

The neutral drag coefficient, Eq. (1.23), is not particularly useful in its current form because it is not written in terms of experimentally controllable quantities. To express the neutral drag coefficient in a more useful form, we make the assumption that the neutral gas obeys a Maxwell-Boltzmann velocity distribution and is in thermal equilibrium with the surrounding vacuum chamber. The neutral gas thermal speed is then given by

$$v_{\mathrm{th,n}} = \sqrt{\frac{8k_{\mathrm{b}}T_{\mathrm{n}}}{\pi m_{\mathrm{n}}}}, \tag{1.24}$$

and the number density is given by

$$n_{\mathrm{n}} = \frac{p_{\mathrm{n}}}{k_{\mathrm{b}}T_{\mathrm{n}}}. \tag{1.25}$$

When inserting Eqs. (1.24 – 1.25) into Eq. (1.23), we get

$$\gamma = \delta\frac{4}{3}\pi\sqrt{\frac{8m_{\mathrm{n}}}{\pi k_{\mathrm{b}}T_{\mathrm{n}}}}a_{\mathrm{d}}^2 p_{\mathrm{n}}. \tag{1.26}$$

An alternative expression to Eq. (1.26) is

$$\Gamma = \delta\sqrt{\frac{8m_{\mathrm{n}}}{\pi k_{\mathrm{b}}T_{\mathrm{n}}}}\frac{p_{\mathrm{n}}}{\rho_{\mathrm{d}}a_{\mathrm{d}}} \tag{1.27}$$

where $\Gamma = \gamma/m_{\mathrm{d}}$ is the normalized Epstein drag coefficient. Eqs. (1.26 – 1.27) are now much more useful because they are written in terms of three experimentally controllable quantities: ρ_{d} is the dust mass density (specific to the material composition that is usually specified by the manufacturer), a_{d} is the dust radius (also specified by the dust manufacturer), and p_{n} is the neutral gas pressure.

Ion drag

The ion drag on a dust grain consists of two primary components: the direct impact of ions on the dust grain surface (called the collection drag), and Coulomb scattering collisions (called Coulomb drag). The total ion drag force is the sum of these two terms and is given as

$$\mathbf{F}_{\mathrm{i}} = \mathbf{F}_{\mathrm{i}}^{\mathrm{coll}} + \mathbf{F}_{\mathrm{i}}^{\mathrm{coul}} \tag{1.28}$$

where $\mathbf{F}_{\mathrm{i}}^{\mathrm{coll}}$ is the ion collection drag and $\mathbf{F}_{\mathrm{i}}^{\mathrm{coul}}$ is the ion Coulomb drag. Both of these contributions to the total ion drag have been thoroughly discussed in review articles [52, 53] and measured [54, 55, 56, 57, 58, 59]. Modifications to these models have also been developed [60, 61, 62, 63] to include effects such as long range ion scattering outside the dust Debye sphere.

In most laboratory dusty plasmas, the characteristic dust grain speed is much smaller than the ion thermal and drift speeds. In this case, both types of ion drag can be written concisely as

$$\mathbf{F}_{\mathrm{i}}^{\mathrm{coll,coul}} = n_{\mathrm{i}} m_{\mathrm{i}} \sigma^{\mathrm{coll,Coul}} V_{\mathrm{i}} \mathbf{v}_{\mathrm{i}} \tag{1.29}$$

where n_{i} is the number density of ions, m_{i} is the mass of an ion, $\sigma^{\mathrm{coll,Coul}}$ is the momentum exchange collision cross section, and $V_{\mathrm{i}} = \sqrt{(v_{\mathrm{i}}^2 + v_{\mathrm{th,i}}^2)}$ where v_{i} is the ion drift speed and $v_{\mathrm{th,i}}$ is the ion thermal speed. The collection cross section is given by

$$\sigma^{\mathrm{coll}} = \pi a_{\mathrm{d}}^2 \left(1 - \frac{2e\Phi_{\mathrm{d}}}{m_{\mathrm{i}} v_{\mathrm{i}}^2}\right) \tag{1.30}$$

where Φ_{d} is the electrostatic potential on the dust grain. Eq. (1.30) is derived in the next section while discussing dust grain charging processes. The Coulomb scattering cross section [54] is given by

$$\sigma^{\mathrm{Coul}} = 2\pi b_0^2 \ln\left(\frac{b_0^2 + L_{\mathrm{d}}^2}{b_0^2 + b_{\mathrm{C}}^2}\right) \tag{1.31}$$

where

$$b_0 = a_{\mathrm{d}} \frac{e\Phi_{\mathrm{d}}}{m_{\mathrm{i}} v_{\mathrm{i}}^2} \tag{1.32}$$

is the impact parameter,

$$b_{\mathrm{C}} = a_{\mathrm{d}} \sqrt{\left(1 - \frac{2e\Phi_{\mathrm{d}}}{m_{\mathrm{i}} v_{\mathrm{i}}^2}\right)} \tag{1.33}$$

is the impact distance of a 90 degree scattering event, and L_{d} is the dust Debye length given by Eq. (1.9).

1.3 An overview of dust grain charging

The collection of electrons and ions on the surface of a dust grain is arguably, one of the most important concepts in dusty plasmas. A dust grain immersed in a plasma is subject to both electron and ion currents so that the total current to the dust grain is

$$I_{\mathrm{t}} = I_{\mathrm{e}} + I_{\mathrm{i}} \tag{1.34}$$

where I_{t} is the total current, I_{e} is the electron current, and I_{i} is the ion current. The electron and the ion currents each have two components: a thermal (random) component, and a component that is in response to space charge distributions that may form around the dust grain. Since the electron thermal speed is larger than the ion thermal speed by a factor of approximately 10^3, the electrons are able to reach the dust grain surface much more rapidly than the ions. As a result, the dust grain quickly obtains a net negative charge. As the dust grain becomes more negatively charged, the electron current to the grain is decreased due to the electrostatic repulsion between the plasma electrons and the electrons residing on the dust grain. The ion current to the dust grain is then increased due to the attractive interaction between the positively charged plasma ions and the negatively charged grain. Eventually, the two currents to the grain reach equilibrium such that

$$I_e + I_i = 0. \tag{1.35}$$

In the rest of this chapter, the physics of the electron and ion currents to the grain is reviewed for several different models.

1.3.1 Orbit-motion-limited (OML) charging theory

The most widely used theory of dust grain charging is the Orbit-Motion Limited (OML) charging theory that is derived from the Langmuir probe theory [64, 65] and commonly appears in textbooks on dusty plasmas [22, 23, 47, 66]. The OML charging theory is a continuous model that does not take into account the discrete nature of charging processes. This section provides an introduction to the OML charging theory, its results, and limitations of the OML model.

OML equilibrium charge

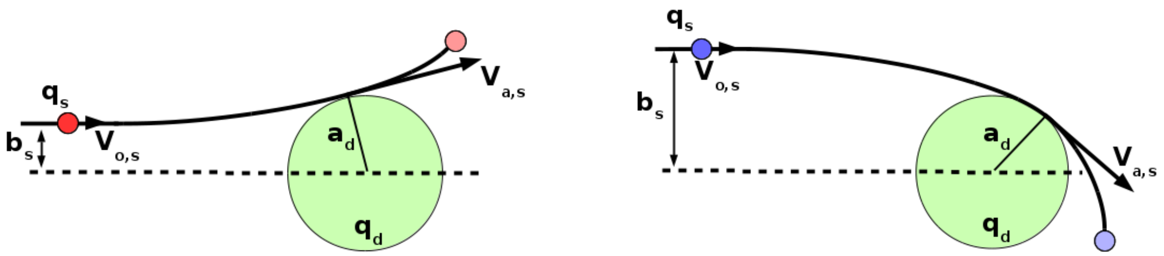

(a) (b)

Figure 1.3: A microscopic plasma particle undergoes a collision with a macroscopic charged dust grain. a) $q_s \Phi_\mathrm{d} > 0$. b) $q_s \Phi_\mathrm{d} < 0$.

Consider the case where an electron or an ion undergoes an electrostatic collision with a negatively charged dust grain as shown in Fig. (1.3). In the OML theory, the details of this electrostatic collision are subject to the following constraints: the grain dimension is much smaller than the electron and the ion mean free paths, there is no ionization in the sheath surrounding the grain, and secondary electrons are not emitted from the grain due to the collision. The angular momentum and energy of the incident particle are conserved during the collision. Conservation of angular momentum can be expressed as

$$m_s v_{\mathrm{o},s} b_\mathrm{s} = m_s v_{\mathrm{a},s} a_\mathrm{d} \tag{1.36}$$

where m_s is the mass of the incident plasma particle, $v_{\mathrm{o},s}$ is the initial speed of the plasma particle at infinity, b_s is the impact parameter, $v_{\mathrm{a},s}$ is the velocity of the incident plasma particle at the point of closest approach, and a_d is the radius of the dust grain. Similarly, applying conservation of energy yields

$$\frac{1}{2}m_s v_{\mathrm{o},s}^2 = \frac{1}{2}m_s v_{\mathrm{a},s}^2 + q_s\Phi_{\mathrm{d}} \tag{1.37}$$

where Φ_{d} is the electrostatic potential of the dust grain. Eqs. (1.36 – 1.37) can be rearranged to solve for the impact parameter b_s so that the collision cross section $\sigma_{\mathrm{d},s}$ is given by

$$\sigma_{\mathrm{d},s} = \pi b_s^2 = \pi a_{\mathrm{d}}^2\left(1 - \frac{2q_s\Phi_{\mathrm{d}}}{m_s v_{\mathrm{o},s}^2}\right). \tag{1.38}$$

The charging current collected by the dust grain can be expressed as

$$I_s = q_s n_s < \sigma_{\mathrm{d},s} v_s > \tag{1.39}$$

where

$$< \sigma_{\mathrm{d},s} v_s > = \left(\frac{m_s}{2\pi k_{\mathrm{b}} T_{\mathrm{s}}}\right)^{\frac{3}{2}} \int_{v_{s,\mathrm{min}}}^{\infty} \sigma_{\mathrm{d},s} v_s f_s(v_s) dv_s, \tag{1.40}$$

$v_{s,\mathrm{min}}$ is the minimum velocity for which the charged plasma particle can hit the dust grain, and

$$f_s(v_s) = 4\pi\left(\frac{m_s}{2\pi k_{\mathrm{b}} T_{\mathrm{s}}}\right)^{\frac{3}{2}} v_s^2 \exp\left(-\frac{m_s v_s^2}{2k_{\mathrm{b}} T_{\mathrm{s}}}\right) \tag{1.41}$$

is the isotropic Maxwellian speed distribution. The minimum velocity with which the ions can hit the grain $v_{i,\mathrm{min}} = 0$ due to the attractive force. Due to the repulsive force between the electrons and the negatively charged grain, $v_{e,\mathrm{min}}$ is non-zero for the electrons and is obtained by applying energy conservation to get

$$v_{e,\mathrm{min}} = \sqrt{\frac{2e|\Phi_{\mathrm{d}}|}{m_e}}. \tag{1.42}$$

Upon carrying out the integration of Eq. (1.40), the electron current to the grain is

$$I_\mathrm{e} = I_\mathrm{o,e} \exp\left(-\frac{e|\Phi_\mathrm{d}|}{k_\mathrm{b} T_\mathrm{e}}\right) \tag{1.43}$$

and the ion current to the grain is

$$I_\mathrm{i} = I_\mathrm{o,i} \left(1 + \frac{e|\Phi_\mathrm{d}|}{k_\mathrm{b} T_\mathrm{i}}\right) \tag{1.44}$$

where $I_\mathrm{o,e}$ and $I_\mathrm{o,i}$ are constant coefficients given by

$$I_\mathrm{o,s} = 4\pi \mathrm{a_d}^2 n_{\mathrm{o},s} q_s \sqrt{\frac{k_\mathrm{b} T_\mathrm{s}}{2\pi m_s}}. \tag{1.45}$$

The absolute value around the $|\phi_\mathrm{d}|$ has been added to ensure the correct sign is used for the electron and ion charging current contributions. Physically, Eq. (1.45) corresponds to the thermal components of the current to the grain when $\Phi_\mathrm{d} = 0$.

By substituting Eqs. (1.43 – 1.45) into Eq. (1.34) and assuming that $n_\mathrm{o,e} = n_\mathrm{o,i} = n_\mathrm{o}$ far from the dust grain, we obtain the following expression for the total charging current:

$$I_\mathrm{t} = 4\pi a_\mathrm{d}^2 n_\mathrm{o} e \sqrt{\frac{k_\mathrm{b} T_\mathrm{e}}{2\pi m_\mathrm{e}}} \left[\sqrt{\frac{m_\mathrm{e} T_\mathrm{i}}{m_\mathrm{i} T_\mathrm{e}}} \left(1 + \frac{e|\Phi_\mathrm{d}|}{k_\mathrm{b} T_\mathrm{i}}\right) - \exp\left(-\frac{e|\Phi_\mathrm{d}|}{k_\mathrm{b} T_\mathrm{e}}\right)\right]. \tag{1.46}$$

At equilibrium, the total current to the grain is zero and Eq. (1.35) applies, which means that the equilibrium charge can be extracted by numerically solving the transcendental equation

$$0 = \sqrt{\frac{m_\mathrm{e} T_\mathrm{i}}{m_\mathrm{i} T_\mathrm{e}}} \left(1 + \frac{e|\Phi_\mathrm{d}|}{k_\mathrm{b} T_\mathrm{i}}\right) - \exp\left(-\frac{e|\Phi_\mathrm{d}|}{k_\mathrm{b} T_\mathrm{e}}\right). \tag{1.47}$$

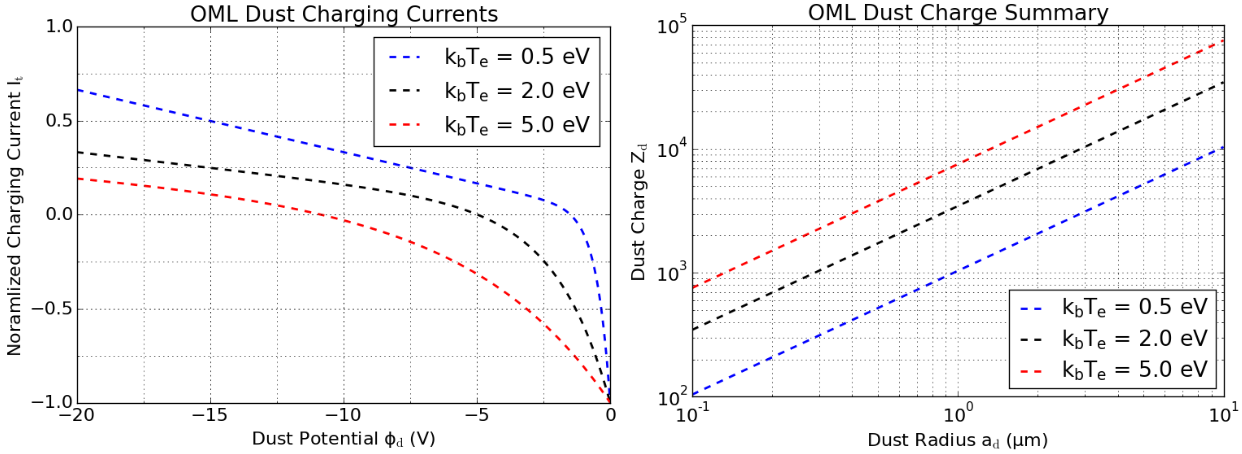

(a) (b)

Figure 1.4: Argon parameters: $k_\mathrm{b}T_\mathrm{i} = 0.025$ eV. a) The normalized total charging current I_t versus dust grain potential Φ_d according to Eq. (1.46). The normalized total charging current is obtained by dividing I_t by the constant in front of the square brackets in Eq. (1.46). b) Solutions to Eq. (1.47) to find the equilibrium dust potential versus dust grain radius a_d. The equilibrium dust potential was converted to the charge using $q_\mathrm{d} = -Z_\mathrm{d}e = 4\pi\epsilon_\mathrm{o}a_\mathrm{d}\Phi_\mathrm{d}$.

The charge of the dust grain, q_d, can be related to the electrostatic potential of the grain, Φ_d, through the following relationship:

$$q_\mathrm{d} = C\Phi_\mathrm{d} \tag{1.48}$$

where C is the capacitance of the grain. Following the work of [13], the capacitance is taken to be that of two concentric spheres separated by a distance L so that

$$C = 4\pi\epsilon_\mathrm{o}a_\mathrm{d}\left(1 + \frac{a_\mathrm{d}}{L}\right). \tag{1.49}$$

In the case presented here, the capacitance is evaluated between the dust grain surface and the outer sheath edge where $L = L_\mathrm{d}$ and L_d is the dust grain Debye length given by Eq. (1.8). In most cases $a_\mathrm{d} \ll L_\mathrm{d}$ and Eq. (1.49) becomes

$$C = 4\pi\epsilon_\mathrm{o}a_\mathrm{d}. \tag{1.50}$$

Eq. (1.50) is the so-called thick sheath limit and applies to dusty plasmas where the dust dimensions are much smaller than the Debye length.

The normalized charging current according to Eq. (1.46) and the corresponding dust grain charge obtained by solving Eq. (1.47) are summarized in Fig. (1.4) for several values of the electron temperature. As the electron temperature increases and the electrons are on average more energetic, the contribution to the charging current from the electrons becomes greater because a greater fraction of the electron population is able to overcome the repulsive potential of the grain — thus making the dust grain potential more negative. A useful and approximate empirical formula obtained from performing a linear fit to the equilibrium dust charge versus grain radius is

$$Z_{\mathrm{d}} \approx 3400 \cdot a_{\mathrm{d}}[\mu\mathrm{m}] \tag{1.51}$$

where a_{d} is the dust grain radius in units of μm. This formula is applicable only in the case where $k_{\mathrm{b}}T_{\mathrm{e}} = 2.0$ eV such that $T_{\mathrm{e}}/T_{\mathrm{i}} = 80$ and $m_{\mathrm{i}}/m_{\mathrm{e}} = 72810$ for Argon plasma. Eq. (1.51) is in agreement with the approximate analytic formula derived in [67].

OML charging timescales

When an initially uncharged dust grain is inserted into a plasma, the timescale required for the dust grain to reach its equilibrium charge may vary based on not only the size of the grain but also the plasma conditions. Eq. (1.46) can be converted to a first-order differential equation for the grain charge by making the substitution

$$I_{\mathrm{t}} = \frac{dq_{\mathrm{d}}}{dt} = -e\frac{dZ_{\mathrm{d}}}{dt} \tag{1.52}$$

so that

$$\frac{dZ_{\mathrm{d}}}{dt} = -4\pi a_{\mathrm{d}}^2 n_{\mathrm{o}}\sqrt{\frac{k_{\mathrm{b}}T_{\mathrm{e}}}{2\pi m_{\mathrm{e}}}}\left[\sqrt{\frac{m_{\mathrm{e}}T_{\mathrm{i}}}{m_{\mathrm{i}}T_{\mathrm{e}}}}\left(1+\frac{e^2 Z_{\mathrm{d}}}{4\pi\epsilon_{\mathrm{o}}a_{\mathrm{d}}k_{\mathrm{b}}T_{\mathrm{i}}}\right) - \exp\left(-\frac{e^2 Z_{\mathrm{d}}}{4\pi\epsilon_{\mathrm{o}}a_{\mathrm{d}}k_{\mathrm{b}}T_{\mathrm{e}}}\right)\right]. \tag{1.53}$$

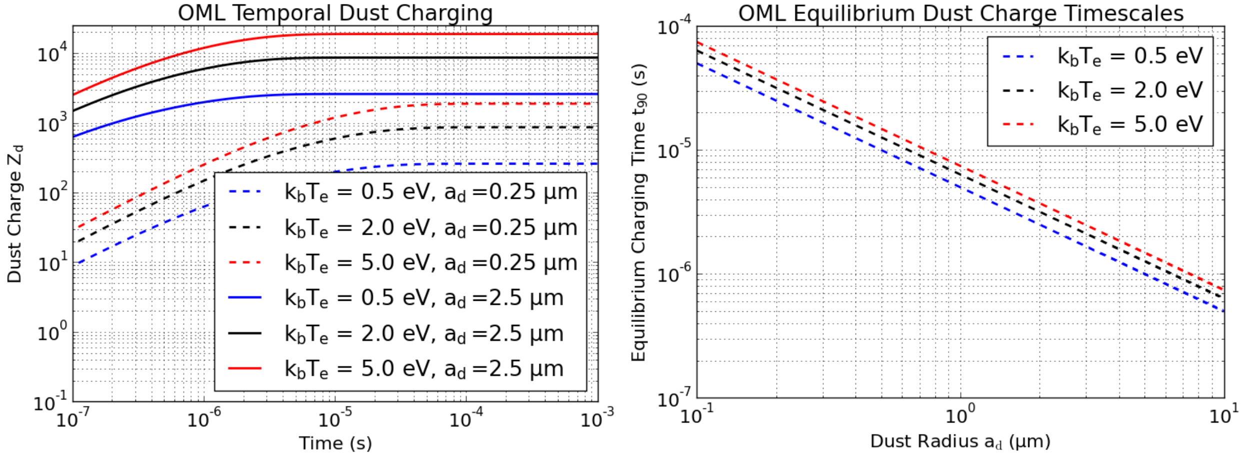

(a) (b)

Figure 1.5: Argon Parameters: $k_\mathrm{b}T_\mathrm{i} = 0.025$ eV, $n_\mathrm{e} = n_\mathrm{i} = 10^{15}$ m^{-3}. a) The grain charge Z_d plotted as a function of time by solving Eq. (1.53) for several values of the grain radius a_d and the electron temperature $k_\mathrm{b}T_\mathrm{e}$. b) The time taken for a dust grain to obtain 90% of its OML equilibrium charge t_{90} versus the grain radius a_d.

where Eqs. (1.48) and (1.50) were substituted for the grain potential Φ_d. Eq. (1.53) can be solved using standard numerical techniques [68]. The results are summarized in Fig. (1.5) where it is shown that large dust grains reach their equilibrium charge fastest. However, even for relatively small dust grains where $a_\mathrm{d} = 100$ nm, the equilibrium charge is obtained in less than 1 ms. These results are also in approximate agreement with [69, 70] where the discrete nature of charge collection was taken into account (as opposed to the continuous OML treatment given here). The charge fluctuations can also be well approximated by a Gaussian distribution [67] according to the expression

$$f(Z) = \frac{1}{\sigma_Z\sqrt{2\pi}} \exp\left(-\frac{(Z - Z_\mathrm{d})^2}{2\sigma_Z^2}\right) \tag{1.54}$$

where Z_d is the mean charge,

$$\sigma_Z^2 = \frac{1}{\beta_e}\left(\frac{1 - \frac{T_e}{T_i}\beta_e Z_\mathrm{d}}{1 + \frac{T_e}{T_i} - \beta_e Z_\mathrm{d}\frac{T_e}{T_i}}\right), \tag{1.55}$$

and $\beta_e = e^2/(4\pi\epsilon_o a_\mathrm{d} k_\mathrm{b} T_\mathrm{e})$. Eqs. (1.54 – 1.55) provide a good approximation for the charge distribution when $Z_\mathrm{d} > 50$. It is also interesting to note that the product $\beta_e Z_\mathrm{d}$ is independent of the particle size since Eq. (1.51) shows that Z_d is linear in a_d. Therefore, the width of the charge distribution given by Eq. (1.55) decreases as $(\sqrt{\beta_e})^{-1}$ or $\sqrt{a_\mathrm{d}}$ and therefore $\sigma_Z \approx \sqrt{Z_\mathrm{d}}$. For small dust grains (as in one to tens of nanometers) such as those typically found in plasma processing reactors, discrete charge fluctuations can sometimes lead to positively charged grains. Positively charged grains typically cannot be confined by plasma sheath electric fields and could therefore be important for the removal of grain impurities in processing reactors since. In other situations, it has also been shown that charge fluctuations can lead to enhanced agglomeration and dust grain growth rates in low pressure plasmas [71].

1.3.2 Limitations of the OML theory and its alternatives

Break down of the OML theory

Strictly speaking, the OML treatment of dust grain charging assumes that all ions within a mean free path of the dust grain with an impact parameter satisfying in inequality

$$b_\mathrm{i,max} \leq a_\mathrm{d}\sqrt{\left(1 + 2\frac{e|\Phi_\mathrm{d}|}{m_\mathrm{i} v_\mathrm{o,i}^2}\right)} \tag{1.56}$$

will be collected by the dust grain. The equality in Eq. (1.56) is a maximum impact parameter at which the incident ion will undergo a grazing collision infinitesimally close to the grain as shown by the red curve in Fig. (1.6). On the other hand, [72, 73] showed that all ions satisfying Eq. (1.56) may not actually hit the dust grain due to minima in the effective potential energy around the grain. Their work split the conservation of energy equation given by Eq. (1.37) into its velocity components to yield

$$\frac{1}{2}m_\mathrm{i} v_\mathrm{o,i}^2 = \frac{1}{2}m_\mathrm{i} v_\mathrm{r,i}^2 + \frac{1}{2}m_\mathrm{i} v_{\phi,\mathrm{i}}^2 + e\Phi_\mathrm{d} \tag{1.57}$$

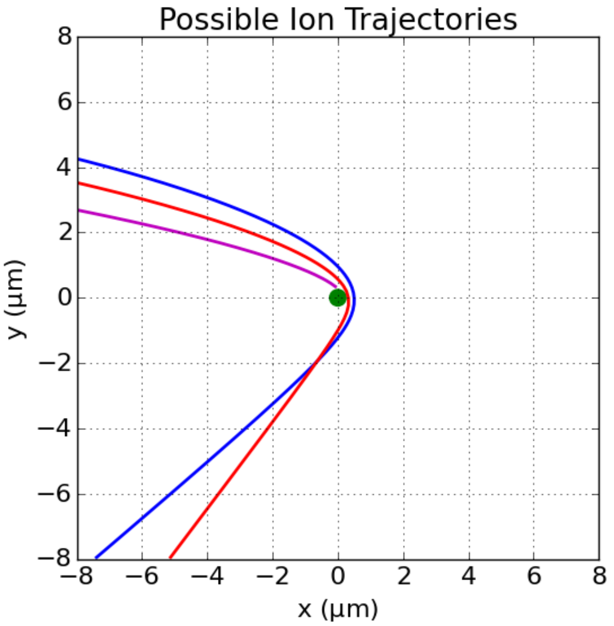

Figure 1.6: The green dot located at the origin represents an $a_\mathrm{d} = 0.25\ \mu$m dust grain with an equilibrium charge of $Z_\mathrm{d} = 840$. The three solid curves correspond to possible ion trajectories around a charged dust grain. The blue curve misses the grain, the red curve undergoes a grazing collision, and the magenta curve hits the grain.

where $v_{\mathrm{r,i}}$ and $v_{\phi,\mathrm{i}} = r\dot{\phi}$ are the radial and angular components of the ion velocity, respectively. An effective potential was then defined as

$$U_\mathrm{eff}(r) = e\Phi_\mathrm{d} + \frac{J^2}{2m_\mathrm{i}r^2} \tag{1.58}$$

where $J = m_\mathrm{i} r v_{\phi,\mathrm{i}}$ is the angular momentum of the ion and $e\Phi_\mathrm{d} < 0$ due to the attractive potential between the positive ion and the negatively charged dust grain. The term $J^2/(2m_\mathrm{i}r^2)$ is positive definite and can therefore be treated as a repulsive potential for the ions.

The effective potential energy given by Eq. (1.58) is plotted for several values of the angular momentum in Fig. (1.7). The large repulsive barriers where $U_\mathrm{eff} > 0$ close to the grain shown by the the blue J_4 curves correspond to ions with large angular momenta that do not come close to the dust grain. These are the ions that exceed the impact parameter condition given by Eq. (1.56) and are included in the OML theory. The large attractive wells where $U_\mathrm{eff} < 0$ shown by the black J_0 curves correspond to ions with negligible angular

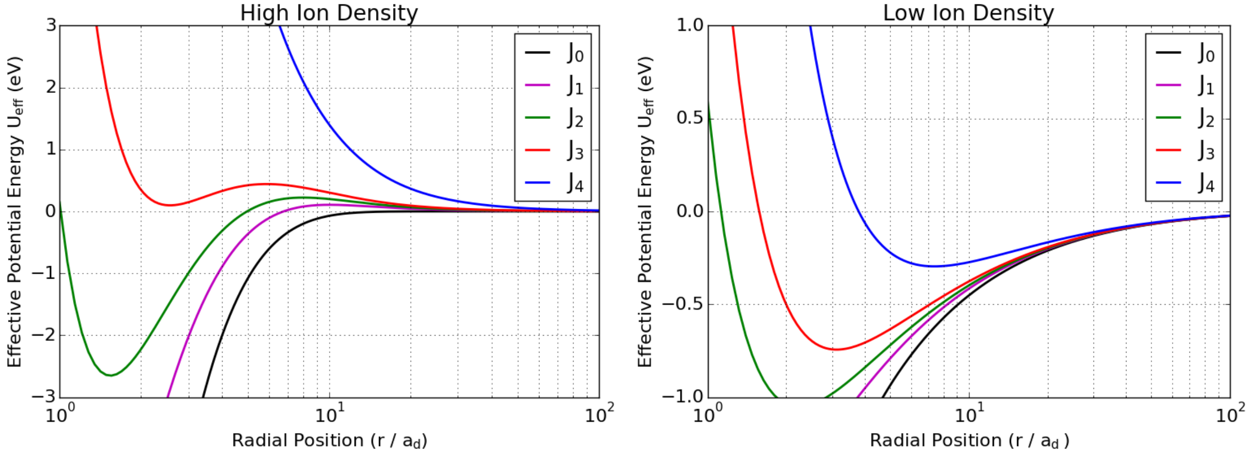

(a) (b)

Figure 1.7: Argon Parameters: $n_\mathrm{e} = 10^{15}$ m^{-3}, $k_\mathrm{b}T_\mathrm{e} = 2.0$ eV, $k_\mathrm{b}T_\mathrm{i} = 0.025$ eV. Several plots of the effective potential given by Eq. (1.58) in both the high and the low density limits that correspond to the small and large Debye length L_d limits, respectively. The Debye length is obtained from Eq. (1.9). The angular speed for the J_{0-4} cases is calculated with $v_{\phi,\mathrm{i}} = J_\mathrm{n}/(m_\mathrm{i} r)$ at the location of $r = 10a_\mathrm{d}$. a) $a_\mathrm{d} = 5.0$ μm, $Z_\mathrm{d} = 20000$, $n_\mathrm{i} = 4 \cdot 10^{17}$ m^{-3} and $L_\mathrm{d} = 1.7$ μm such that $v_{\phi,\mathrm{i}} = (0,\ 132,\ 163,\ 192,\ 380)$ m/s. b) $a_\mathrm{d} = 0.25$, μm, $Z_\mathrm{d} = 840$, $n_\mathrm{i} = 10^{15}$ m^{-3} and $L_\mathrm{d} = 37$ μm such that $v_{\phi,\mathrm{i}} = (0,\ 400,\ 510,\ 603,\ 930)$ m/s. The blue, red, and magenta curves in part b) correspond to the trajectories shown in Fig. (1.6).

momenta that approach the dust grain with a velocity that is mostly radial. This situation is also included in the OML theory and corresponds to a case where the ion impact parameter satisfies the inequality given by Eq. (1.56).

There are two intermediate cases with specific angular momentum values between J_0 and J_4 that correspond to the break down of the OML theory. First, in some situations, Eq. (1.58) has an inner minimum and outer maximum (i.e. where $dU_\mathrm{eff}/dr = 0$) such that ions streaming in toward the grain from infinity may not have enough energy to overcome the outer maximum. This is shown in the J_2 case (green curve) of Fig. (1.7a) where there is a small potential barrier located at approximately r = 7 a_d. Second, when there are collisions near the grain that lead to low energy ions, the ions may become trapped [74, 75] in the inner minimum shown in the J_2 green and J_3 red curves. These ions remain trapped (i.e., bound) in this region indefinitely until undergoing another collision. [76] showed that the barrier height of the effective potential is given by the inequality

$$U_{\max} < 10^{-2} \frac{T_{\mathrm{e}}}{T_{\mathrm{i}}} \frac{a_{\mathrm{d}}}{L_{\mathrm{d}}} k_{\mathrm{b}} T_{\mathrm{i}}. \tag{1.59}$$

For typical glow discharge plasmas $T_{\mathrm{e}}/T_{\mathrm{i}} \approx 100$ and $a_{\mathrm{d}}/L_{\mathrm{d}} \approx 0.007$ so that

$$U_{\max} < 0.007 k_{\mathrm{b}} T_{\mathrm{i}}, \tag{1.60}$$

and hence only a small fraction of $k_{\mathrm{b}} T_{\mathrm{i}}$ Maxwell-Boltzmann distributed ions have low enough energy that they can become trapped. The distribution and number of these ions is still an open question, but in most cases they are usually ignored [73].

Alternative charging theories

The OML charging theory presented above is just one of several possible approaches to deriving the dust grain charge that are based on the orbital motion of ions. Some alternatives are the Modified Orbit Motion Limited (MOML) [77, 78] theory and the Flowing Orbit Motion Limited [22, 79] theory. All of these approaches are simplifications of the generalized Orbit Motion (OM) theory [80, 81]. In the OM theory, the ions are no longer assumed to undergo a grazing collision such as what is shown in Fig. (1.3b). Instead, an absorption radius exists inside which all ions are drawn into and collected by the dust grain. The OM theory is sparsely used because it is by far the most complicated. Moreover, [76, 80] have shown that for spherical grains, the OM theory ion current is identical to the OML theory ion current in the limit $a_{\mathrm{d}}/L_{\mathrm{d}} \to 0$.

As an alternative to the orbital motion category of dust grain charging theories, there is the Radial Motion (RM) charging theory [82, 83, 84]. In the RM theory, the ions are assumed to be cold such that $T_{\mathrm{i}} = 0$ at distances beyond a mean free path. Starting from rest, the ions gain kinetic energy by falling radially inward due to the attractive negative potential of the grain. The Poisson equation is then numerically solved for Boltzmann electrons (just as in the OML case) and a radially inward ion flow of ions. Angular motion is neglected. A useful (and approximate) empirical formula adapted from [83] for the RM predicted equilibrium dust grain charge is

$$Z_{\mathrm{d}} \approx 600 \cdot a_{\mathrm{d}}[\mu\mathrm{m}] \tag{1.61}$$

where a_{d} is the dust grain radius in units of μm. This formula is applicable only in the case where $k_{\mathrm{b}}T_{\mathrm{e}} = 2.0$ eV and $m_{\mathrm{i}}/m_{\mathrm{e}} = 72810$ for Argon plasma. In comparison to Eq. (1.51), the RM predicted equilibrium dust grain charge is approximately 20% of that predicted by the OML theory. This result is disputed by [84] where they claim that the boundary conditions were not handled correctly in [83] and as a result, the dust grain charge was over-estimated and should be much lower than what the empirical formula Eq. (1.61) predicts. Regardless of this dispute, Eq. (1.61) is still useful to provide an approximate estimate of the dust grain charge according to the RM theory.

Dust charge measurements

Up until this point, two possible estimations of the dust grain charge have been provided based on the OML and the RM charging theories. These theories predict dust grain charges which differ by a factor of at least 5 – 6. In reality, the true grain charge may lie somewhere in between these two limits. Since this dissertation is an experimental work, it is important to verify which theory is most likely correct based on previous experimental measurements. The following list includes a brief summary of experimental work to extract the dust grain charge.

- [85] examined binary dust collisions in a parabolic confinement along the sheath edge. It was found that although the error bars were large due to the limited spatial and temporal resolution of the grain motion in this early work, the effective dust charge was in very good agreement with the OML predictions.

- [86] studied the thermal mode spectra of finite dust clusters consisting of 3 to 145 dust grains in a plasma sheath and found that the measured dust grain charge was in good agreement with the OML predictions. This experiment is part of a broader category of resonance experiments where the resonance can be driven with natural thermal fluctuations (as in the work above), laser excitation [87, 88, 89], and even an external modulation applied to a wire that is inserted into the dust region [90]. All of these results broadly agree with the OML theory to within a factor of two.

- [91] performed charge measurements on a dust crystal suspended in the plasma sheath by modifying the tilt angle of gravity with respect to the crystal plane. The observed changes in the characteristic shielding length agreed with the OML theory.

- [92] examined the role of an ion-wake mediated non-reciprocal interaction force between two dust grains suspended in a vertical chain in a strongly magnetized plasma sheath. The driven electrode was modulated with a sinusoidal signal to induce small amplitude oscillations of the grains. The results showed that the dust charge remains constant for a magnetic field strength of up to B = 2.5 T. Larger magnetic field strengths were not considered.

With the exception of the first method, these works were based on the assumption of a linear plasma sheath electric field. A linear plasma sheath electric field is well justified by simulations [93, 94] and measurements [95, 96]. Based on the measurements above, the OML theory is considered to predict an accurate dust grain charge for grains suspended in the plasma sheath region. Therefore, we proceed with a theoretical development of dust grain $\mathbf{g} \times \mathbf{B}$ drift under the assumption that OML theory provides a reasonable estimate of the dust grain charge.

Chapter 2

Theory and Simulations: Using **g** x **B** Drift to Measure Grain Charge

In the previous chapter, applications of dusty plasmas were briefly introduced followed by an introduction to typical forces acting on laboratory dusty plasmas. A final emphasis was placed on the widely used OML theory of dust grain charging, its limitations, and some validation measurements. In this chapter, the requirements for dust grain magnetization are discussed in great detail where we propose an alternative method to quantify dust grain magnetization. Simulations are then used to outline the reasons why magnetizing dust grains in a plasma sheath under real experimental conditions is extremely difficult. As an alternative to dust magnetization in the plasma sheath, we construct a model for dust grain $\mathbf{g} \times \mathbf{B}$ drift motion in the plasma bulk and then show that observations of this motion can be used to obtain a unique measurement of the grain charge.

2.1 On the meaning of dust grain magnetization.

In contrast to the collisions between electrons or ions with the background neutral gas that were discussed in Sec. (1.2.3), a micron-sized dust grain is relatively unaffected by a single collision with a neutral gas particle. This is due to the approximately 10 orders of magnitude mass difference between the two. Although the mass difference is large, the average inter-neutral spacing in laboratory dusty plasmas is usually smaller than the grain diameter — meaning that there are many neutral gas particles in immediate proximity to a dust grain. For example, at a typical neutral gas pressure of $p_{\mathrm{n}} = 0.67$ Pa where the neutral particle number density is $n_{\mathrm{n}} \approx 1.6 \cdot 10^{20}$ m^{-3}, the approximate inter-neutral particle distance is 0.2 μm. This means that even for a relatively small dust grain radius of $a_{\mathrm{d}} = 0.25$ μm where the volume occupied by the grain is $V_{\mathrm{d}} = 6.5 \cdot 10^{-20}$ m^3, the dust grain is occupying

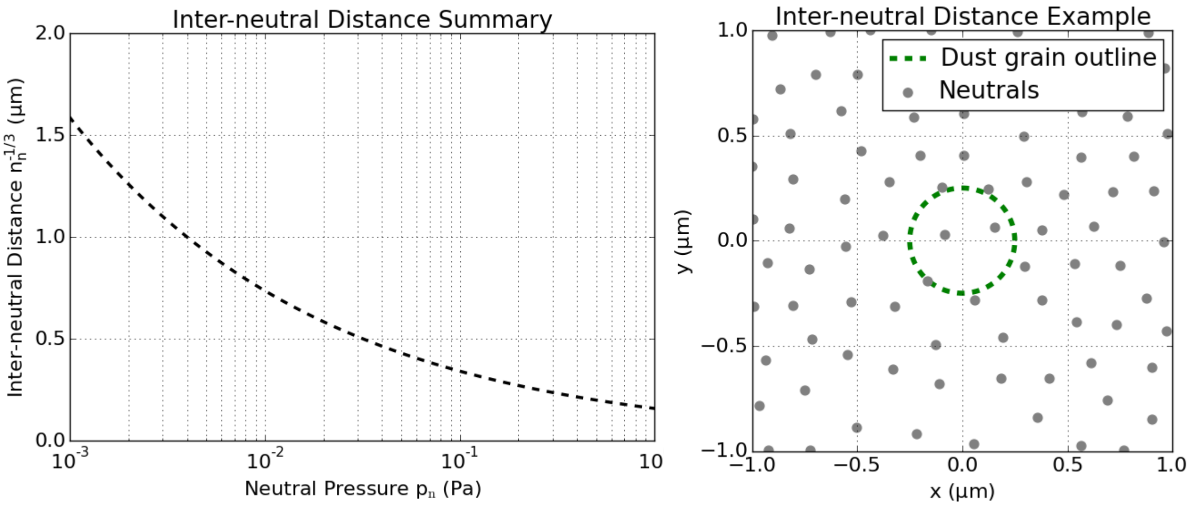

(a)

(b)

Figure 2.1: Argon parameters: $k_\mathrm{b}T_\mathrm{n} = 0.025$ eV. a) The approximate inter-neutral distance $n_\mathrm{n}^{-1/3}$ (where n_n is the number density) versus neutral pressure p_n b) An $a_\mathrm{d} = 0.25$ μm diameter dust grain surrounded by neutral gas particles at $p_\mathrm{n} = 0.67$ Pa. The gray dots represent a typical inter-neutral spacing of approximately 0.2 μm. The dust grain radius (green dashes) and the neutral particle spacing (gray dots spacing) are to scale. The area of the gray dots is not to scale.

the space where approximately 4 neutral particles would otherwise be. In fact, the average inter-neutral distance does not exceed approximately 1 μm until a neutral gas pressure of $p_\mathrm{n} \approx 0.0033$ Pa, which is far below the usual operating pressures of dusty plasma experiments. A summary of typical characteristic inter-neutral length scales versus neutral gas pressure is provided in Fig. (2.1).

When quantifying dust grain magnetization, it is important to take into account both the cumulative effect of many dust-neutral collisions and also the large mass difference between the neutral particles and the dust grains. We define a modified Hall parameter specifically for an isolated dust grain as the ratio of the stopping distance due to neutral collisions to the Larmor circumference of the dust grain. This is expressed as

$$H_\mathrm{m,d} = \frac{x_\mathrm{stop}}{2\pi r_\mathrm{L,d}} \tag{2.1}$$

where x_{stop} is the dust grain stopping distance and

$$r_{\mathrm{L,d}} = \frac{m_{\mathrm{d}} v}{q_{\mathrm{d}} B} \tag{2.2}$$

is the dust grain Larmor radius where v is the velocity of the dust grain and m_{d} is the dust grain mass. The stopping distance is the distance that a dust grain, when given an initial velocity, will travel before coming to rest due to the cumulative effect of many dust-neutral collisions. A dust grain is considered to be magnetized when $H_{\mathrm{m,d}}$ is of the order unity such that it will travel a total distance of at least one Larmor circumference before the cumulative effect of many dust-neutral collisions brings the dust grain to rest.

We derive the stopping distance by considering a 1D model of a dust grain under the influence of linear drag and no other forces. In this situation, the equation of motion is

$$\frac{dv}{dt} = -\Gamma v \tag{2.3}$$

where $\Gamma = \gamma / m_{\mathrm{d}}$ is the normalized Epstein drag coefficient. Epstein drag was briefly introduced in Sec. (1.2.5) and is further discussed and measured in great detail in Sec. (4.1.3). For the purposes of this derivation, the factor Γ has a value of the order $1 - 100$ s^{-1} and is given by Eq. (1.27). In this context, Γ can be thought of as the decay rate of the dust grain momentum due to frequent neutral collisions. The integration of Eq. (2.3) is straightforward and yields

$$v(t) = v_{\mathrm{o}} \exp\left(-\Gamma t\right) \tag{2.4}$$

where the initial time is assumed to be zero and v_{o} is the initial velocity. Eq. (2.4) can be integrated again to get the position of the dust grain

$$x(t) = \frac{v_{\mathrm{o}}}{\Gamma}\left(1 - \exp\left(-\Gamma t\right)\right) \tag{2.5}$$

where the initial position of the dust grain was assumed to be $x_\text{o} = 0$. In the limiting case of $t \to \infty$, the position of the dust grain asymptotically approaches its final resting position

$$x_\text{stop} = \frac{v_\text{o}}{\Gamma}. \tag{2.6}$$

Eq. (2.6) is the stopping distance. Eq. (2.2) and Eq. (2.6) can be substituted into Eq. (2.1) to get the following expression for the modified Hall parameter:

$$H_\text{m,d} = \frac{\omega_\text{d}}{2\pi\Gamma} = \frac{q_\text{d}B}{2\pi\Gamma m_\text{d}} \tag{2.7}$$

where ω_d is the dust Larmor frequency. Alternatively, returning to Eq. (2.1), the factor of 2π can be omitted by taking the ratio of the stopping distance to the Larmor radius (rather than the circumference) of the dust grain orbital path. In this case, we have

$$H_\text{d} = 2\pi H_\text{m,d} = \frac{\omega_\text{d}}{\Gamma} \tag{2.8}$$

where H_d is the dust Hall parameter. For the remainder of this dissertation, we will refer to Eq. (2.7) as the modified dust Hall parameter and Eq. (2.8) as the dust Hall parameter.

So far, by comparing the ratio of the dust grain stopping distance to the Larmor circumference (or radius), we derived two possible expressions to quantify the magnetization of an isolated dust grain which differ by a factor of 2π. At first glance, the factor of 2π may seem to be of no consequence; however, as we will soon show using simple 2D models, the factor of 2π is extraordinarily important when designing an experiment to observe dust magnetization. For example, consider the situation where a charged dust grain is confined to the 2D x-y plane and is subject to both the magnetic force (where $\mathbf{B} = B_\text{o}\hat{z}$) and neutral gas drag. The coupled equations of motion for this model are

$$\frac{d^2x}{dt^2} = \omega\frac{dy}{dt} - \Gamma\frac{dx}{dt} \tag{2.9}$$

and

$$\frac{d^2y}{dt^2} = -\omega\frac{dx}{dt} - \Gamma\frac{dy}{dt}. \tag{2.10}$$

Eqs. (2.9) and (2.10) can be non-dimensionalized with the substitutions $\tilde{x} = x/r_{\mathrm{L,d}}$, $\tilde{y} = y/r_{\mathrm{L,d}}$, and $\tilde{t} = t\omega_{\mathrm{d}}/(2\pi)$ to become

$$\frac{d^2\tilde{x}}{d\tilde{t}^2} = 2\pi\frac{d\tilde{y}}{dt} - \frac{1}{H_{\mathrm{m,d}}}\frac{d\tilde{x}}{dt} \tag{2.11}$$

and

$$\frac{d^2\tilde{y}}{d\tilde{t}^2} = -2\pi\frac{d\tilde{x}}{dt} - \frac{1}{H_{\mathrm{m,d}}}\frac{d\tilde{y}}{dt}. \tag{2.12}$$

This non-dimensional form is convenient for both deriving the analytic solution (see Appendix C for details) as well as plotting solutions to examine the motion of the dust grain for different values of both the modified and standard Hall parameters. Fig. (2.2) shows example

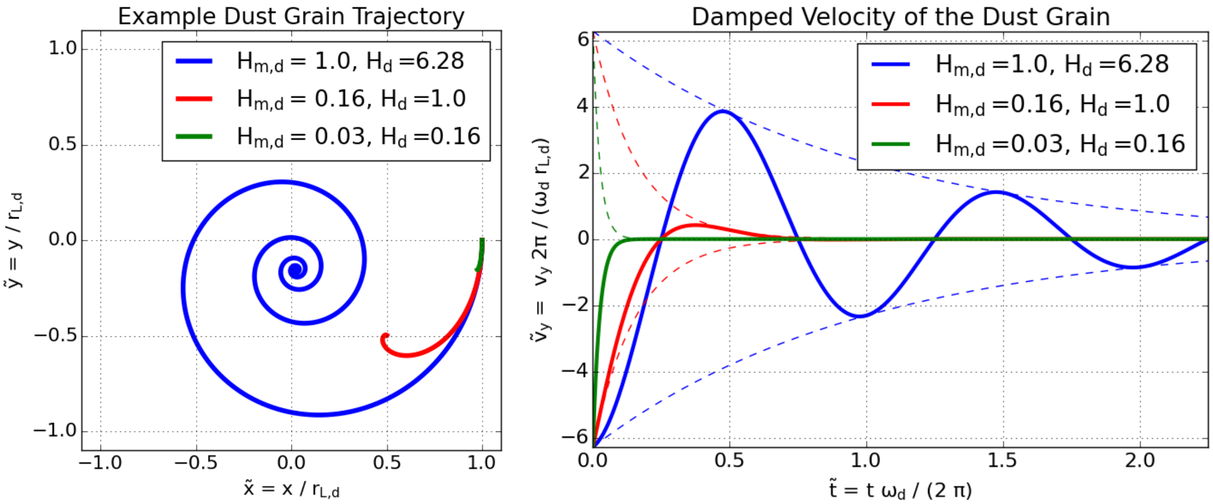

(a)

(b)

Figure 2.2: Solutions to Eqs. (2.11 – 2.12) are plotted with the axes in non-dimensional form. a) Dust grain trajectories for several values of the modified Hall parameter. The solid blue curve corresponds to a case when $H_{\mathrm{m,d}} = 1$ and $H_{\mathrm{d}} = 2\pi$. The solid red curve corresponds to a case where $H_{\mathrm{m}} = 1/(2\pi)$ and $H_{\mathrm{d}} = 1$. The solid green curve corresponds to a case where $H_{\mathrm{m}} = 1/(2\pi)^2$ and $H_{\mathrm{d}} = 1/(2\pi)$. b) The non-dimensionalized y-velocity of the dust grain with the same color scheme as part a). The colored dashed lines are the exponential decay envelopes $\exp(-t/H_{\mathrm{m,d}})$ for the damped Larmor motion.

dust grain trajectories for different values of both versions of the Hall parameters. When the modified Hall parameter is $H_{\mathrm{m,d}} = 1$, the spiral-like Larmor motion, although damped, is still obvious. On the other hand, when the modified Hall parameter is $H_{\mathrm{m,d}} = 1/(2\pi)$, the Larmor motion is so strongly damped that it may become difficult to observe. Therefore, when constructing a laboratory experiment to magnetize dust grains, the factor of 2π between the Hall parameter definitions is an extremely important factor that determines whether or not the direct observation of dust grain Larmor motion is feasible.

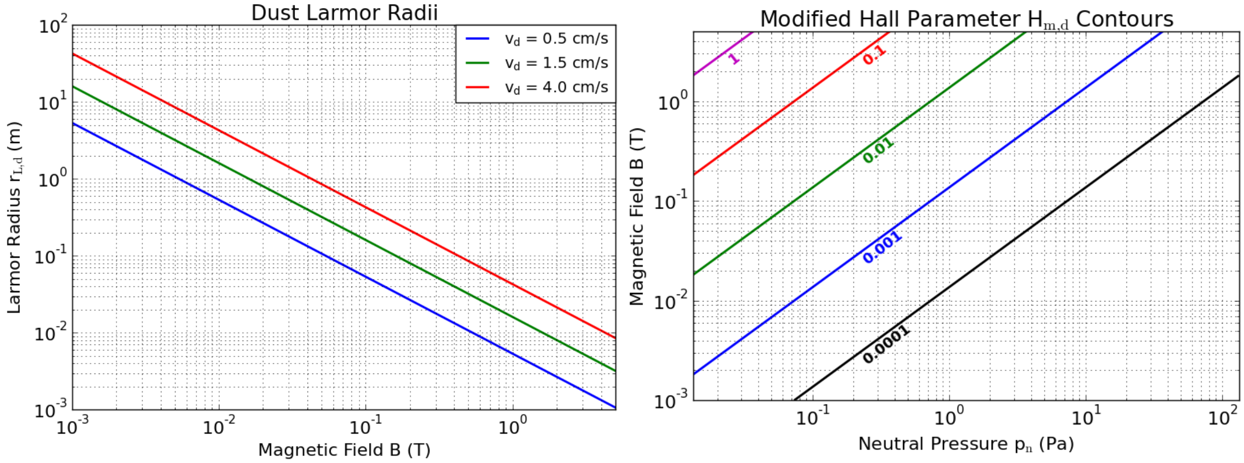

(a)

(b)

Figure 2.3: Parameters: $a_{\mathrm{d}} = 0.25\ \mu$m, $\rho_{\mathrm{d}} = 2.2$ g cm^{-3}. a) The dust grain Larmor radius versus magnetic field strength for several typical dust grain velocities in a laboratory. b) Contours of constant values of the modified dust grain Hall parameter $H_{\mathrm{m,d}}$ given by Eq. (2.7) versus neutral Argon pressure p_{n} and magnetic field strength B. For comparison, these dust grains at room temperature $k_{\mathrm{b}}T_{\mathrm{d}} = 0.025$ eV will have a thermal speed of $v_{\mathrm{th,d}} \approx 0.8$ cm/s.

As shown in this example model, the visibility of the dust grain Larmor motion strongly depends on the neutral gas damping factor Γ which was expressed in terms of experimentally controllable quantities in Eq. (1.27). Eq. (1.27) can then substituted into Eq. (2.7) to obtain the modified Hall parameter in terms of experimental quantities. Fig. (2.3b) shows contours of the modified Hall parameter for a dust grain with a radius $a_{\mathrm{d}} = 0.25\ \mu$m and a charge $Z_{\mathrm{d}} = 840$. The only region of (B, p_{n}) parameter space where the modified Hall parameter is greater than 1 is the upper left hand corner where B ≥ 1.0 T and $p_{\mathrm{n}} \leq 0.04$ Pa. Therefore, duplicating the dust grain motion of Fig. (2.2) in a laboratory will require a large magnetic field as well as operating at a neutral gas pressure below the usual dusty plasma experiment range of $p_{\mathrm{n}} \geq 0.13$ Pa. A summary of the dust grain Larmor radius is also included in Fig. (2.3a) because an experiment in this geometry also requires that the Larmor diameter be smaller than the physical dimensions of the plasma chamber which is usually of the order 7 – 20 cm.

The dust grain magnetization requirements discussed in this section highlight the extraordinary difficulty of constructing and operating an experiment that magnetizes the dust grains and clearly shows Larmor motion. However, it may be possible to observe dust grain magnetization effects other than pure Larmor motion. The remainder of this dissertation is devoted to constructing and performing an experiment to measure the $\mathbf{g} \times \mathbf{B}$ magnetization effect on dust grains. In the next section, we will develop a theory to address the following open question: Can an experiment be designed such that the dust grains undergo a measurable amount of $\mathbf{g} \times \mathbf{B}$ drift, and if measurable, what other information about the dust grains can we extract from the measurement?

2.2 Modeling falling dust grains in the bulk of a magnetized plasma

In this section, we develop a theory for dust grain $\mathbf{g} \times \mathbf{B}$ drift (sometimes also called deflection) in a plasma bulk, and then show that the amount of deflection is measurable using realistic experimental conditions. It is also shown that the amount of deflection is directly proportional to the dust grain charge. As such, observations of this motion can therefore be used perform a unique dust grain charge measurement.

First, to illustrate the concept of $\mathbf{g} \times \mathbf{B}$ drift, we simplify the problem by neglecting the neutral drag on the dust grain. A dust grain that is subject to the magnetic force and the gravitational force obeys the equation of motion

$$\mathbf{F}_{\mathrm{net}} = m_{\mathrm{d}} \frac{d\mathbf{v}}{dt} = q_{\mathrm{d}} \mathbf{v} \times \mathbf{B} + m_{\mathrm{d}} \mathbf{g}. \tag{2.13}$$

Due to the cross product, the solution to Eq. (2.13) can be complicated depending on the geometry of the magnetic field. However, regardless of the magnetic field geometry, the solution can be split into three components such that

$$\mathbf{v} = \mathbf{v}_{\parallel} + \mathbf{v}_L + \mathbf{v}_g \tag{2.14}$$

where $\mathbf{v}_{\parallel}$ is the solution for parallel motion along the magnetic field, $\mathbf{v}_L$ is the solution for the usual oscillatory Larmor motion, and $\mathbf{v}_g$ is a velocity perpendicular to both $\mathbf{g}$ and $\mathbf{B}$ that satisfies the equation

$$q_{\mathrm{d}}\mathbf{v}_g \times \mathbf{B} + m_{\mathrm{d}}\mathbf{g} = 0. \tag{2.15}$$

The solution to Eq. (2.15) is

$$\mathbf{v_g} = \frac{m_{\mathrm{d}}}{q_{\mathrm{d}}}\frac{\mathbf{g} \times \mathbf{B}}{B^2}. \tag{2.16}$$

Eq. (2.16) is a guiding center drift of the dust grain that arises due to the coupling between the gravitational and magnetic fields and is called the $\mathbf{g} \times \mathbf{B}$ drift. In the following section, a more realistic framework for describing the motion of a dust grain falling through the plasma bulk is developed by introducing neutral drag to the model. When the neutral drag is introduced, the guiding center motion is suppressed, and the motion asymptotes to a constant deflection angle while approaching terminal speed.

2.2.1 The equations of motion

The motion of a dust grain falling vertically downward in the plasma bulk with neutral gas drag is governed by the following equations of motion:

$$\mathbf{F}_{\mathrm{net}} = m_{\mathrm{d}}\frac{d\mathbf{v}}{dt} = q_{\mathrm{d}}\mathbf{v} \times \mathbf{B} + m_{\mathrm{d}}\mathbf{g} - \gamma\mathbf{v}. \tag{2.17}$$

By expanding the cross product of Eq. (2.17) and substituting $\mathbf{B} = -B\hat{\mathbf{z}}$, the coupled 2D

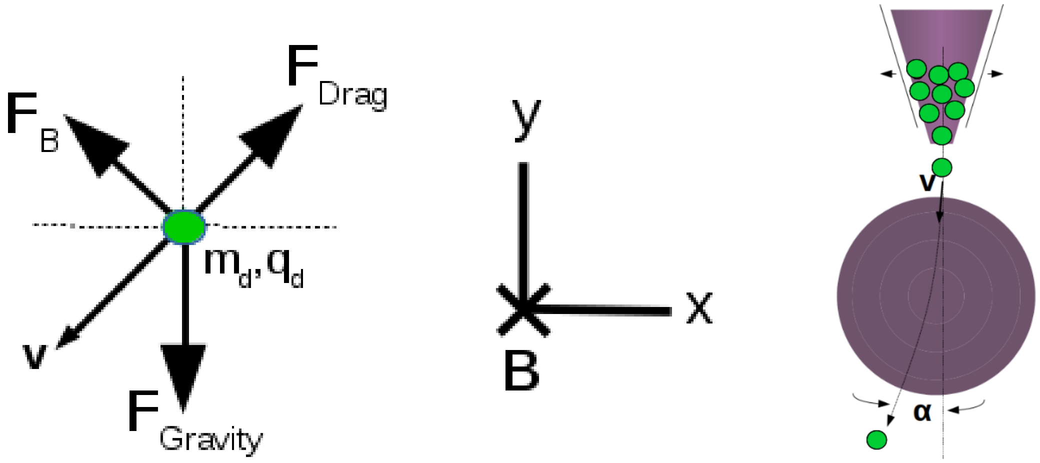

(a) (b)

Figure 2.4: a) A force diagram for the falling dust grain model. The particle is assumed to be moving down and to the left as illustrated by the arrow pointing toward **v**. The force inventory is as follows: $\mathbf{F}_{\mathrm{B}}$ is the magnetic force, $\mathbf{F}_{\mathrm{Gravity}}$ is the gravitational force, and $\mathbf{F}_{\mathrm{Drag}}$ is the neutral gas drag. b) An example cartoon of what the dust motion may look like. The asymptotic deflection angle is α.

system of equations becomes

$$\frac{d^2x}{dt^2} = -\omega_{\mathrm{d}}\frac{dy}{dt} - \Gamma\frac{dx}{dt} \tag{2.18}$$

and

$$\frac{d^2y}{dt} = \omega_{\mathrm{d}}\frac{dx}{dt} - \Gamma\frac{dy}{dt} - g. \tag{2.19}$$

2.2.2 Analytic solution to the equations of motion

The analytic solution to Eqs. (2.18 – 2.19) is a lengthy mathematical exercise that does not significantly contribute to the physics of the posed problem. Therefore, a detailed derivation of the solution is provided in Appendix C, and in this section, only a general outline of the major components of the solution is provided. The general solution is the sum of a homogeneous and a particular solution such that

$$\mathbf{v} = \mathbf{v}_h + \mathbf{v}_p. \tag{2.20}$$

The homogeneous solution is

$$\begin{aligned}\mathbf{v}_h(t) = &\left(v_{\mathrm{o,y}} + \frac{\Gamma g}{\omega_{\mathrm{d}}^2(1+\Gamma^2/\omega_{\mathrm{d}}^2)}\right)\exp(-\Gamma t)\begin{pmatrix}\sin(\omega_{\mathrm{d}}t)\\ \cos(\omega_{\mathrm{d}}t)\end{pmatrix}\\ &+\left(v_{\mathrm{o,x}} + \frac{g}{\omega_{\mathrm{d}}(1+\Gamma^2/\omega_{\mathrm{d}}^2)}\right)\exp(-\Gamma t)\begin{pmatrix}\cos(\omega_{\mathrm{d}}t)\\ -\sin(\omega_{\mathrm{d}}t)\end{pmatrix}\end{aligned} \tag{2.21}$$

where $v_{\mathrm{o,y}}$ and $v_{\mathrm{o,x}}$ are the initial velocities. The particular solution is

$$\mathbf{v}_{\mathrm{p}} = \frac{-g}{\omega_{\mathrm{d}}^2(1+\Gamma^2/\omega_{\mathrm{d}}^2)}\begin{pmatrix}\omega_{\mathrm{d}}\\ \Gamma\end{pmatrix}, \tag{2.22}$$

which is the $\mathbf{g}\times\mathbf{B}$ drift solution that has been modified due to the presence of neutral drag.

Eqs. (2.20 – 2.22) can be more easily understood by examining some limiting cases. The simplest limiting case is the situation where $g = 0$ and $\Gamma = 0$ (i.e., when there is no gravity or neutral gas drag). In this case, the particular solution vanishes and the homogeneous solution contains the expected undamped oscillatory Larmor motion. A second important limiting case is when $g = 0$ and $\Gamma \neq 0$. In this case, the Larmor motion is exponentially damped such that the dust grain will undergo spiral-like motion, which is the same behavior that was discussed in Sec. (2.1).

2.3 Adapting terminal speed solutions to real experimental conditions

The terminal speed limiting case where $t \to \infty$ can be used to understand the dust grain motion under realistic experimental conditions. In this limit, the homogeneous solution given by Eq. (2.21) vanishes and only the particular solution given by Eq. (2.22) remains. We define the ratio of the x and y components of the particular solution velocities as

$$\alpha = \frac{|v_{\mathrm{x}}|}{|v_{\mathrm{y}}|} = \frac{\omega_d}{\Gamma} \tag{2.23}$$

which is the same asymptotic terminal speed deflection angle α as shown in Fig. (2.4b). This terminal speed deflection angle α is mathematically equivalent to the dust Hall parameter Eq. (2.8), and it has already been shown in Sec. (2.1) that the neutral gas drag will make observations of dust grain magnetization difficult. The components of the terminal velocities are

$$v_{\mathrm{x}} = -\frac{\omega_{\mathrm{d}} g}{\Gamma^2} \frac{1}{1 + \left(\frac{\omega_{\mathrm{d}}}{\Gamma}\right)^2} \tag{2.24}$$

and

$$v_{\mathrm{y}} = -\frac{g}{\Gamma} \frac{1}{1 + \left(\frac{\omega_{\mathrm{d}}}{\Gamma}\right)^2}. \tag{2.25}$$

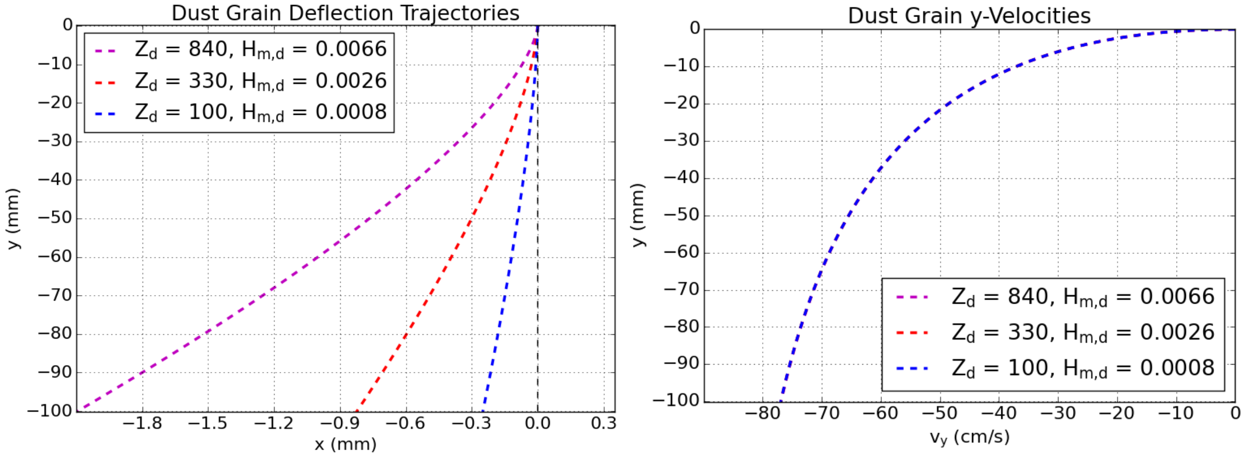

(a) (b)

Figure 2.5: Parameters: $B_{\mathrm{z}} = -0.5$ T, $a_{\mathrm{d}} = 0.25$ μm, $p_{\mathrm{n}} = 0.67$ Pa. a) Solutions to Eqs. (2.18 – 2.19) in an Argon plasma for several different values of the dust charge Z_{d}. b) Vertical position of the dust grain versus the y-velocity v_{y}. The dust grain charge does not significantly affect the terminal speed because $H_{\mathrm{d}} = \omega_{\mathrm{d}}/\Gamma \ll 1$ and hence $v_{\mathrm{y}} = -g/\Gamma$ according to Eq. (2.25).

In contrast to the model presented in Sec. (2.1), the neutral drag is not able to bring the falling dust grain to rest due to the presence of the gravitational force. Instead, the dust grain will reach terminal speed and its deflection will asymptotically approach the constant angle α. The size of the deflection angle determines whether or not it is possible to observe this effect under laboratory conditions. The deflection angle can be written in terms of experimental quantities as

$$\alpha = \frac{q_{\mathrm{d}}B}{\frac{4}{3}\pi\sqrt{\frac{8m_{\mathrm{n}}}{\pi k_{\mathrm{b}}T_{\mathrm{n}}}}\delta p_{\mathrm{n}}a_{\mathrm{d}}^2} \sim \frac{q_{\mathrm{d}}B}{p_{\mathrm{n}}a_{\mathrm{d}}^2}. \tag{2.26}$$

so that it contains all of the necessary information to define the experimental parameters under which the dust grain $\mathbf{g}\times\mathbf{B}$ deflection is measurable. Eq. (2.26) shows that the magnetic field B must be maximized whereas the dust grain radius a_{d} and the neutral gas pressure p_{n} must be minimized. The dust grain charge Z_{d} is not an experimentally controllable quantity (i.e., the experimenter cannot "set" a specific grain charge), so it is important to examine dust grain trajectories for several values of the dust grain charge as shown in Fig. (2.5). In the worst case scenario where $Z_{\mathrm{d}} = 100$ and $H_{\mathrm{m,d}} = 0.0008$, the falling dust grains still deflect a horizontal distance of approximately 0.3 mm over a vertical distance of 10 cm.

For the dust grain $\mathbf{g} \times \mathbf{B}$ drift experiments performed in this dissertation, the camera resolution is typically 20 μm per pixel with a viewing region of approximately 4 x 4 cm^2. This means that if the particle deflection is observed over the latter half of the trajectory shown in Fig. (2.5), the grain will deflect nearly 140 μm = 7 pixels which is a reasonable amount to measure. It is also important to note that in this analysis, even though the modified Hall parameter is extremely small (of the order 10^{-3}), the dust grain $\mathbf{g}\times\mathbf{B}$ magnetic effect is still likely to be observable. Thus, we have shown that the geometry the model presented in this section permits the detection of magnetic effects at low modified Hall parameters, which in many other experiment geometries would not be possible. Furthermore, since the deflection angle α given by Eq. (2.26) is directly proportional to the grain charge, an observation of α will provide a measurement of the dust grain charge q_{d}.

Chapter 3

Analysis Software and Experiment Apparatus

In Chapter 2, a theory of $\mathbf{g} \times \mathbf{B}$ drifting dust grains in the plasma bulk was presented. The dust grains quickly reach terminal speed while also approaching an asymptotic deflection angle given by Eq. (2.26) that is linearly proportional to the dust grain charge. Due to this linear relationship, an observation of the asymptotic deflection angle can be used to directly measure the dust grain charge. The terminal speed deflection angle also turns out to be mathematically equivalent to the dust Hall parameter given by Eq. (2.8) which means that a measurement of the deflection angle is also a measurement of the magnetization of the dust grains. In this chapter, we outline the creation of an image analysis module for the Complex Plasma Analysis (CoPlA) software package that was used to observe the dust grain $\mathbf{g} \times \mathbf{B}$ deflection, and then discuss details of the Magnetized Dusty Plasma eXperiment (MDPX) device that will be used to generate the necessary high magnetic field environment.

3.1 The Complex Plasma Analysis (CoPlA) software

CoPlA is a dusty plasma experiment control manager written in the C++ programming language that was originally written by U. Konopka. The low level nature of C++ code allows users to closely manage system resources to optimize performance. Recent work on the CoPlA software by B. Lynch was focused on the addition of a fast image analysis module to the CoPlA software. The module performs a fast analysis on large volumes of digital imaging data so that information about dust cloud dynamics can be extracted in near real-time. In the following sections, the fundamentals of dusty plasma imaging and the relevant portions of the image analysis module that was used to perform the measurements in this dissertation are discussed.

3.1.1 An overview of dusty plasma imaging systems

The imaging systems and analysis methods used in dusty plasmas are very similar to those used in other engineering applications [97, 98, 99, 100, 101] where micron-sized tracer particles are inserted into hydrodynamic flows to study the properties of the underlying fluid medium. In the case of dusty plasmas, the tracer particles are the dust grains. The dust grain motion is influenced by not only the underlying plasma (fluid) medium, but also the inter-dust electrostatic forces.

The macroscopic size of the dust grains permits the use of relatively inexpensive (∼ $2000 US) digital imaging systems to observe dust grain motion. The dust grains are illuminated using a monochromatic laser that is spread into a laser sheet using a cylindrical lens. Digital cameras are then used to record the dust grain motion. In single camera viewing systems such as those illustrated in Figs. (3.1 – 3.2), light scattered from dust grains is typically observed at 90 degrees from the paraxial axis in order to maximize the depth of field. An important feature of these digital imaging systems is that they do not perturb the underlying dust system yet still contain valuable information pertaining to both the inter-dust interactions as well as properties of the non-dusty plasma components. A typical illuminating laser has a power of approximately 50 – 300 mW, which, when spread into an illuminating plane, does not contain sufficient energy density to influence dust grain motion. Camera frame rates may range from 30 – 1000 frames per second (FPS) with 0.2 – 8 Megapixel (MP) resolutions. The spatial resolution of these systems typically ranges from 20 – 40 μm/pixel.

The two most common image analysis methods applied to dusty plasmas are the Particle Image Velocimetry (PIV) and the Particle Tracking Velocimetry (PTV) techniques. The PIV technique analyzes the shift in spatial correlation peaks between sub-domains of an image. The shift in the correlation peak is then used to calculate a velocity. Since each sub-domain typically contains many dust grains, the PIV technique is a non-localized technique that extracts only an average velocity of the grains within the sub-domain. The PIV technique is

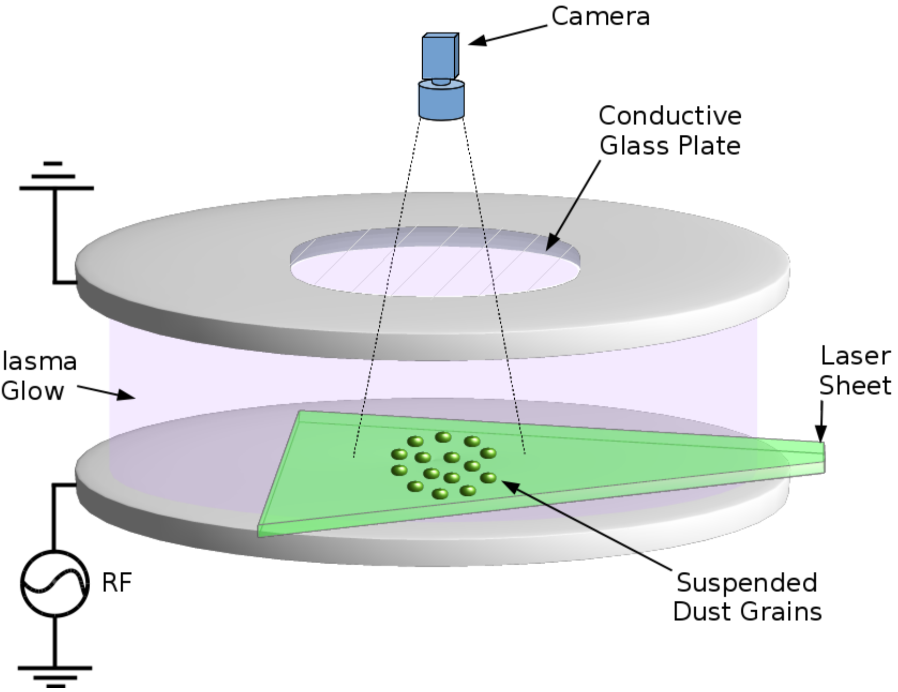

Figure 3.1: A top-down view camera looks through a transparent glass plate coated with a conductive film that is mounted within the grounded top electrode. The dust grains are vertically suspended in the plasma sheath electric field and illuminated with a thin horizontal laser sheet. An RF signal is applied to the bottom electrode. This is a common experiment geometry for single camera viewing systems. Some configurations may also have an RF signal applied to both the top and bottom electrodes.

best suited for systems with a large particle number densities that may not be individually resolvable. As an alternative to PIV, the PTV technique is a localized method that tracks individual particles through sequential image frames by performing particle-pairing so that a velocity is calculated for each individual dust grain. However, in cases where there are many particles in close vicinity to each other, particle-pairing may become ambiguous and the calculated velocities may be incorrect. As a result, the PTV technique is best suited for systems with low particle number densities. Both of these techniques are discussed in great detail in textbooks [102, 103, 104], review articles [105, 46, 106, 107], as well as discussions of a crossover between the two techniques [108, 109, 110].

A challenge for all imaging systems and analysis techniques is the management of large volumes of data. For example, a single 8-bit 4 MP grayscale camera operating at 100 frames

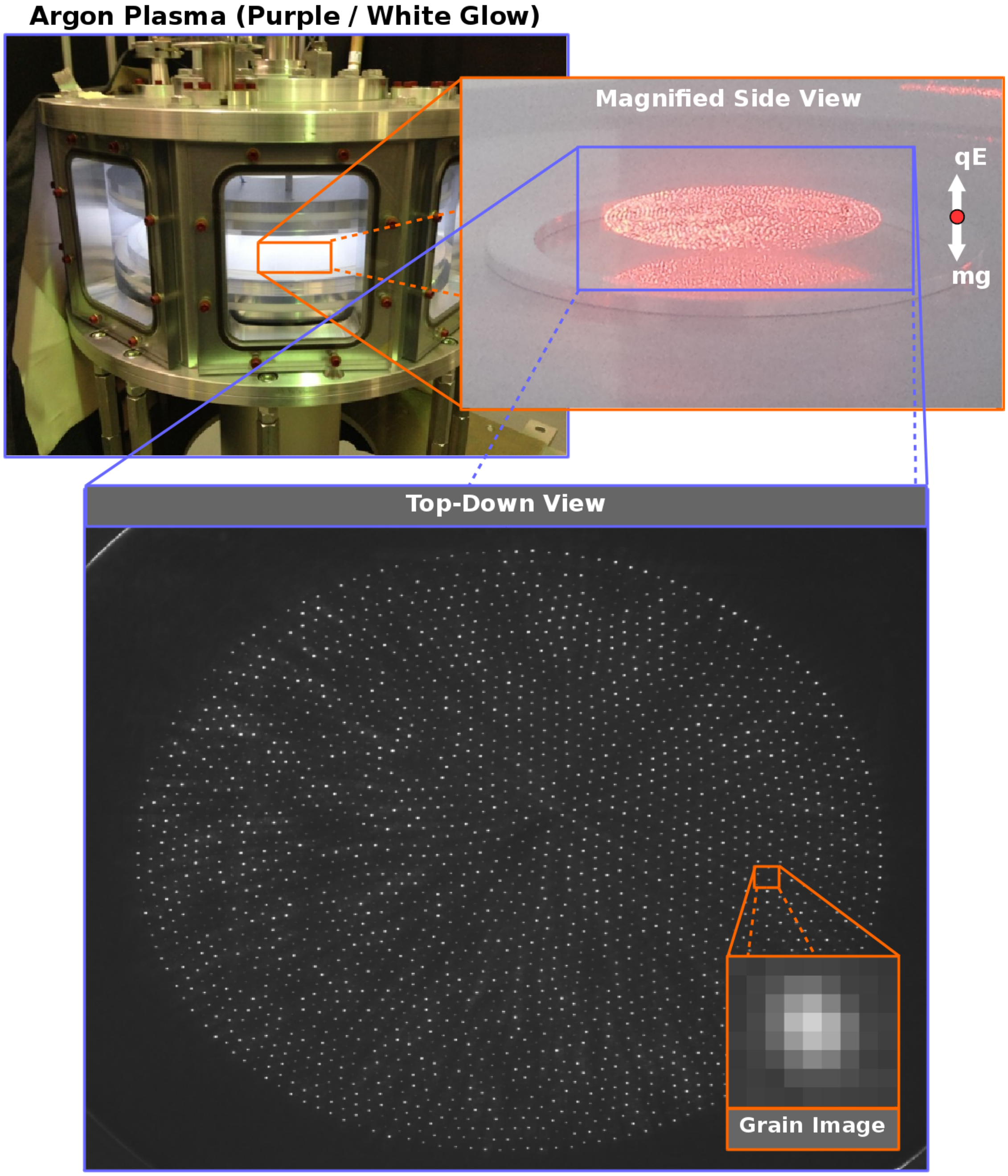

Figure 3.2: The vacuum chamber contains a plasma (the white/purple glow) that is generated by an RF signal applied to the bottom electrode while the top electrode is grounded. This is the same electrical configuration shown in Fig. (3.1). In the magnified side view, the dust cloud is illuminated using a red laser spread into an sheet using a cylindrical lens. The dust cloud (red dots) is vertically suspended against gravity by the plasma sheath electric field. The top-down view is an 8-bit grayscale image of the dust cloud containing several thousand dust grains (white dots). The spatial resolution is approximately 30 μm/pixel.

per second will generate 4 Gigabytes (GB) of data every 10 seconds. In most cases, the data is stored on a hard disk for post-experiment analysis, and even then, analyzing all recorded data is a substantial computational challenge. For this reason, having a highly optimized and computationally efficient method to analyze large volumes of dusty plasma imaging data could be highly advantageous. For example, several Terabytes (TB) of data was recorded for this dissertation and without access to fast analysis software, categorizing and sorting the data would have been computationally prohibitive. In addition, for some systems, the fast analysis could be used to construct an autonomous experiment that is operated in a closed feedback control loop.

The fast image analysis and PTV module that was added to CoPlA was aimed at circumventing the logistical and technical issues associated with large volume data management. The software has been thoroughly benchmarked and tested in [111]. In the following section, we briefly summarize the components of the image analysis module that are relevant to the analysis performed in this dissertation.

3.1.2 Dust grain identification technique

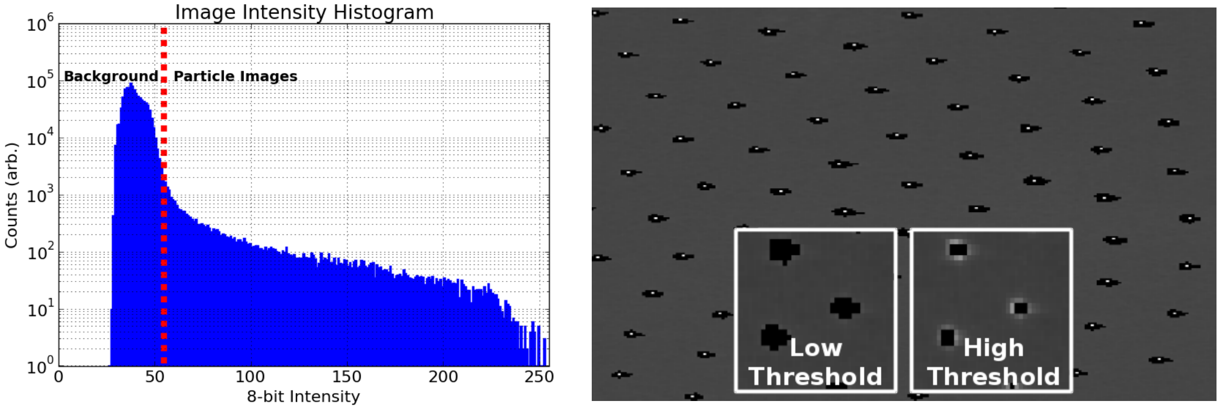

(a) (b)

Figure 3.3: a) A pixel intensity histogram of the entire top-down view image from Fig. (3.2). b) An example image demonstrating the effect of high and low global intensity thresholds. The white dots in the background image are the calculated centers of intensity for each grain.

The CoPlA particle identification routine uses a global intensity threshold to identify all pixels that belong to dust grains. The effect of the global intensity threshold is shown in Fig. (3.3). There are several alternative methods for selecting the appropriate intensity threshold such as those discussed in [112, 113]. However, these methods have a substantial computational overhead. In our fast analysis approach, we select an appropriate threshold in an ad-hoc manner that minimizes computational overhead while still allowing us to reliably identify dust grains. If the thresholded image (as shown in Fig. (3.3b)) does not appear to be collecting all pixel information, a CoPlA user can change the threshold and receive instant feedback in real-time. Situations like this may arise in, for example, cases where the RF power applied to the plasma was recently increased. In this situation, the amount of background noise will increase and as a result, the threshold will need to be increased.

When a global intensity threshold is applied to an 8-bit grayscale image (where pixel intensity values vary from $0 - 255$), the CoPlA software is effectively creating a binary image. The resulting image is binary in a sense that all pixels with an intensity value above the threshold are treated as belonging to dust grains (i.e., “True”) and all pixel intensities at or below the threshold are assumed to be background noise (i.e., “False”). Some possible sources of background noise in dusty plasma experiments are thermal fluctuations of the camera sensor, plasma glow, and laser reflections. If the threshold is set too low, background noise may be collected from pixels in the local neighborhood of the grain. If the threshold is set too high, not all available information about the grain is collected. This is illustrated in Fig. (3.3b). Intensity thresholding, whether global or not, introduces some potential error into the calculated locations of dust grains. One such effect is pixel-locking where the calculated center of dust grains may bias toward integer values or integer sub-fractions of a pixel. This effect (and others), as well as mitigation techniques, are discussed in [114, 103].

After setting a global intensity threshold, the image analysis and PTV module of CoPlA iterates through each pixel of the image until a pixel is found with an intensity value greater than the threshold. When a pixel with the intensity value greater than the threshold is encountered, a grain's "edge" has been found at the location (i, j). A flood fill [115] is then performed starting from this edge (also called a seed pixel) to find all other pixels belonging to the grain image. Appendix D provides a detailed illustration of the flood fill algorithm. Once all pixel information has been collected, the center of each particle is found using a moment method, which is known to have a sub-pixel accuracy to within approximately 0.1 – 0.2 pixels or better for particle image diameters of 2 – 3 pixels [114].

3.2 The Magnetized Dusty Plasma Experiment (MDPX)

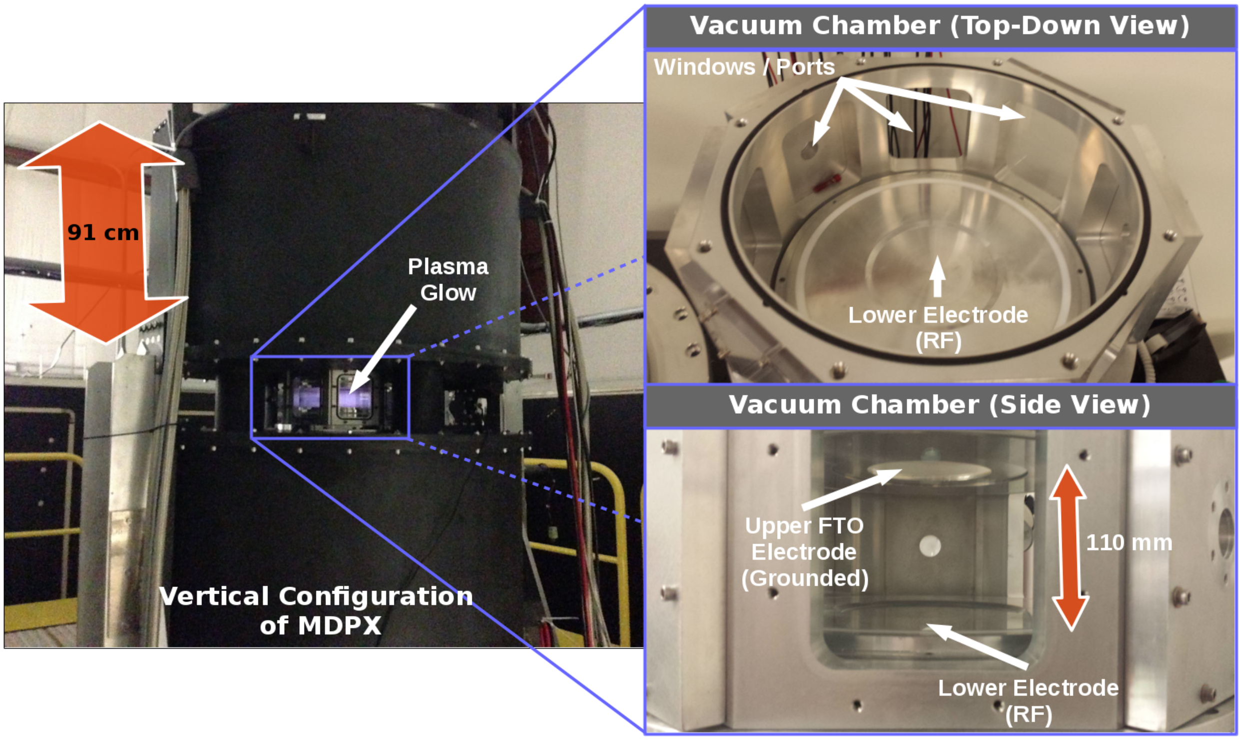

Figure 3.4: The Magnetized Dusty Plasma eXperiment (MDPX) in a configuration where the magnetic field is vertical. Each half of the magnet system (i.e. the hollow black cylinders) is 91 cm tall. The cylindrical halves are called the upper and lower cryostat, respectively. The spacing between the cryostats is 19 cm. Within the bore and at the axial mid-plane, an octagonal plasma chamber with an ID of 35.5 cm is mounted. The plasma chamber contains two 35.5 cm electrodes in a parallel-plate configuration with a 110 mm spacing. The purple plasma glow is shown in the left figure.

The Magnetized Dusty Plasma eXperiment (MDPX) device is an open-bore (i.e., a hollow cylinder with an OD of 125 cm and ID of 50 cm) and split-bore (meaning there are two separate 91 cm x 125 cm hollow cylindrical halves) superconducting magnet system. MDPX is shown in the vertical orientation in Fig. (3.4). Each hollow black cylinder contains two individually wound coils of niobium titanium superconducting wire. Each coil is independently controlled and programmable, which provides the ability to generate uniform magnetic fields up to 4 T or to generate spatially varying magnetic geometries such as a cusp or a linear gradient of up to 2 T/m [116]. The MDPX device is discussed in great detail in the literature [117, 118, 116, 119]. In this section, we provide only a brief summary of the relevant dimensions and performance information.

For the purposes of using the MDPX device to construct an experiment to observe dust grain $\mathbf{g} \times \mathbf{B}$ drift, we are interested in the uniform magnetic field mode of operation. Detailed measurements of the magnetic field in the plasma chamber region of the device [118] have shown that the axial magnetic field variations are of the order 0.2% over a 6 cm scanning distance, and the radial magnetic field variations are of the order 0.95% over a 20 cm distance. Due to the measured uniformity of the magnetic field generated by the MDPX device, for all measurements and error analysis performed in this dissertation, the magnetic field is considered to be uniform with no spatial variation.

The split-bore feature of the MDPX device means that there is a 19 cm spacing between the upper and the lower cryostat to provide substantial access to the plasma volume. The large amount of optical access is exploited extensively in the $\mathbf{g} \times \mathbf{B}$ drift experiments. An octagonal plasma chamber is mounted inside the magnet bore at the axial mid-plane. The plasma chamber has a circular ID of 35.5 cm and is pictured in Fig. (3.4). The eight outer ports of the octagon are 12.7 cm x 10.2 cm and may be either transparent windows or adapted to standard vacuum fittings (i.e. KF-40, ISO-100, etc.). Inside the chamber, a pair of 30.4 cm diameter electrodes are configured in a parallel plate fashion with a 110 mm spacing. A 13.56 MHz RF signal is applied to the bottom electrode, and the top electrode is grounded. The RF signal is capacitively coupled to the system to create a DC self-bias voltage drop across the sheath. The upper electrode has a circular cutout within which an approximately 100 cm^2 transparent Fluorine-doped tin oxide (FTO) conductive glass plate is mounted. The transparent glass plate is necessary to provide a top-down view of dust grain motion as shown in Figs. (3.1 – 3.2). The neutral gas pressure is measured by an MKS 722B Baratron pressure gauge that is accurate to 0.5% of the measured pressure value.

3.2.1 Reconfiguring MDPX to measure $\mathbf{g} \times \mathbf{B}$ drift

The $\mathbf{g} \times \mathbf{B}$ experiment requires that the magnetic and gravitational fields are perpendicular (due to the cross product) to maximize the amount of deflection. The MDPX device was rotated to the horizontal configuration such that the magnetic field was horizontal and perpendicular to gravity. A Ximea XiQ USB 3.0 camera with 4 Megapixel resolution at 90 FPS (maximum) is mounted to the MDPX device. A 70 to 200 mm Nikon Micro-Nikkor macro lens was mounted to the camera. The CoPlA software was used to manipulate the camera settings and render images. Fig. (3.5) is a schematic view of the experiment in this configuration. Dust grains are dropped vertically downward and into the camera viewing region so that the $\mathbf{g} \times \mathbf{B}$ drift can be observed.

3.2.2 Radio-frequency plasma generation system calibration

The presence of a strong magnetic field may cause catastrophic failure in electronics—particularly electronics which contain iron core inductors and other components which are sensitive to magnetic fields. As a result, it is difficult to obtain plasma discharge measurements because standard electronics cannot be placed in close proximity to the magnetic field. The MDPX RF system uses a RF-VII model 3 RF supply with a RFVII model ATN-20/30 auto-tuning network. In order to measure the peak-to-peak voltage of the RF discharge, a capacitive voltage divider was used. A 2 pF capacitor was placed in parallel to the discharge at the vacuum chamber connection according to the schematic shown in Fig. (3.6a). The 2 pF parallel capacitance does not significantly change the matching impedance of the load while still allowing a (reduced) voltage to be measured far away from the magnetic field. At

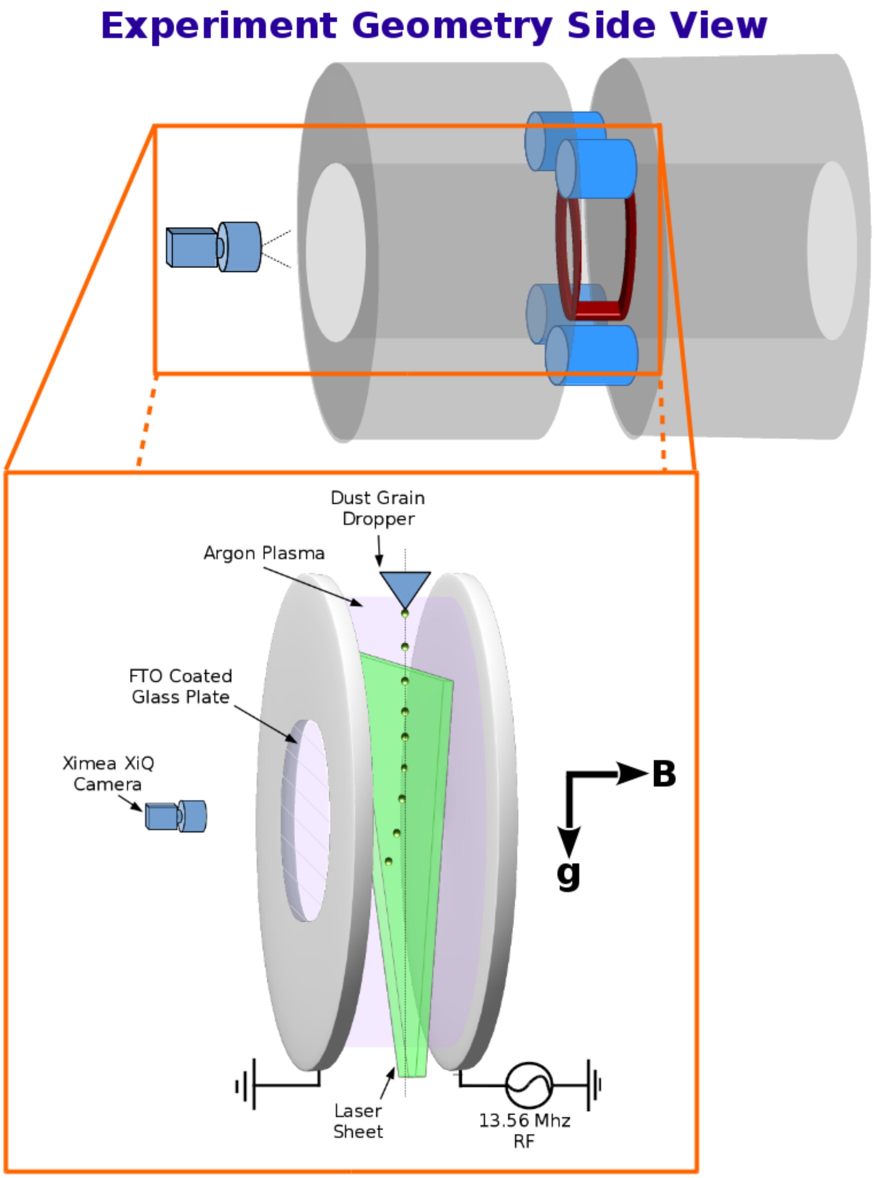

Figure 3.5: An illustration of the geometry necessary to perform the $\mathbf{g} \times \mathbf{B}$ drift experiment. The MDPX device shown in Fig. (3.4) was rotated such that the magnetic field is horizontal and points away from the camera. In this geometry, the magnetic and gravitational fields are perpendicular. The dust grains are dropped vertically downward through the plasma bulk, and they are illuminated by a vertical laser sheet. The falling grains will deflect into the page as a result of the $\mathbf{g} \times \mathbf{B}$ drift.

zero magnetic field, the measured voltage was calibrated using a 10x probe and oscilloscope. A linear fit is performed to provide a conversion equation between the measured voltage after the 2 pF capacitor and the actual voltage measured by the 10x probe as shown in Fig. (3.6b).

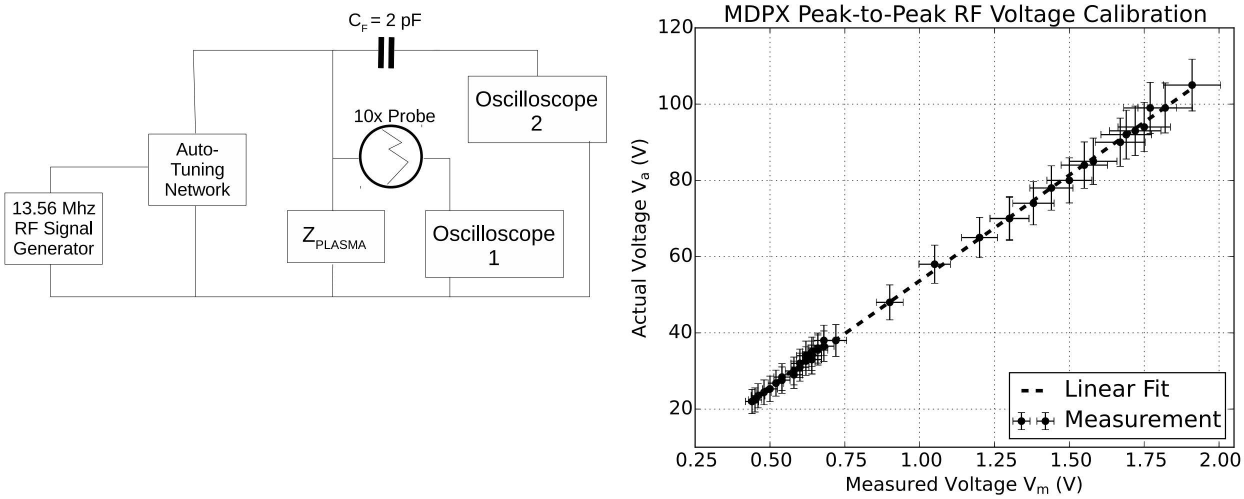

(a)

(b)

Figure 3.6: a) The peak-to-peak RF voltage measurement electrical schematic for MDPX. b) The calibration measurements taken using the circuit outlined in part a). The x-axis was measured using oscilloscope 2, and the y-axis was measured using a 10X probe connected to oscilloscope 1. Eq. (3.1) is the linear fit result that was used to convert between the measured and actual voltage of the RF system.

The conversion factor between the 10x probe measurement and the voltage divider was

$$V_{\mathrm{A}} = (55.46 \pm 0.296)V_{\mathrm{M}} + (-1.089 \pm 0.323)\mathrm{Volts} \tag{3.1}$$

where V_{A} is the actual voltage as measured by the 10x probe, and V_{M} is the voltage reading from the voltage divider.

3.2.3 Spatial calibration of the camera system

In order to extract dimensional information from camera images, a careful absolute scaling of the camera pixel space to physical dimensions must be performed by placing an object of known dimension into the camera field of view. A 12.7 mm long 6.350 mm OD aluminum standoff spacer was placed into the camera field of view. The lens was focused on the spacer and locked in place. The calibration image of the standoff spacer is shown in Fig. (3.7a).

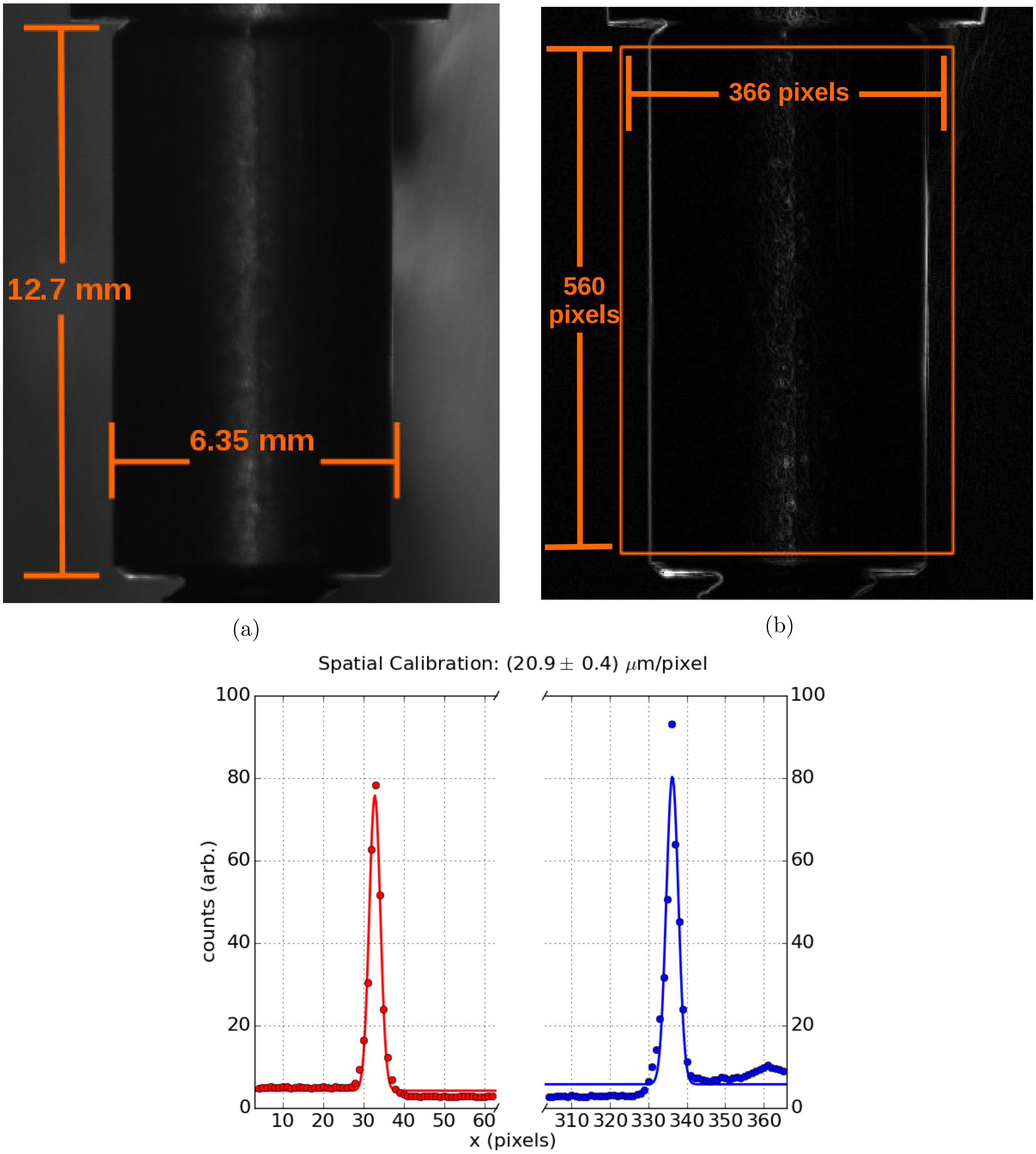

(a)

(b)

(c)

Figure 3.7: Both calibration images shown here are 540 x 651 pixels. a) The 12.70 mm long by 6.350 mm OD aluminum standoff spacer used as the calibration object. b) The Sobel filtered 12.70 mm long by 6.350 mm OD aluminum standoff spacer with a 366 x 560 pixel bounding box. c) The histogram generated by applying Eq. (3.2) over the 560 pixel height of part b). The Gaussian with constant background offset curve fits to the left and right hand side peaks. The resulting spatial resolution was $(20.9 \pm 0.4\ \mu\text{m/pixel})$.

In many cases, due to the lighting conditions of the calibration image, identifying the true edges of the calibration object with an accuracy of better than 2 – 3 pixels can be difficult. For this reason, we use a Sobel edge detection filter[120] to identify the edges of the standoff spacer. The Sobel edge detection filter is a commonly used image processing method for object and feature identification [103, 121]. The Sobel filter calculates the magnitudes of the spatial gradients in an image. When the spatial gradients change rapidly, an edge in the image has been found. A comparison between the raw calibration image and its corresponding Sobel transformed image is shown in Fig. (3.7). In the Sobel transformed image, one can see that the edges of the calibration spacer (the white streaks) are much more clearly defined; however, there is still possibly a several pixel ambiguity in which pixels to select as the definite edge. In order to resolve this ambiguity, we generate a histogram of the Sobel filtered image according to the equation

$$h(i) = \sum_{\mathrm{j=0}}^{\mathrm{N}} G(i, j) \tag{3.2}$$

where (i, j) are the pixel indices and $G(i, j)$ is the 8-bit intensity of the Sobel image at pixel (i, j). Eq. (3.2) is applied to the bounding box of Fig. (3.7b). The resulting histogram is shown in Fig. (3.7c) where the edges of the calibration spacer are the sharp peaks located at approximately x = 40 pixels and x = 335 pixels.

A Gaussian curve fit with a constant background offset was applied to the left and right hand side peaks of Fig. (3.7c). The left peak was located at $x_{\mathrm{o,L}} = (32.84 \pm 0.03)$ pixels and the right peak $x_{\mathrm{o,R}} = (336.22 \pm 0.07)$ pixels. The distance between these two peaks is (303.38 ± 0.08) pixels. The spacer dimension was (6.350 ± 0.127) mm and thus the absolute scaling between pixel space and physical dimensions was $(20.9 \pm 0.4\ \mu\mathrm{m/pixel})$.

Chapter 4

Experiments: Using **g** x **B** Drift to Measure Grain Charge

4.1 An auxiliary experiment to measure neutral gas drag

The previous chapter focused on the characteristics of the MDPX device and the development and application of the software needed to analyze dust grain imaging data. The remaining ingredient to perform the $\mathbf{g} \times \mathbf{B}$ drift experiment is to devise a method through which we can selectively drop single dust grains so that the drift of individual grains can be observed. In this section, we provide design specifications for and test the performance characteristics of a novel single dust grain dropper that is able to reliably drop single dust grains with high spatial precision ($\sim 50\ \mu$m) in a controlled manner. In addition, we use the dropper device to measure the unknown Epstein neutral drag coefficient to remove it as a free parameter from the model developed in Sec. (2.2.1). The single grain dropper device was designed and tested as an auxiliary experiment separate from the MDPX device. The grain dropper performance evaluation discussed in Secs. (4.1.2 – 4.1.3) was not performed in the MDPX device.

4.1.1 Designing a device to drop single dust grains

The single grain dropper is effectively a small RF secondary plasma device that contains a reservoir of suspended dust grains. The amplitude of the applied RF voltage is manipulated to selectively allow the release of single grains in a controlled manner. The design of the single grain dropper is based on a parallel plate, capacitively coupled RF plasma source. The parallel plate electrodes are mounted inside a glass cylinder which confines the plasma radially and aids in maintaining the symmetry of the plasma discharge. A cartoon sketch of the grain dropper is shown in Fig. (4.1).

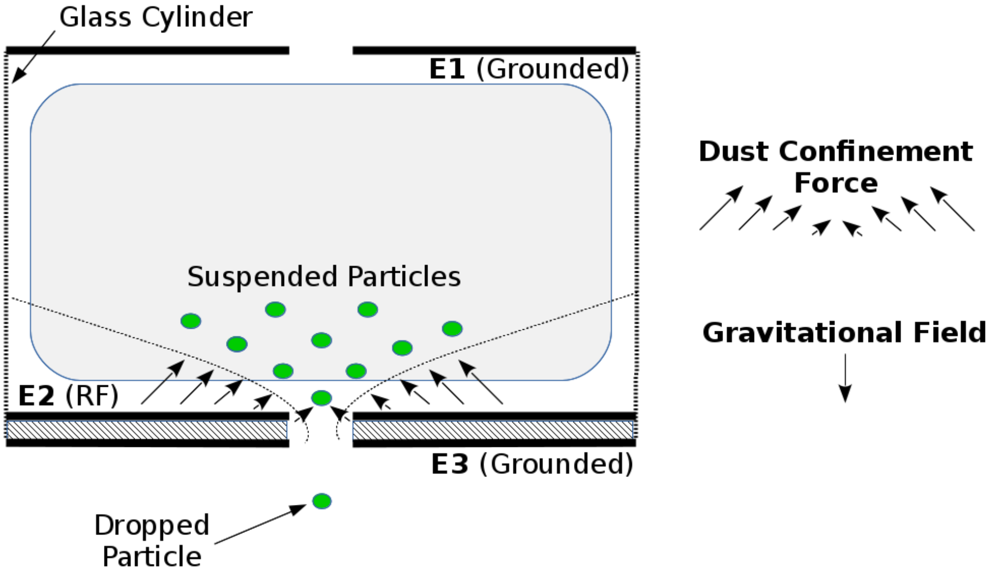

Figure 4.1: An illustration of the dust dropper configuration. A 13.56 MHz RF signal is applied to electrode E2. The peak-to-peak voltage of the RF signal is gradually reduced until the vertical component of the confinement force that is provided by the plasma sheath electric field can no longer support the bottom-most grain.

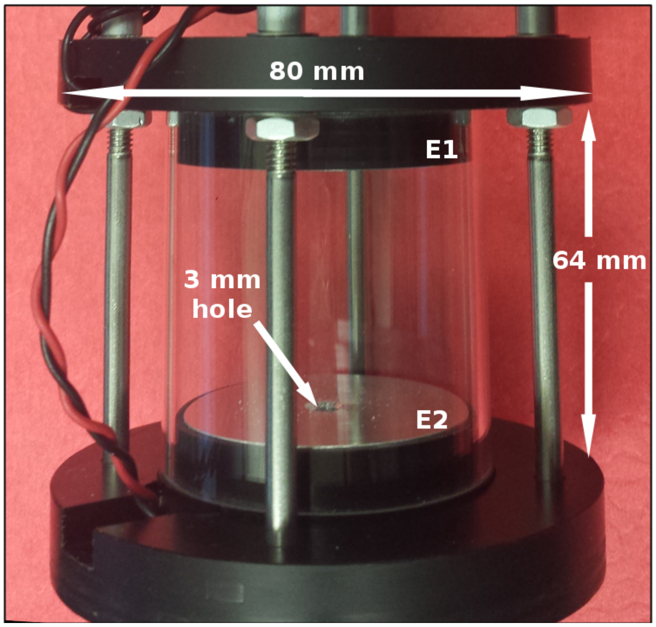

Figure 4.2: A picture of the dropper and mounting hardware assembly. The modularity of the dropper assembly and the mounting hardware provides variable electrode spacing by changing the length of the confining glass cylinder. Detailed dimensional drawings of the device are provided in Appendix A.

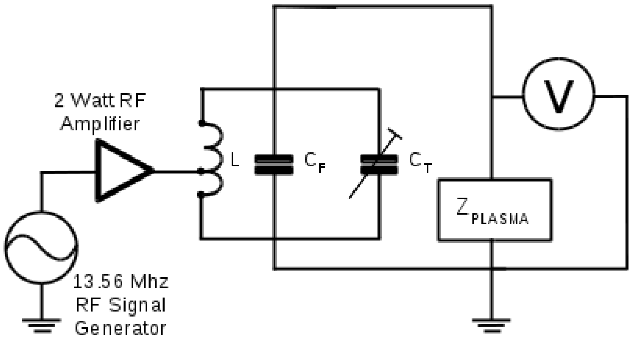

Figure 4.3: An electrical schematic of the dropper RF network that is used to power E2. The trimmer capacitor, C_T, ranges from 10-150 pF. The single air coil inductor, L, has an inductance of approximately 1 μH, and the shunt capacitor, C_F is approximately 50 pF.

All three dropper electrodes have a diameter of 41.27 mm as well as a 3.175 mm diameter central hole. Electrode 1 is labeled as E1 in Figs. (4.1 – 4.2) and is grounded. Electrode 2 (E2) has an applied 13.56 MHz RF signal. Electrode 3 (E3) is approximately 10 mm beneath electrode E2. E3 was included in the design to serve two purposes: confining the plasma generated between E2 and E1 such that no plasma appears below the dropper, and in some cases, manipulate the sheath ions above E2 with a DC signal to assist with dropping grains. In all single grain dropper experiments performed in this dissertation, E3 was grounded because the auxiliary DC signal was not required to drop grains. The mounting hardware shown in Fig. (A.2) was used to attach the dropper to an standard ISO-100 vacuum port.

We use a Rigol DG4062 Signal Generator as input to a generic 2 Watt HAM (amateur) radio amplifier. A standard L-network, as sketched in Fig. (4.3), is used to match the 50 Ω amplifier (source) and the plasma (load) impedance. The plasma ignites at a typical peak-to-peak voltage of 200 volts and can be sustained for voltages down to 40 volts.

The dust grains are inserted into the dropper plasma using a standard dust shaker located approximately 10 cm above electrode E1 and the mounting hardware. A standard dust shaker is analogous to a table-top “salt shaker”. A small amount of dust ($\sim$ 1 cm^3) is stored behind a fine metallic mesh that is placed inside the vacuum chamber. The standard dust shaker is mechanically agitated from outside the vacuum chamber. The dust grains fall through the central hole in electrode E1 and into the plasma region. When the dust grains enter the plasma, they very quickly become charged within microsecond timescales as discussed in Sec. (1.2). The dust grains are then suspended by the vertical component of the sheath electric field above electrode E2.

There is a 60 degree flare angle on the 3.175 mm central hole in electrode E2 to provide an additional radial confinement force for only the central-most dust grains. When the RF voltage applied to E2 is reduced, the vertical confinement weakens until it is no longer able to support the bottom-most grain and it falls out of the device. Depending on the number of suspended grains, the confinement force begins to drop grains when the peak-to-peak voltage applied to E2 is reduced to approximately 90 – 100 volts. When fewer grains are present (i.e. there are fewer grains on top "pushing" down on the bottom-most grain), the voltage may need to be reduced as low as 70 volts. The precision with which the dust grains are dropped is critically dependent on the size of the hole that is opened in the confinement force. For this reason, we devote the next section to analyzing the grain dropper's precision performance.

4.1.2 Evaluating grain dropping precision

The precision of the single grain dropper is evaluated over the pressure range (23.9 – 85.3) Pa. The pressure was measured using a MKS-722B Baratron gauge that has a measurement uncertainty of 0.5%. At each pressure setting, multiple dust grains with a radius $a_{\mathrm{d}} = (4 \pm 0.4)$ μm radius are individually dropped over a 500 image sequence. The CoPlA software was used to compute the per pixel standard deviation image from the sequence using the expressions

$$\sigma^2_{\mathrm{i,j}} = \sum_{\mathrm{k=1}}^{\mathrm{N}} \frac{(I^{\mathrm{k}}_{\mathrm{i,j}} - < I_{\mathrm{i,j}} >)^2}{\mathrm{N}-1} \tag{4.1}$$

and

$$< I_{\mathrm{i,j}} >= \sum_{\mathrm{k=1}}^{\mathrm{N}} \frac{I^{\mathrm{k}}_{\mathrm{i,j}}}{\mathrm{N}} \tag{4.2}$$

where (i,j) are the spatial coordinate indices of pixels, $I_{i,j}^{k}$ is the (i,j) pixel intensity at frame number k, N = 500 frames, and $< I_{\mathrm{i,j}} >$ is the per pixel average intensity over the 500 frame sequence. The standard deviation image created using Eqs. (4.1 – 4.2) is referred to as the composite image. The falling grains are illuminated using a 632 nm 100 mW laser spread into an approximately 1 mm thick by 4 cm wide laser sheet. The grains are imaged during a 10 ms exposure using an Ximea XiQ USB 3.0 4 MP camera equipped with a Nikon Micro-Nikkor 60 mm f/2.8D lens. The spatial resolution is 25 μm/pixel in this system.

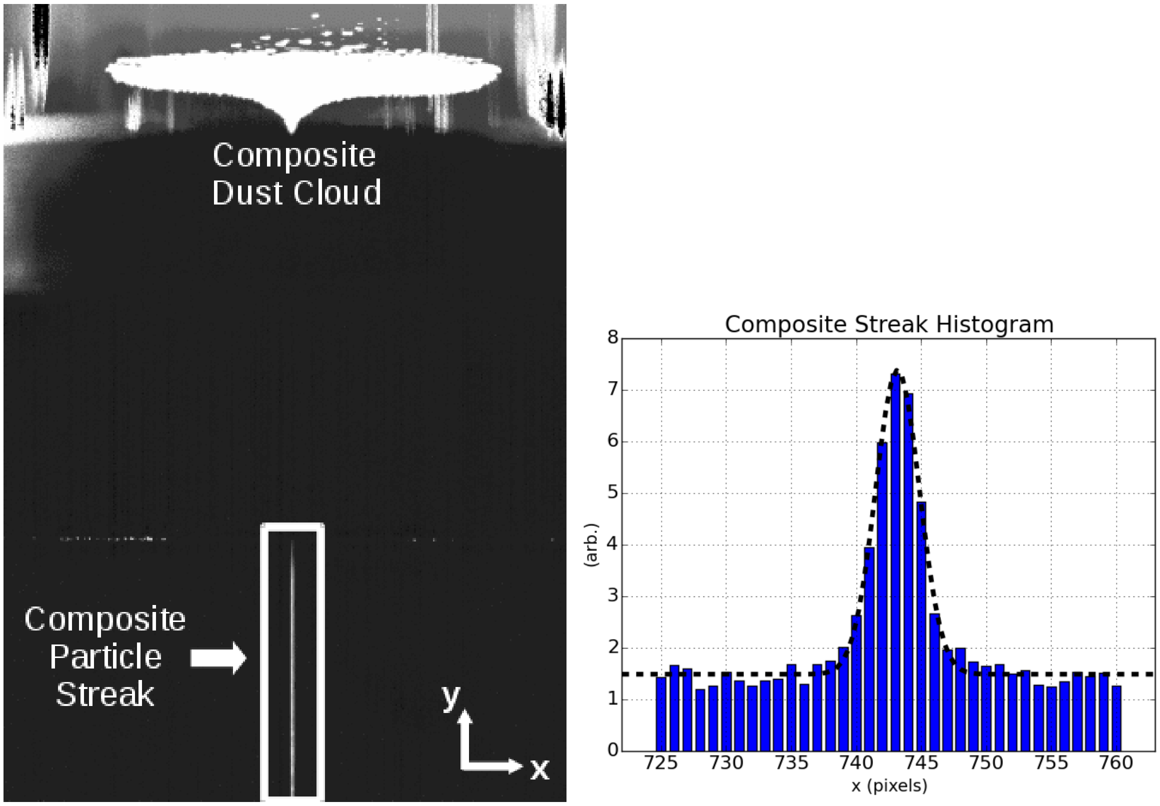

(a) (b)

Figure 4.4: a) A composite image formed by computing the standard deviation of 500 images according to Eqs. (4.1) and (4.2). b): The grain streak x-position histogram formed by summing over the bottom 575 pixels of the composite image. The dashed black line is the Gaussian curve fit of the histogram data.

The bottom 575 pixels (1.43 cm) of the composite image are then used to generate a histogram that represents the distribution of all dust grain trajectories during the 500 image sequence. An example composite image and its dropped grain trajectory histogram are shown in Fig. (4.4). The histogram is then curve fit to a Gaussian distribution with an additive background constant. The composite streak variance, σ^2_{total}, is obtained from the curve fit. The composite streak variance can be decomposed as

$$\sigma^2_{\text{total}} = \sigma^2_{\text{grain}} + \sigma^2_{\text{streak}} \tag{4.3}$$

where $\sigma^2_{\text{grain}} \approx 1.5$ pixels^2 is the average variance of grain images, and σ^2_{streak} is the variance of dropped grain trajectories. The variance of the dropped grains trajectories depends on three factors: the size of the opening in the confinement force, the neutral gas pressure (due to neutral drag), and the vertical alignment of the camera system. In this analysis, we do not include the vertical mis-alignment of the camera system because the values obtained for σ_{streak} were 1 – 2 pixels, which means that the camera was already relatively well aligned.

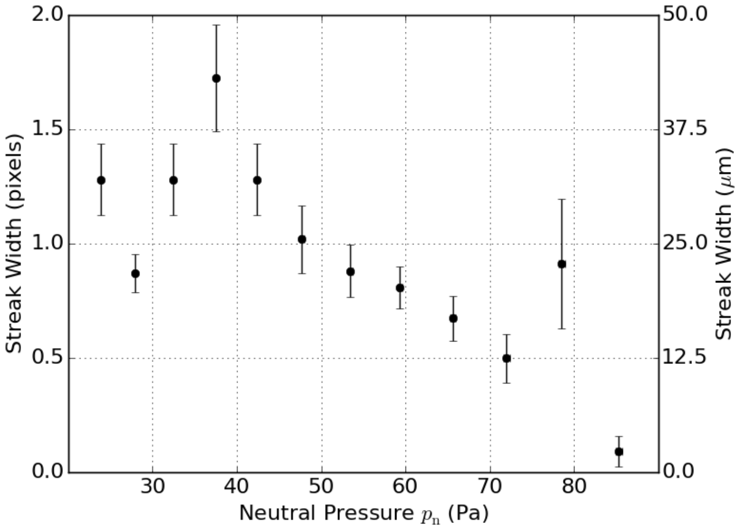

Figure 4.5: The streak width $\sigma_{\text{streak}} = \sqrt{\sigma^2_{\text{total}} - \sigma^2_{\text{grain}}}$ versus neutral pressure p_{n} range (23.9 – 85.3) Pa. The y-axis error bars were obtained from the uncertainty in the σ_{total} and σ_{grain} fits. The x-axis error bars were obtained from the gas pressure uncertainty, 0.5%, which is too small to be seen on this scale.

The results of the grain dropping precision experiment are summarized in Fig. (4.5) where the streak width σ_{streak} is plotted the neutral gas pressure p_{n}. The x-axis uses this scaling so that the uncertainty in both the grain size distribution and the neutral gas pressure measurement can be included in the analysis. Based on these results, we conclude that even in the worst case scenario at lower pressures where neutral gas drag is weak, the single grain dropper is able to consistently drop grains to within a region of, at most, about 2 pixels = 50 μm. In Sec. (2.3), we showed that even in a relatively weak magnetic field of $B_{\mathrm{z}} = 0.5$ T with an OML dust grain charge of $Z_{\mathrm{d}} = 840$ electrons at a neutral gas pressure of $p_{\mathrm{n}} = 0.67$ Pa, the dust grain deflection will be of the order 500 μm. Therefore, the single dust grain dropper precision of 50 μm more than sufficient to perform the $\mathbf{g} \times \mathbf{B}$ drift experiment.

4.1.3 Measurement of the neutral gas drag

The dropper device was also used to remove a free parameter from the grain deflection model. From Eq. (2.26), the asymptotic deflection angle is inversely proportional to the neutral gas drag, which contains an unknown Epstein coefficient, δ, that was discussed in Sec. (1.2.5). δ has been extensively measured and usually has a value of $\sim 1.3 - 1.5$. However, although its value is well established, it is usually left as a free fitting parameter in experiment model solutions. In the case of the $\mathbf{g} \times \mathbf{B}$ experiment, measuring δ for the silica grains bears the substantial benefit of reducing the number of free parameters from two to one, which leaves the dust grain charge as the only unknown in the model. For this reason, this section is devoted to performing a measurement of δ for silica dust grains in neutral Argon gas.

Falling grain model

When a dust grain is dropped by lowering the RF voltage applied to electrode E2, it falls through the central hole in electrode E2 and the mounting hardware and then enters a plasma free region beneath the grounded E3 electrode as shown in the inset image of Fig. (4.6). In the absence of plasma, the only two forces acting on the grain are the gravitational force

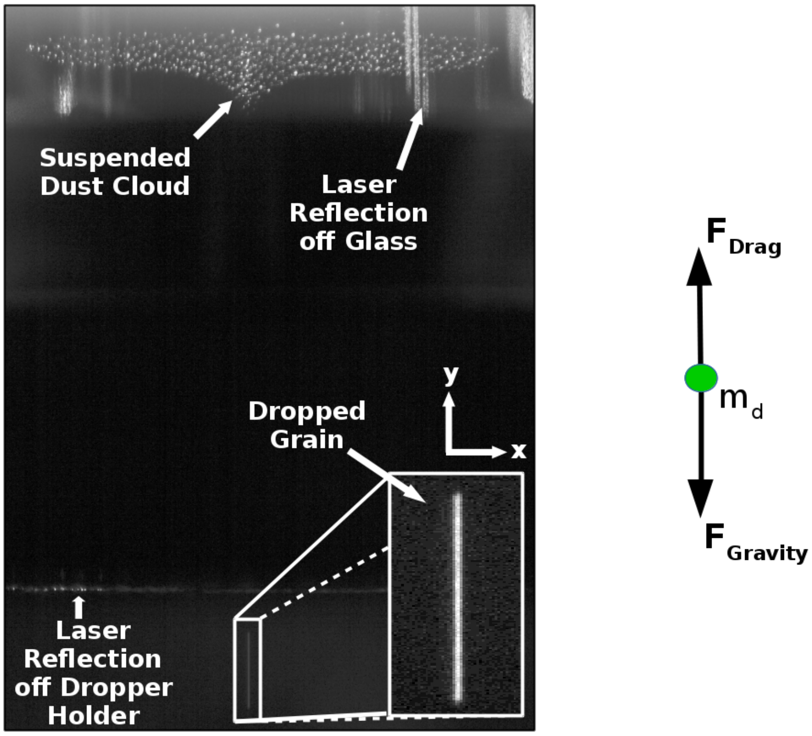

Figure 4.6: On the left, an example of a suspended dust cloud and a dropped dust grain in the bottom region. The grain trajectory is a streak and represents the distance traveled during the 10 ms camera exposure. On the right, a force diagram for a falling dust grain in the absence of plasma. In the falling grain region, there is no plasma and the grain is subject to only the gravitational force $\mathbf{F}_{\text{Gravity}}$ and the neutral gas drag $\mathbf{F}_{\text{Drag}}$.

and the neutral gas drag. The equation of motion is

$$\frac{d^2y}{dt^2} = -g - \Gamma\frac{dy}{dt} \tag{4.4}$$

where m_{d} is the mass of the falling dust grain, y is the time-dependent vertical position of the grain, g is the Earth's gravitational constant (9.8 m/s^2), and Γ is the Epstein expression for the neutral gas drag that is given by Eq. (1.27). The solution to Eq. (4.4) is not included in the main text and is derived in Appendix B. The solution is

$$y - y_{\text{o}} = -\frac{1}{\Gamma^2}[\Gamma v_{\text{o}} + g]\exp[-\Gamma(t - t_o)] - \frac{g}{\Gamma}(t - t_{\text{o}}) \tag{4.5}$$

where t_o is the initial time, y_o is the initial position, and v_o is the initial velocity. In the limiting case where $\Gamma(t - t_o) \gg 1$ (i.e., when terminal speed has been reached), Eq. (4.5) reduces to

$$y - y_o = -\frac{g}{\Gamma}(t - t_o) = -v_{\text{term}}(t - t_o) \tag{4.6}$$

where $v_{\text{term}} = g/\Gamma$ is the terminal speed. The terminal speed approximation is used extensively in the following measurements.

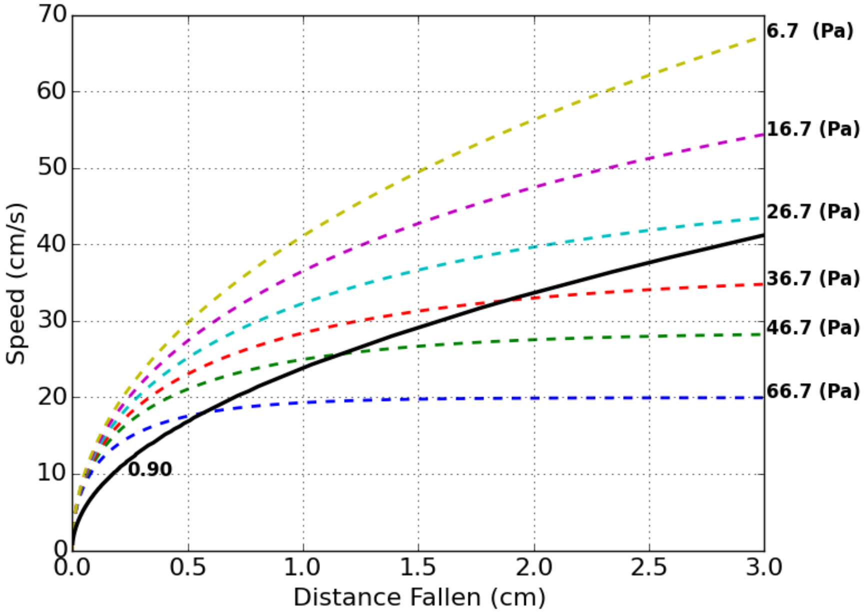

Figure 4.7: The thick dashed curves (from bottom to top) are falling grain speed versus distance curves for the following Argon gas pressures: (66.7, 46.7, 36.7, 26.7, 16.7, 6.7) Pa. The curves were generated using the following parameters: $\delta = 1$, $k_b T_n = 0.025$ eV, $a_d = 4$ μm, $\rho_d = 2.2$ g/cm^3. The initial conditions for Eq. (4.5) were: $t_o = 0$, $v_o = 0$, and $y_o = [\Gamma v_o + g]/\Gamma^2$ so that $y(0) = 0$. The solid curve labeled by 0.90 is the contour below which grains have reached 90% of their terminal speed (i.e. where Eq. (4.6) is valid).

The electrodes and mounting hardware are not transparent, which means that we do not know a priori the exact location at which the grains begin their free fall motion nor do we know any temporal information about the falling grain before it enters the observation region in Fig. (4.6). There is an approximately 2 cm distance between the dust cloud sheath confinement region above electrode E2 and the observation region. Due to the terminal speed approximation, it is important that we restrict the experimental neutral gas pressures such that the observed falling dust grains are guaranteed to reach close to terminal speed by the time they reach the observation region. We estimate the falling grain speed by plotting phase space curves of Eq. (4.5) at several different neutral gas pressures based on the conservative estimate of $\delta = 1$ where the neutral drag is weakest and therefore the calculated grain speed is an upper limit. The results are summarized in Fig. (4.7) where it is shown that the dust grain's speed will be at least 90% of the terminal speed at y = 2 cm when $p_{\mathrm{n}} \geq 36.7$ Pa.

Falling grain measurements

We selectively drop single $a_{\mathrm{d}} = (4 \pm 0.4)$ μm radius silica grains with a mass density of $\rho_{\mathrm{d}} = 2.2$ g/cm^3 and measure the length of the grain streaks in the plasma free region shown in Fig. (4.6). This is performed at several different neutral gas pressures in the range (37.5 – 85.3) Pa. The falling dust grains are imaged using the same camera and software system discussed in Sec. (4.1.2). The CoPlA software is used to determine the length of the light streaks corresponding to individually dropped dust grains. The measured streak lengths are then converted to a terminal speed according to the expression

$$v_{\mathrm{term}} = \frac{|y - y_{\mathrm{o}}|}{t - t_{\mathrm{o}}} = \frac{g}{\Gamma} = \frac{g}{\delta}\sqrt{\frac{\rho_{\mathrm{d}}^2 \pi k_{\mathrm{b}} T_{\mathrm{n}}}{8 m_{\mathrm{n}}}}\frac{a_{\mathrm{d}}}{p_{\mathrm{n}}}. \tag{4.7}$$

where $y(t) - y_{\mathrm{o}}$ is the measured streak length and $t - t_{\mathrm{o}}$ is the 10 ms camera exposure time.

The terminal speed data is plotted in Fig. (4.8) along with a corresponding linear fit using Eq. (4.7). The Epstein coefficient, δ, is obtained from the slope of the linear fit. The fit results yield $\delta = (1.443 \pm 0.007)$, which is in agreement with previous experiments [49, 50, 42, 51]. The error estimate of 0.007 was obtained from the standard error of the slope estimate given by the Orthogonal Distance Regression (ODR) method [122]. It is important to note that the linear fit error may not contain all possible sources of error. For example, there may be an error associated with the mass density specified by the dust grain manufacturer. The dust grain manufacturer specifies a mass density value of ρ_{d}= 2.2 g/cm^3,

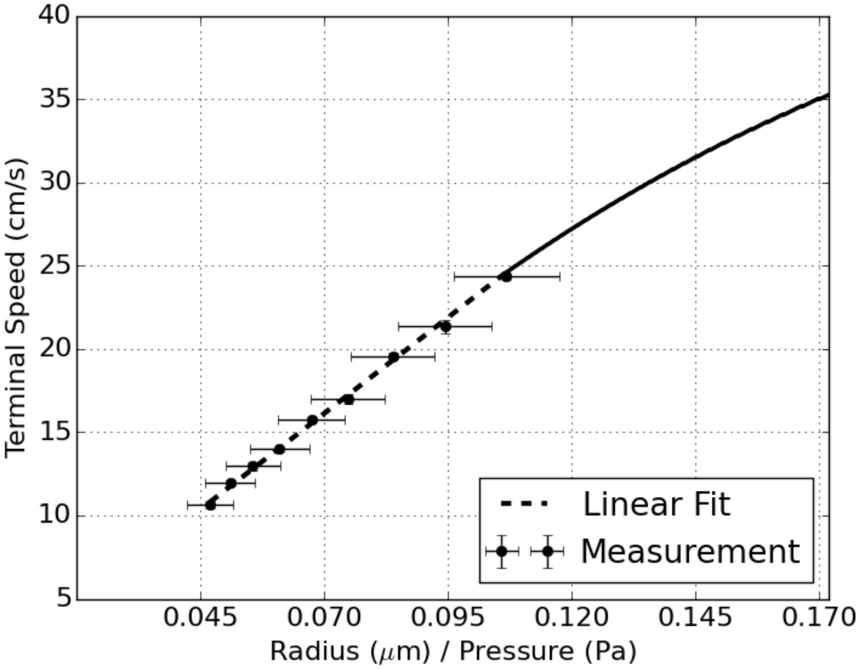

Figure 4.8: The length of ten grain streaks during a 10 ms exposure is measured and plotted on a linear scaling according to Eq. (4.7) at neutral pressures ranging from (37.5 – 85.3) Pa. The y-axis error bars (most are too small to be seen) are plotted using the standard error of the mean streak length measurement (i.e., $\sigma/\sqrt{N}$). The x-axis error bars are obtained using standard error propagation to combine the gas pressure uncertainty, 0.5 %, with the grain size distribution uncertainty, 10%. The dashed line between points is the linear fit to the data that was used to obtain the Epstein coefficient, δ. The solid line is a continuation of the model at lower pressures where measurements would begin to deviate from the linear terminal speed approximation.

but does not specify an uncertainty for this value. Therefore, we estimate a mass density error of 5 %, which is then combined with the curve fit error. The resulting value of the Epstein coefficient is in this case $\delta = (1.443 \pm 0.072)$.

4.1.4 Dropper device performance in strong magnetic fields

In this section, the performance of the single grain dropper is evaluated in strong magnetic fields using the MDPX device. This evaluation will determine if the dropper can be used to perform the $\mathbf{g} \times \mathbf{B}$ drift experiment to measure the deflection of single grains. Fig. (4.9) illustrates the geometry required to use the dropper to perform the $\mathbf{g} \times \mathbf{B}$ drift experiment. With the exception of an additional external magnetic field that is parallel to the electrode surface, the geometry is the same as the experiments performed in Sections (4.1.1 and 4.1.3).

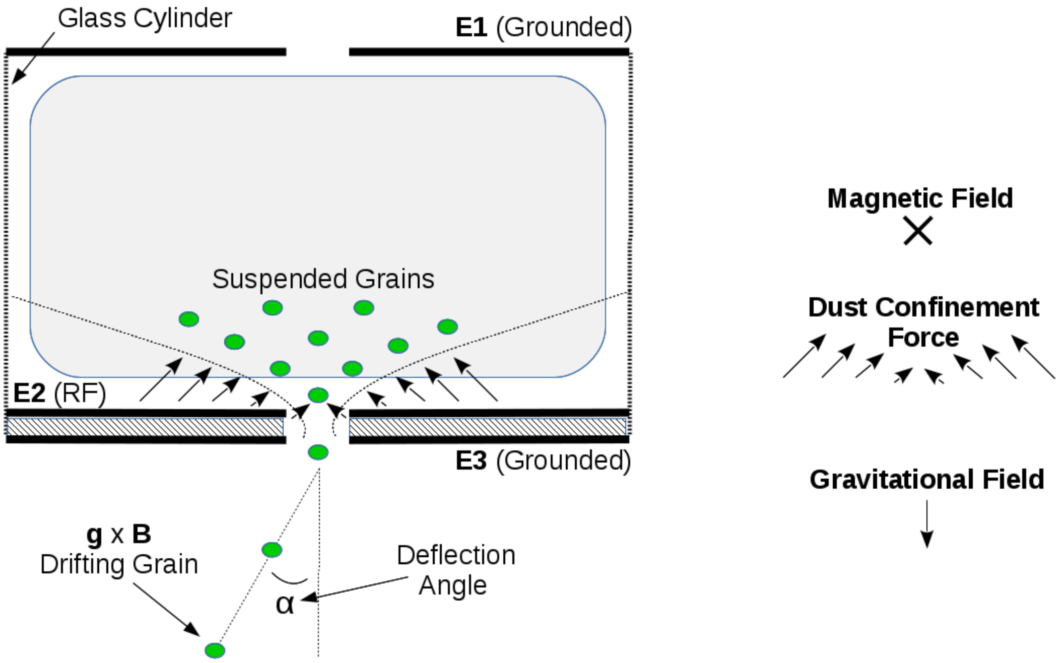

Figure 4.9: An illustration of the geometry required to use the single grain dropper in the $\mathbf{g} \times \mathbf{B}$ drift experiment. The deflection angle, α, is the same as defined in Eq. (2.26) and shown in Fig. (2.4). The magnetic field is into the page parallel to the electrode surface, and the vertical component of the dust confinement force is anti-parallel to the downward gravitational field. In order for the dropper to function as demonstrated in Secs. (4.1.1) and (4.1.3), a plasma must be generated between electrodes E2 and E1, which requires electrons to travel perpendicular to the magnetic field.

For the dropper performance testing, the dropper was mounted inside the MDPX plasma chamber using an ISO-100 port. The dropper electrode surface was parallel to the external magnetic field of MDPX according to the geometry of Fig. (4.9). At B = 0 T and a neutral Argon pressure of $p_\mathrm{n} = 6.67$ Pa, a plasma is ignited between electrodes E1 and E2 using the same technique outlined in Sec. (4.1.1). The magnetic field was increased from B = 0 T to B = 0.1 T while maintaining the dropper plasma. We found that as the magnetic field strength was increased, the dropper plasma was no longer confined within the glass cylinder between electrodes E1 and E2 (perpendicular to the magnetic field). The dropper plasma was instead generated between E2 and other conducting surfaces within the MDPX chamber along the

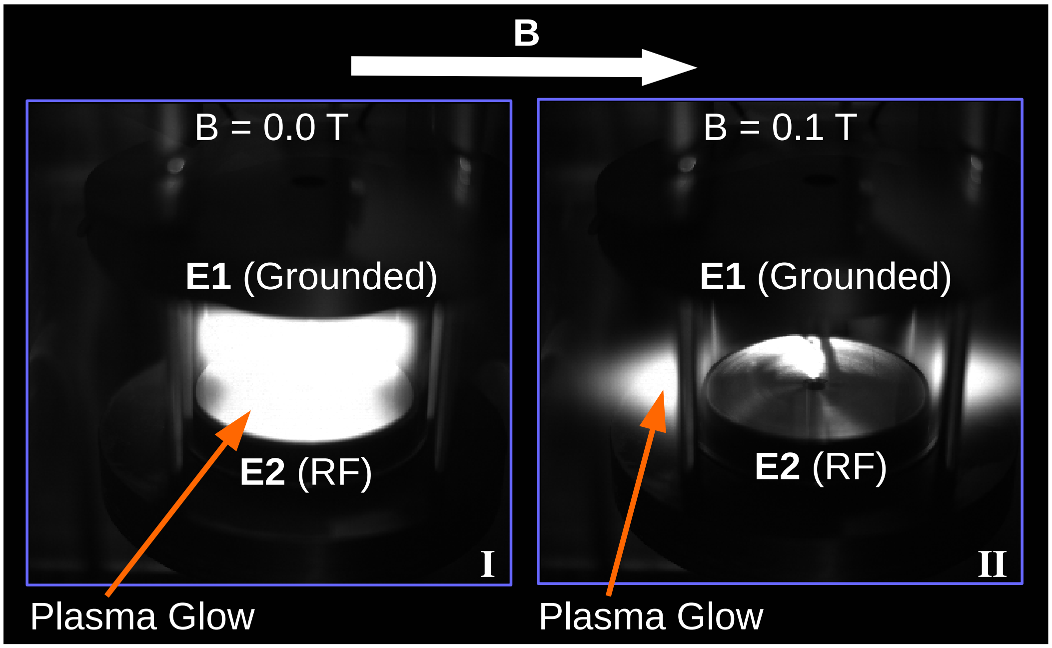

Figure 4.10: In both figures, electrode E1 was grounded and electrode E2 had an applied RF 13.56 MHz signal. The neutral Argon gas pressure was $p_{\mathrm{n}} = 6.67$ Pa. Inset image I is the B = 0.0 T case where the plasma is confined within the glass cylinder between electrodes E1 and E2. Inset image II shows that at B = 0.1 T, the plasma is no longer confined within the glass cylinder between electrodes E1 and E2 and is preferentially generated a long the magnetic field.

direction parallel to the magnetic field. This effect is shown in Fig. (4.10). Based on this observation, we conclude that the dropper cannot be used in the configuration illustrated in Fig. (4.9) to perform the dust grain $\mathbf{g} \times \mathbf{B}$ measurements. In this geometry, the addition of a magnetic field clearly breaks the sheath confinement symmetry that is required to precisely and reliably drop single dust grains as demonstrated in Secs. (4.1.1 – 4.1.3).

In rest of this section, we develop a model to explain why the single grain dropper is unable to maintain plasma confinement between electrodes E1 and E2 (i.e., within the glass cylinder) when a strong magnetic field is applied parallel to the electrode surface. The following model is based on common plasma physics arguments found in textbooks [123, 124, 25]— although the case of weakly-ionized low temperature plasmas is usually paid little attention. We start from the standard Magneto-hydrodynamic (MHD) electron momentum equation:

$$m_\mathrm{e} n_\mathrm{e} \frac{d\mathbf{u}_\mathrm{e}}{dt} = -n_\mathrm{e} e(\mathbf{E} + \mathbf{u}_\mathrm{e} \times \mathbf{B}) - \nabla P_\mathrm{e} + \frac{\delta_\mathrm{c} \mathbf{p}_\mathrm{e}}{\delta t} \tag{4.8}$$

where m_e is the electron mass, n_e is the electron number density, $\mathbf{u}_\mathrm{e}$ is the average velocity, e is the electron charge, $\mathbf{E}$ is the electric field, $\mathbf{B}$ is the magnetic field, P_e is the electron pressure, and $\frac{\delta_\mathrm{c} \mathbf{p}_\mathrm{e}}{\delta t}$ is a generic expression used to represent a collisional drag force on the electrons. Qualitatively, from left to right in Eq. (4.8), we have the rate of change of the electron momentum density, the electromagnetic force density acting on the electrons, the force density on electrons resulting from pressure (or density) gradients, and a collisional drag force per unit volume.

In low temperature weakly-ionized plasmas (such as those used in most dusty plasma experiments) where the ionization fraction is of the order 10^{-6} – 10^{-7}, the electrons more frequently collide with neutral atoms than ions or with other electrons. The collisional drag term of Eq. (4.8) can be greatly simplified by applying the Lorentz gas model [125, 126, 127] to electron-neutral collisions. In the Lorentz gas model, a point particle (i.e., the electron) travels through the gas and undergoes periodic elastic collisions with stationary scatterers (i.e., the neutral atoms). The approximation of stationary neutrals is appropriate because the electron thermal speed of $k_\mathrm{b} T_\mathrm{e} = 2$ eV electrons is $v_\mathrm{th,e} \sim 10^6$ m/s, which is much larger than the room temperature $k_\mathrm{b} T_\mathrm{n} = 0.025$ eV neutral Argon thermal speed of $v_\mathrm{th,n} \sim 10^3$ m/s. The large difference in characteristic speeds means that the neutrals are effectively at rest with respect to the electrons. The Lorentz gas model for elastic electron-neutral collisions is

$$\frac{\delta_\mathrm{c} \mathbf{p}_\mathrm{e}}{\delta t} = -\nu_\mathrm{e,n} m_\mathrm{e} n_\mathrm{e} \mathbf{u}_\mathrm{e} \tag{4.9}$$

where $\nu_\mathrm{e,n}$ is the electron-neutral collision frequency. For $k_\mathrm{b} T_\mathrm{e} = 2.0$ eV electrons colliding with room temperature neutral Argon at $p_\mathrm{n} = 6.67$ Pa, $\nu_\mathrm{e,n} \sim 10^6$ Hz. When substituting

Eq. (4.9) into Eq. (4.8), the electron momentum equation becomes:

$$m_\mathrm{e} n_\mathrm{e} \frac{d\mathbf{u}_\mathrm{e}}{dt} = -n_\mathrm{e} e(\mathbf{E} + \mathbf{u}_\mathrm{e} \times \mathbf{B}) - \nabla P_\mathrm{e} - \nu_\mathrm{en} m_\mathrm{e} n_\mathrm{e} \mathbf{u}_\mathrm{e}. \tag{4.10}$$

We further assume that the plasma is in equilibrium where $\frac{d}{dt} \to 0$ — meaning that the RF field is neglected. However, at the end, we briefly outline how the motion of the electrons due to the RF field can be included. We also assume that there are no pressure (or density) gradients in the electron population such that $\nabla P = 0$ and Eq. (4.10) becomes

$$0 = -e(\mathbf{E} + \mathbf{u}_\mathrm{e} \times \mathbf{B}) - \nu_\mathrm{en} m_\mathrm{e} \mathbf{u}_\mathrm{e} \tag{4.11}$$

When the cross-product is expanded of Eq. (4.11) and making the substitutions $\mathbf{B} = B_\mathrm{z}\hat{\mathbf{z}}$, $\mu_\mathrm{e,n} = e/m_\mathrm{e}\nu_\mathrm{e,n}$ (the electron mobility), $\omega_\mathrm{c,e} = eB_\mathrm{z}/m_\mathrm{e}$ (the Larmor frequency), and decoupling the system by solving for either u_x or u_y and using back-substitution, the system of equations becomes

$$(1 + H_\mathrm{e}^2) u_\mathrm{e,x} = -\mu_\mathrm{en} E_\mathrm{x} + H_\mathrm{e}^2 \frac{E_\mathrm{y}}{B_\mathrm{z}} \tag{4.12}$$

$$(1 + H_\mathrm{e}^2) u_\mathrm{e,y} = -\mu_\mathrm{e,n} E_\mathrm{y} - H_\mathrm{e}^2 \frac{E_\mathrm{x}}{B_\mathrm{z}} \tag{4.13}$$

$$u_\mathrm{e,z} = -\mu_\mathrm{e,n} E_\mathrm{z} \tag{4.14}$$

where $H_\mathrm{e} = \omega_\mathrm{c,e}/\nu_\mathrm{e,n}$ is the electron Hall parameter from Eq. (1.12).

The average electron velocity, $\mathbf{u}_\mathrm{e}$, can be related to the current density using $\mathbf{J}_\mathrm{e} = -en_e\mathbf{u}_\mathrm{e}$ as well as the electric field by applying Ohm's Law, $\mathbf{J}_\mathrm{e} = \boldsymbol{\sigma} \cdot \mathbf{E}$ (where $\boldsymbol{\sigma}$ is the conductivity tensor). These two expressions are summarized as

$$\mathbf{J}_\mathrm{e} = -en_\mathrm{e}\mathbf{u}_\mathrm{e} = \boldsymbol{\sigma} \cdot \mathbf{E}. \tag{4.15}$$

By inspection, Eqs. (4.12 – 4.14) can now be rearranged and expressed in terms of the conductivity tensor (also note that $H_{\rm e}^2/B_{\rm z} = \mu_{\rm e,n}\omega_{\rm c,e}/\nu_{\rm e,n}$)

$$\begin{pmatrix} J_{\rm e,x} \\ J_{\rm e,y} \\ J_{\rm e,z} \end{pmatrix} = -en_{\rm e} \begin{pmatrix} u_{\rm x} \\ u_{\rm y} \\ u_{\rm z} \end{pmatrix} = \frac{-e^2 n_{\rm e}}{m_{\rm e}\nu_{\rm e,n}(1+H_{\rm e}^2)} \begin{pmatrix} 1 & H_{\rm e} & 0 \\ -H_{\rm e} & 1 & 0 \\ 0 & 0 & (1+H_{\rm e}^2) \end{pmatrix} \begin{pmatrix} E_{\rm x} \\ E_{\rm y} \\ E_{\rm z}. \end{pmatrix}. \tag{4.16}$$

The conductivity tensor, in component form, is given as

$$\boldsymbol{\sigma} = \begin{pmatrix} \sigma_\perp & \sigma_{\rm H} & 0 \\ -\sigma_{\rm H} & \sigma_\perp & 0 \\ 0 & 0 & \sigma_\parallel \end{pmatrix} \tag{4.17}$$

where

$$\sigma_\perp = \frac{\sigma_{\rm o}}{1+H_{\rm e}^2}, \tag{4.18}$$

$$\sigma_{\rm H} = H_{\rm e}\frac{\sigma_{\rm o}}{1+H_{\rm e}^2}, \tag{4.19}$$

and

$$\sigma_\parallel = \sigma_{\rm o} = \frac{e^2 n_{\rm e}}{m_{\rm e}\nu_{\rm en}}. \tag{4.20}$$

The perpendicular conductivity, $\sigma_\perp$, corresponds to current flow along the component of the electric field that is normal to the magnetic field, the off-diagonal conductivity, $\sigma_{\rm H}$, corresponds to current flow that is flowing both normal to the electric and magnetic field, and parallel electron conductivity, $\sigma_\parallel$, is the current flow along the direction of the magnetic field. $\sigma_\parallel$ is the steady-state DC conductivity that is independent of the magnetic field. A graphical comparison of the normalized components of the conductivity tensor is shown in Fig. (4.11a).

In the context of the dropper plasma no longer being confined to the glass cylinder as illustrated in Fig. (4.10), the perpendicular conductivity given by Eq. (4.18) decreases as $\sim$

$1/H_\mathrm{e}^2$. In other words, the electrons become so strongly magnetized that they are unable to travel perpendicular to the magnetic field and therefore cannot cross the gap between electrodes E1 and E2. To a certain extent, this effect can be mitigated by increasing the neutral gas pressure, but if one desires to perform the experiment at low neutral gas pressures, then increasing the neutral pressure is not feasible. Fig. (4.11a) is a plot of the electron conductivity tensor components versus the electron Hall parameter and it is clearly shown that even for moderately magnetized electrons where $H_\mathrm{e} \sim 10$, the perpendicular conductivity has fallen to only a few % of its nominal unmagnetized value. In addition, contours

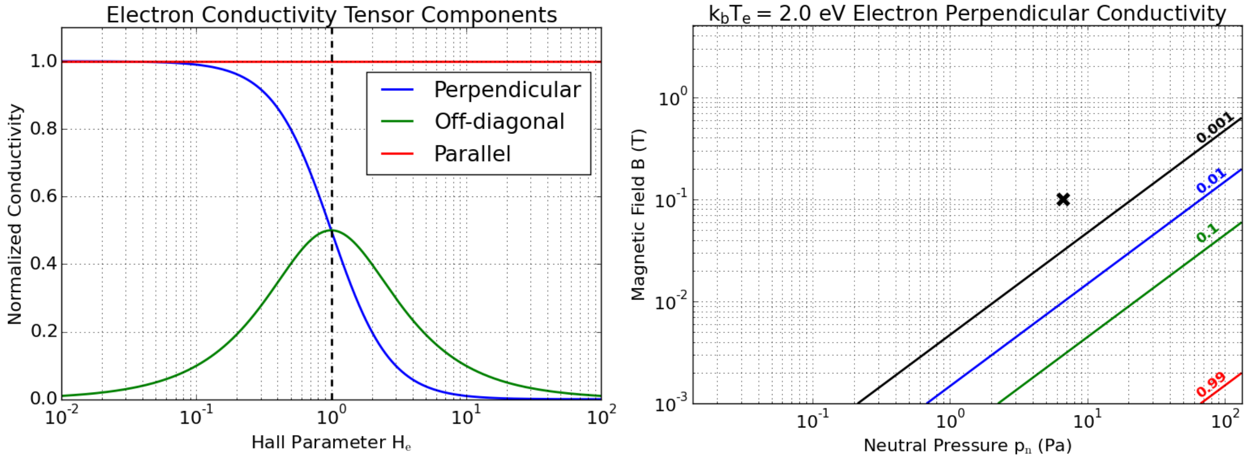

(a)

(b)

Figure 4.11: a) The components of the electron conductivity tensor given by Eq. (4.17) normalized by σ_o versus the electron Hall parameter H_e. b) Contours of the normalized perpendicular electron conductivity versus the neutral Argon pressure p_n and magnetic field strength B. The black cross marks the location of the neutral pressure p_n = 6.67 Pa and magnetic field B_z = -0.1 T used while recording the picture shown in Fig. (4.10). At this location in parameter space, the perpendicular conductivity has fallen by more than a factor of 10^3.

of constant (normalized) perpendicular conductivity are shown in Fig. (4.11b) versus the neutral Argon pressure and the magnetic field strength. The black cross on Fig. (4.11b) is the point in (p_n,B_z) space at which the test experiment shown in Fig. (4.10) was performed. At this point, the electron magnetization was so strong that the perpendicular conductivity fell by a factor of more than 10^3, and as a result, a plasma could no longer be generated between electrodes E2 and E1. When extrapolating this result to much higher magnetic fields (greater than 1 T) and lower neutral pressures (less than 6.67 Pa) as required by the $\mathbf{g} \times \mathbf{B}$ experiment, the perpendicular electron conductivity will drop by several more orders of magnitude.

These results were derived under the steady state (DC) assumption where $\frac{d}{dt} \to 0$. The same calculation can be done including the influence of the RF field on electrons. Here, we cite the results of this calculation from [128] where the conductivity tensor was replaced with the dielectric tensor by applying the relation $\boldsymbol{K} = \mathbf{I} - \boldsymbol{\sigma}/(i\epsilon_o\omega)$ where $\mathbf{I}$ is the identity matrix, ω is the RF driving frequency, and i is the imaginary unit. The dielectric tensor components are then given by

$$k_\perp = 1 - \frac{\omega - i\nu_{\mathrm{e,n}}}{\omega}\frac{\omega_{\mathrm{p,e}}^2}{(\omega - i\nu_{\mathrm{e,n}})^2 - \omega_{\mathrm{c,e}}^2}, \tag{4.21}$$

$$k_{\mathrm{H}} = \frac{\omega_{\mathrm{c,e}}}{\omega}\frac{\omega_{\mathrm{p,e}}^2}{(\omega - i\nu_{\mathrm{e,n}})^2 - \omega_{\mathrm{c,e}}^2}, \tag{4.22}$$

and

$$k_\parallel = 1 - \frac{\omega_{\mathrm{p,e}}^2}{\omega(\omega - i\nu_{\mathrm{e,n}})}. \tag{4.23}$$

It may be possible to exploit Eqs. (4.21 – 4.23) in such a way that the single grain dropper is able to generate a plasma perpendicular to the magnetic field when $\omega \sim \omega_{\mathrm{c,e}}$. Such methods might include, for example, Electron Cyclotron Resonance (ECR) [129, 130]. In the case of the single grain dropper immersed in a B = 1 T magnetic field generated by the MDPX device, the resonance excitation frequency of the source would need to be on the order of tens of GHz.

In addition to using the appropriate driving frequency, a potential drop must exist across the sheath between the plasma and the electrode to provide the electric field that suspends dust grains against the gravitational force. This potential drop can be of the order 10 – 100 volts in most dusty plasmas. [131] performed a self consistent analytic calculation for a capacitive sheath under the assumptions of inertialess electrons that respond instantaneously to the RF field and time independent, collisionless ion motion. Under these assumptions, it was shown that the self-bias voltage of the electrode was

$$V_{\mathrm{f,RF}} = \frac{k_{\mathrm{b}} T_{\mathrm{e}}}{e} \left(\frac{3}{4} \pi \psi + \frac{9}{32} \pi^2 \psi^2 \right) \tag{4.24}$$

where $\psi \sim \omega^{-2}$ is a frequency dependent voltage scaling parameter. Based on Eq. (4.24), it is unclear whether or not a high frequency plasma source will have a sufficiently large sheath voltage drop to suspend dust clouds. Some evidence for greatly reduced dust suspension and confinement was observed in [132, 133] where the frequency dependence of dust grain growth in Silane plasma processing experiments was analyzed. They observed that the grain growth rates were substantially reduced at higher frequencies. A possible explanation for this is the reduction of the sheath voltage drop at high frequencies, which may lead to reduced grain trapping and subsequent growth through coagulation.

Based on the results and scalings shown in this section, we conclude that the grain dropper cannot be used according to the geometry of Fig. (4.9) with a 13.56 MHz RF source to perform the $\mathbf{g} \times \mathbf{B}$ drift experiment. No further engineering was performed on the single grain dropping device. In the next section, we will discuss an alternative method to collimate falling dust grains rather than drop single grains one-by-one.

4.2 Measuring the g x B drift using CoPlA and MDPX

In Sec. (4.1.4), we performed a test experiment to examine the performance of the single grain dropper in a strong magnetic field and found that the device is no longer able to produce a plasma perpendicular to the magnetic field. This was due to strong electron magnetization leading to a drastically decreased perpendicular electron conductivity which substantially modified the single drain dropper sheath electric field geometry. Because the plasma was no longer generated perpendicular to the magnetic field, the plasma sheath confinement force was no longer able to suspend dust grains. As a result, we were unable to use the single grain dropping device to perform the $\mathbf{g} \times \mathbf{B}$ drift experiment in MDPX.

4.2.1 An alternative dust grain collimation method

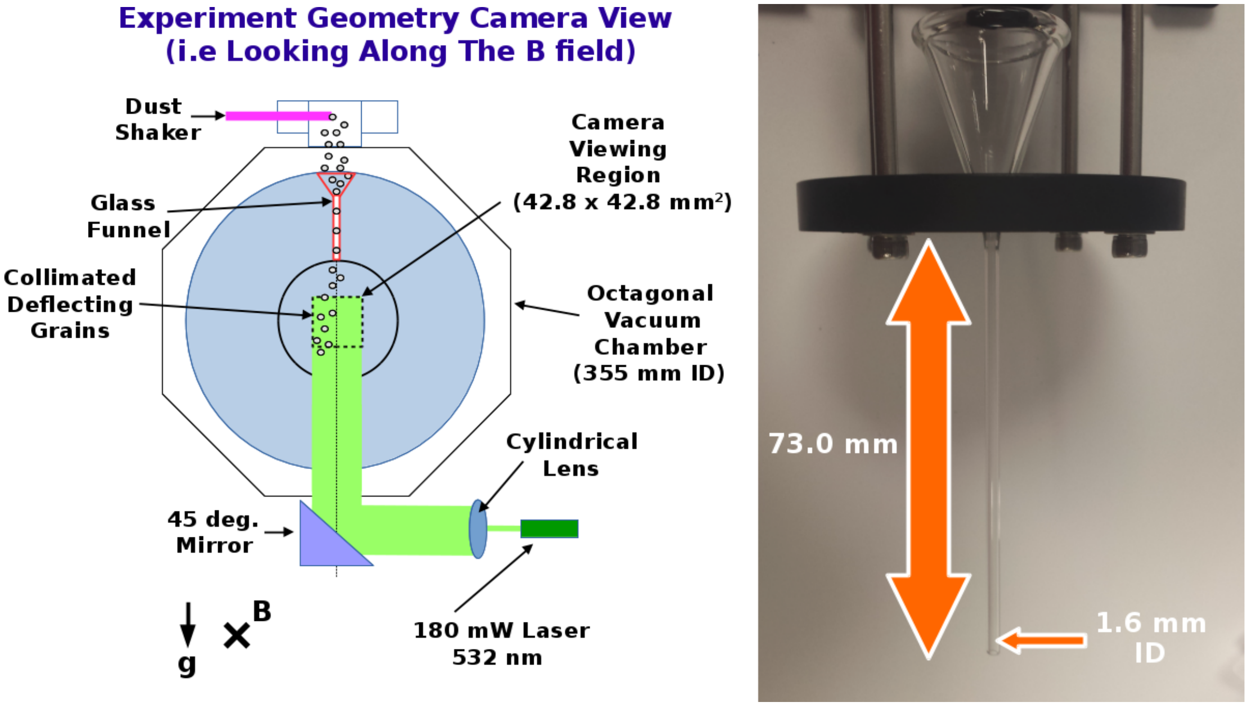

(a) (b)

Figure 4.12: a) A top-down schematic view of the glass funnel mounted inside the MDPX plasma chamber. Dust grains were inserted into the plasma using a standard dust shaker located above the funnel. The falling dust grains were collimated by the funnel and exit the funnel approximately 50 mm above the camera field of view. b) The glass funnel used to collimate falling dust grains. A detailed dimensional drawing of the funnel is provided in the Appendix in Fig. (A.3).

As an alternative to using the single grain dropper, a glass funnel was placed below a standard dust shaker to collimate the falling dust grains into the central region of the vacuum chamber before entering the camera field of view. The geometry of this configuration is shown in Fig. (4.12). The funnel stem is 73 mm long with an ID of 1.6 mm. The flared upper surface ID is 31.8 mm. The dust grains are inserted into the MDPX chamber using a dust shaker placed several centimeters above the flared surface of the glass funnel. The electrode spacing between the RF electrode and the transparent grounded electrode was 110 mm. A side view of the geometry is shown in Fig. (3.5). The funnel outlet was placed in the axial mid-plane of the chamber such that it was approximately 54 mm away from both electrodes so that the falling dust grains travel through the plasma bulk. The bottom outlet of the glass funnel was placed approximately 70 mm above the radial geometric center of the MDPX plasma chamber. The collimated dust grains travel a vertical distance of approximately 50 mm before entering the camera field of view. An investigation into the effect of using a glass funnel to collimate the falling dust grains is performed in Sec. (4.3).

4.2.2 Measurement procedure and data processing technique

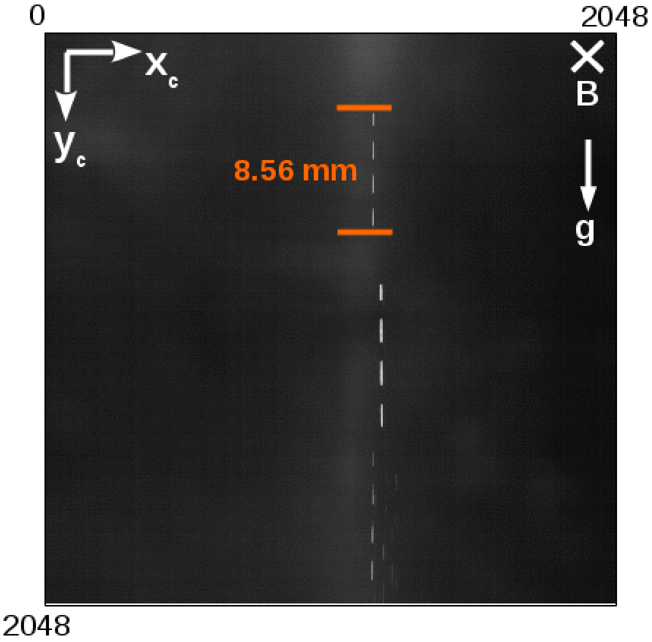

Figure 4.13: Parameters: $a_{\mathrm{d}} = 0.25$ μm and $p_{\mathrm{n}} = 0.67$ Pa. Example data of collimated falling grains. Each falling grain is seen as a sequence of four white streaks in this single frame because the laser was modulated at 3 ms with a 50% duty cycle and the camera exposure time was 10 ms. The camera was not synchronized with the laser modulation. In this example, the laser is already "on" when the camera exposure begins so that there are two complete light streaks in the middle and two partial light streaks at the ends. The 8.56 mm streak length shown is approximately consistent with the terminal speed approximation that will be used in Sec. (4.2.3). Some streaks may be slightly longer than predicted by the terminal speed approximation which can be attributed to a reduction in neutral drag as discussed at the end of Sec. (4.3.2).

The collimated dust grains were illuminated using a 180 mW 532 nm laser that was spread into an approximately 4 mm thick by 30 mm wide laser sheet using a cylindrical lens as shown in Fig. (4.12). The laser was modulated at 3 ms with a 50% duty cycle during a 10 ms camera exposure time. The laser and camera were not synchronized. The grains were imaged using the camera system discussed in Sec. (3.2.3) with a spatial resolution of (20.9 ± 0.4) μm/pixel.

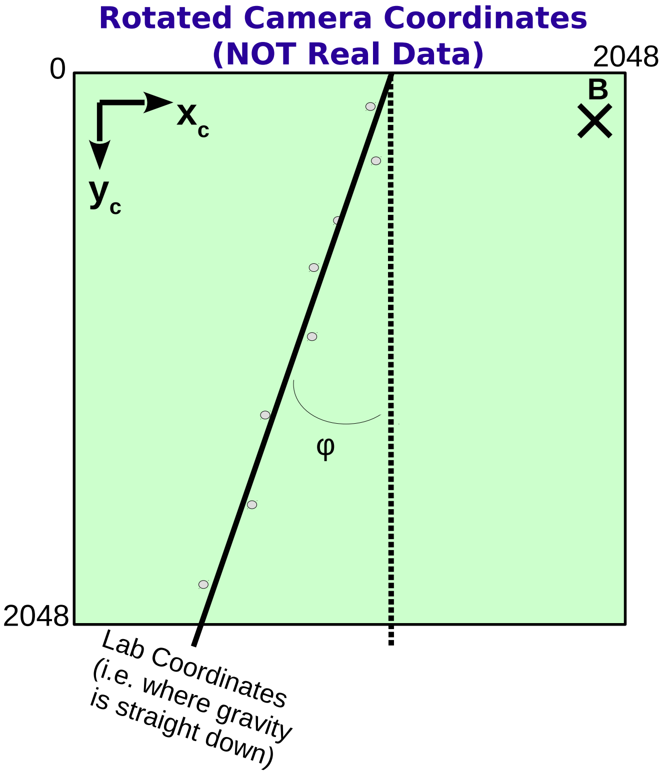

Figure 4.14: An illustration depicting possible vertical mis-alignment of the camera system. In order to find the direction of gravity, dust particles are dropped into the system when the RF signal is turned off and there is no plasma. The camera coordinates are denoted with a subscript "c" and are tilted relative to the lab coordinates. Gravity is straight down in the lab coordinate system.

The presence of a magnetic field puts a tremendous amount of stress on the camera components and the camera mounting hardware. This stress could cause slight spatial shifts in the camera equipment which may change the direction of gravity with respect to the camera reference frame. The camera shift and tilt is illustrated by the cartoon in Fig. (4.14).

Camera coordinates are given the subscript "c" and by convention, the origin of the camera coordinate system is located in the upper left hand corner of the image.

The direction of gravity was re-calibrated at each magnetic field setting by inserting dust grains into the vacuum chamber when no plasma was present. In the absence of plasma, the dust grains were assumed to be uncharged such that they fall in the direction of the gravitational field — thus providing a calibration to account for the magnetic forces causing the camera equipment to shift. The following data recording procedure was applied at each magnetic field strength:

Data Recording Steps

S.1 Set the desired magnetic field strength.

S.2 Turn off the RF system so the grains fall through neutral gas only.

S.3 Record the falling grains to determine the direction of gravity.

S.4 Turn on the RF system so the grains fall through the plasma bulk.

S.5 Record the falling grains to determine the amount of $\mathbf{g} \times \mathbf{B}$ deflection.

S.6 Return to S.1.

Approximately 3 – 5 thousand dust grains were dropped vertically downward at each magnetic field setting. The average locations of a grain in each light streak (example streaks are shown in Fig. (4.13)) was calculated using the CoPlA analysis software discussed in Sec. (3.1.2). The top 200 pixels were removed from the image due to a laser reflection. The distribution of average dust grain locations were processed into a 2D histogram with 10 vertical bins and 20 horizontal bins. The vertical bin width was $\Delta y_{\mathrm{c}} = 3.86$ mm and the horizontal bin width was $\Delta x_{\mathrm{c}} = 0.287$ mm. Two example position histograms (in camera coordinates) are shown in Fig. (4.15). Each horizontal row of the histogram data shown in Fig. (4.15) was curve fit to a Gaussian distribution with a constant background offset. The

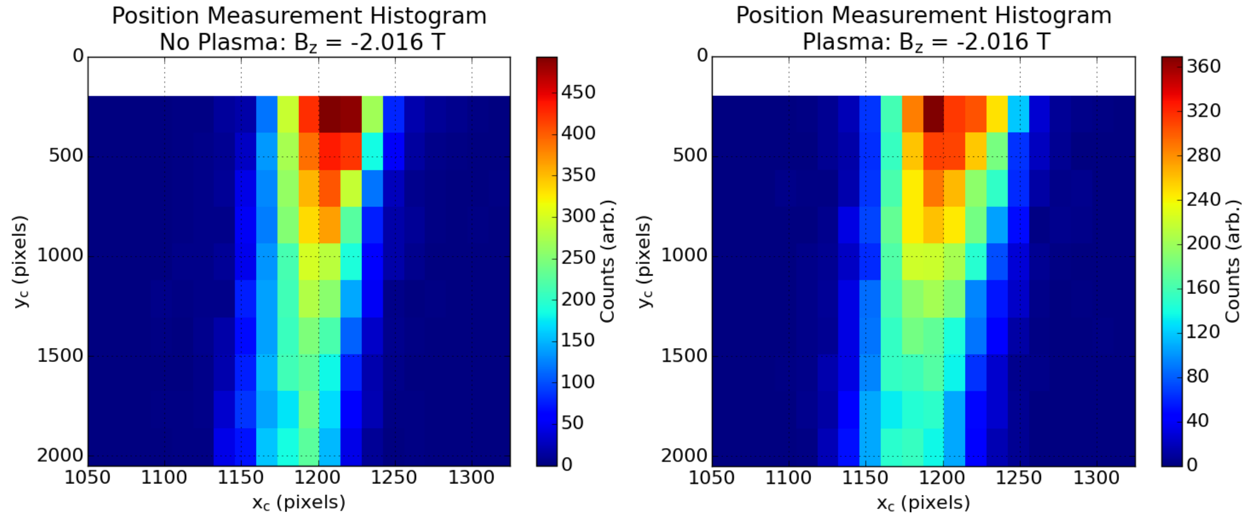

(a) (b)

Figure 4.15: An $(x_{\rm c}, y_{\rm c})$ falling dust grain streak center of intensity histogram in camera coordinates. The top 200 pixels are cropped from the data due to a laser reflection. a) The plasma is turned off and 13,687 dust grain streaks were measured. b) The plasma is turned on and 12,032 dust grain streaks were measured. In both cases there are on average more counts in the top-most bins because as the dust grains fall they may shift out of the image plane thus making their detection more difficult.

mean of the curve fit was then used as the effective horizontal dust grain location in each row of the histogram data. Examples of both the histogram row data and the corresponding Gaussian curve fits are provided in Fig. (4.16).

As previously discussed, it was necessary to calibrate the camera shift at each magnetic field strength due to magnetic fields shifting the equipment locations. This calibration was performed by applying a linear fit through the average particle locations (from the histogram and the Gaussian curve fits) when no plasma was present. This is illustrated in Fig. (4.17a). The linear fit equation was

$$x_{\rm c} = m_{\rm slope} y_{\rm c} + b_{\rm o} \tag{4.25}$$

where contrary to popular convention, $x_{\rm c}$ was treated as the dependent variable of the fit, $m_{\rm slope}$ is the slope, $y_{\rm c}$ was treated as the independent variable in the fit, and $b_{\rm o}$ is the x-intercept. An illustration of the linear fit compared to the data when the plasma was turned on is provided in Fig. (4.17). The slope from Eq. (4.25) was used to find the direction of

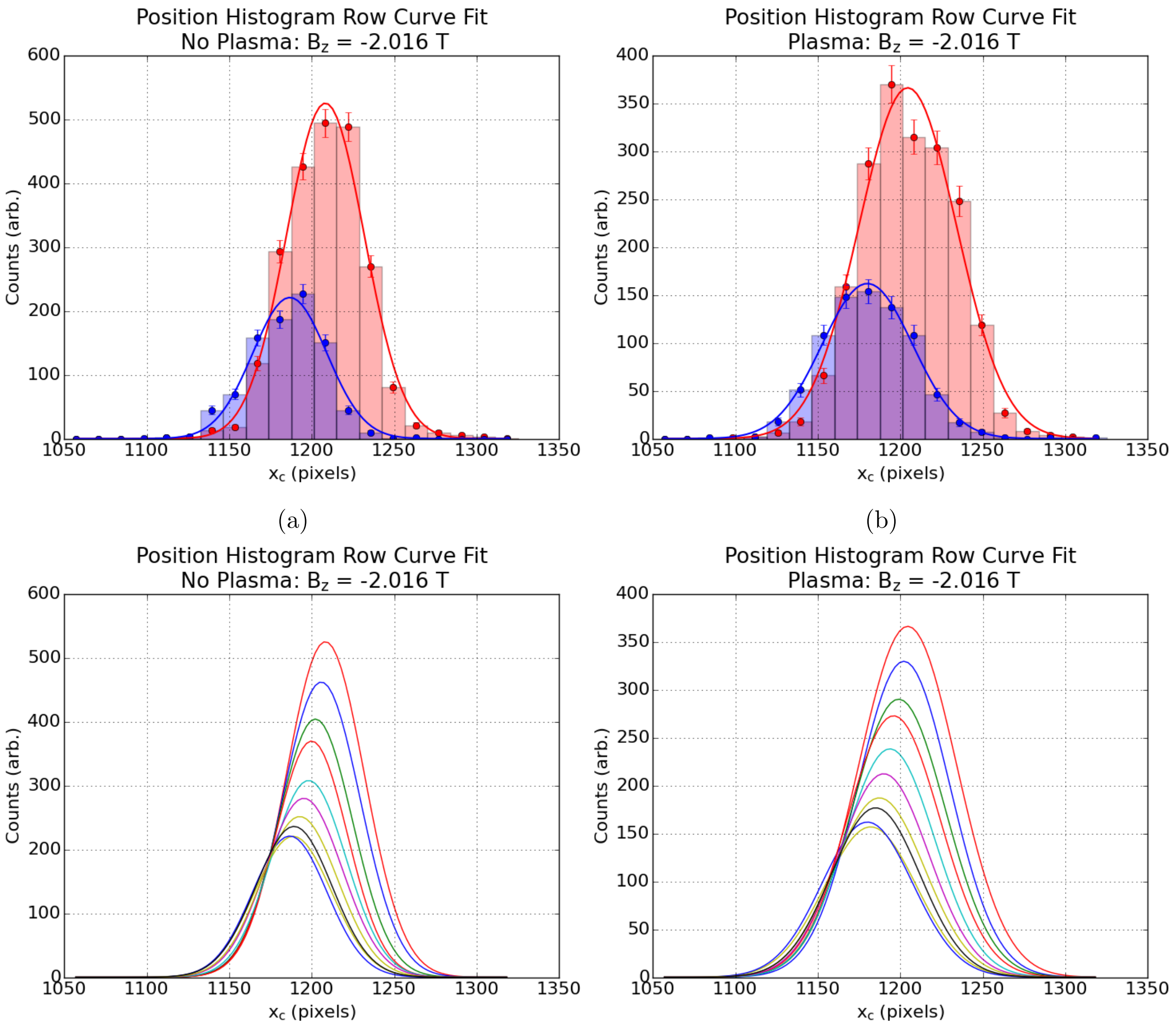

(a) (b)

(c) (d)

Figure 4.16: a), b) The top and bottom rows of the raw histogram data shown in Fig. (4.15). The solid lines are the corresponding curve fits. c), d) The Gaussian curve fits for each row of Fig. (4.15).

the gravitational field within the camera coordinate system. The rotation angle was given by $\varphi = \arctan(m_{\text{slope}})$. The locations of the histogram means were shifted by the linear fit x-intercept b_o and then rotated into the laboratory coordinate system according to the

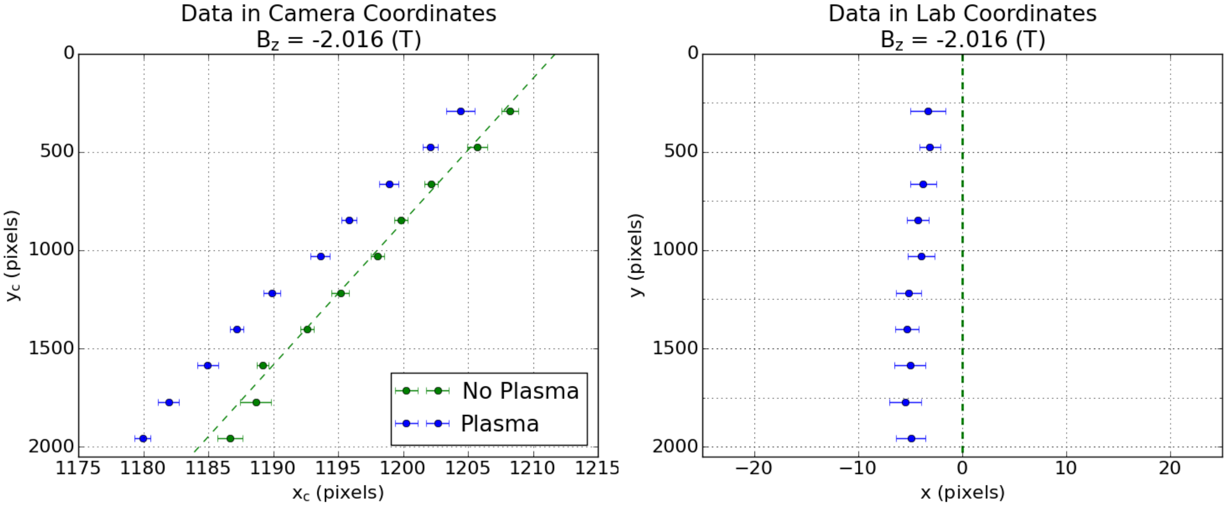

(a) (b)

Figure 4.17: A summary of the deflection data and the resulting rotation from the camera calibration at a magnetic field strength of B_z = -2.016 T (directed into the page). a) The blue dots with error bars are from the data obtained while the plasma was turned on whereas the green dots with error bars are from the data obtained when the plasma was turned off. A straight line is fit through the no plasma data (dashed green line). The intercept and slope of the no plasma linear fit were then used to rotate the plasma data (blue dots) into Lab coordinates where gravity is along the y-axis. b) The plasma data (blue dots) expressed in Lab coordinates where the gravitational field vector is straight down along the y-axis. The dashed green line is the rotated linear fit from part a).

following transformation

$$\begin{pmatrix} x \\ y \end{pmatrix} = \begin{pmatrix} \cos(\varphi) & -\sin(\varphi) \\ \sin(\varphi) & \cos(\varphi) \end{pmatrix} \begin{pmatrix} x_c \\ y_c \end{pmatrix}. \tag{4.26}$$

The new coordinates (x, y) have no subscript and from here onward are the lab coordinates where the gravitational field is along the y-axis. The error was propagated using standard Gaussian error propagation.

Grain charge calculation method

The data shown in Fig. (4.17b) was scaled into laboratory coordinates using the 20.9 μm/pixel spatial calibration factor discussed in Sec. (3.2.3). The geometric center of the plasma chamber is at the origin of the (x, y) coordinate system. The dust grains exit the funnel outlet at $(x_\mathrm{o}, y_\mathrm{o})$ = (0,70) mm. The dust grain charge was calculated by solving the equations of motion, Eqs. (2.18 – 2.19), while performing an iterative minimization to find the dust grain charge Z_d which best describes the measured data. The minimization function is given by

$$\chi^2 = \sum_{\mathrm{i}=1}^{N_\mathrm{y}} \left[\frac{x_\mathrm{i} - \tilde{x}_\mathrm{i}(y_\mathrm{i}; Z_\mathrm{d})}{\sigma_\mathrm{i}} \right]^2 \tag{4.27}$$

where N_y = 10 is the number of vertical histogram bins, x_i is the horizontal position of rotated deflection data from when the plasma is turned on, σ_i is the standard deviation of the x_i measurements, and $\tilde{x}_\mathrm{i}(y_\mathrm{i}; Z_\mathrm{d})$ is obtained from the solution of the equations of motion, Eqs. (2.18 – 2.19).

4.2.3 Summary of measurement results

The initial conditions for solving Eqs. (2.18 – 2.19) were $(x_\mathrm{o}, y_\mathrm{o}) = (0, 70)$ mm, $v_\mathrm{o,x} = 0$ cm/s, and the initial y-velocity is examined for the two limiting cases $v_\mathrm{o,y}$ = 0 cm/s and $v_\mathrm{o,y}$ = -80 cm/s (approximately terminal speed). These initial y-velocities are the lower and upper limiting cases of the dust grain speed exiting the collimating funnel. The upper limit of $v_\mathrm{o,y}$ = -80 cm/s is justified by the results shown in Fig. (2.5b). The lower limiting case $v_\mathrm{o,y}$ = 0 cm/s was included to show that the results do not have a strong dependency on $v_\mathrm{o,y}$ due to the relatively small amount of horizontal deflection. Fig. (4.20) provides a summary of the best fit dust grain charge in both the $v_\mathrm{o,y}$ limiting cases. The curve fit ODE solutions to the data for all magnetic field settings are summarized in Figs. (4.18 – 4.19). The equations of motion were integrated using the 4th order Runge-Kutta technique [68].

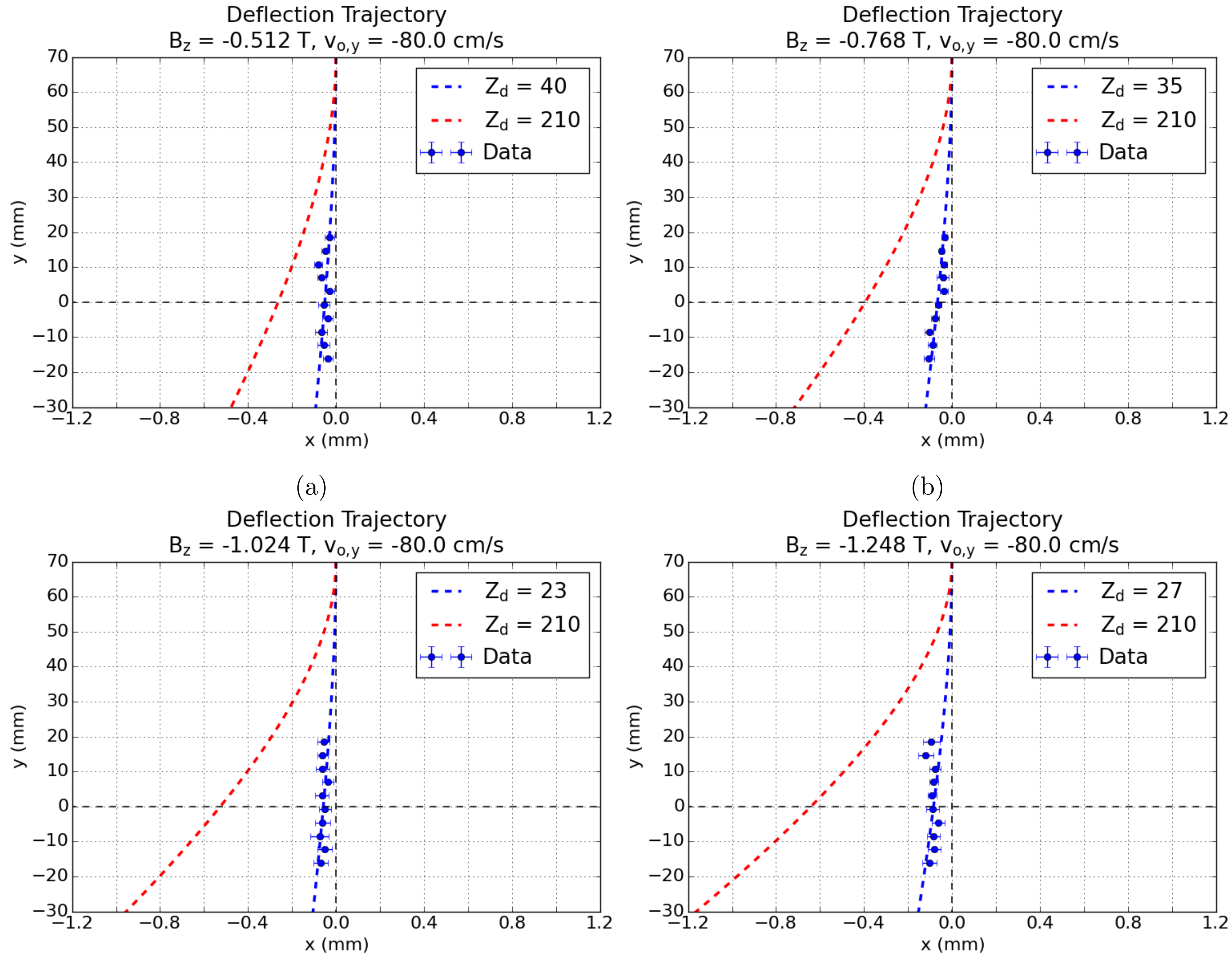

(a) (b)

(c) (d)

Figure 4.18: A summary of the deflection data (blue dots with error bars), the curve fit (dashed blue) used to obtain the dust grain charge Z_d, and the expected dust trajectory (dashed red) assuming 25% of the OML charge $Z_\mathrm{d} = 210$. The initial x-velocity was $v_{\mathrm{o,x}} = 0$ and initial y-velocity was terminal speed $v_{\mathrm{o,y}} = -80$ cm/s. The magnetic field is directed into the page. a) B_z = -0.512 T, b) B_z = -0.768 T, c) B_z = -1.024 T, d) B_z = -1.248 T.

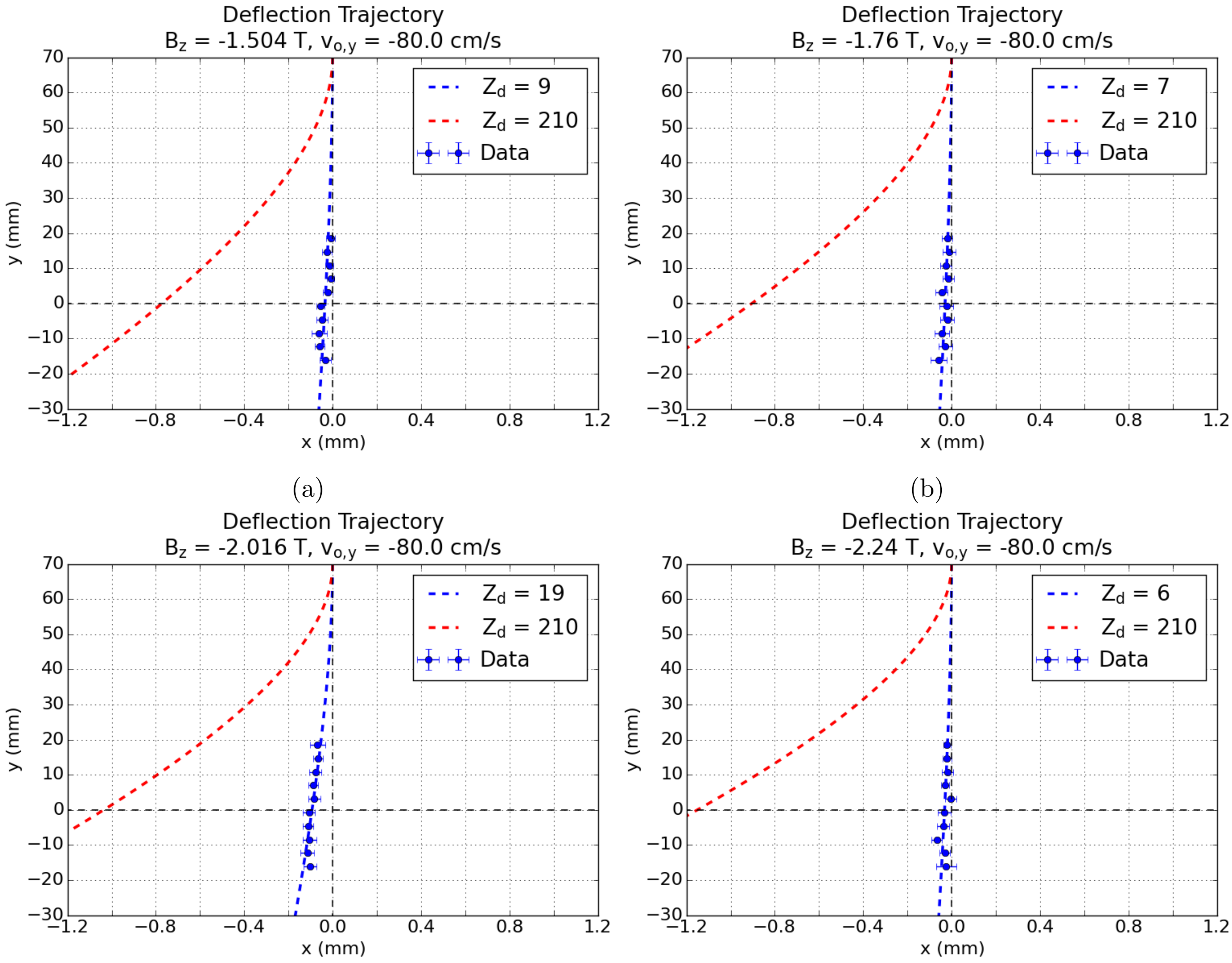

(a)

(b)

(c)

(d)

Figure 4.19: A summary of the deflection data (blue dots with error bars), the curve fit (dashed blue) used to obtain the dust grain charge Z_d, and the expected dust trajectory (dashed red) assuming 25% of the OML charge $Z_\mathrm{d} = 210$. The initial x-velocity was $v_{\mathrm{o,x}} = 0$ and initial y-velocity was terminal speed $v_{\mathrm{o,y}} = -80$ cm/s. The magnetic field is directed into the page. a) B_z = -1.504 T, b) B_z = -1.760 T, c) B_z = -2.016 T, d) B_z = -2.240 T.

- Experiment parameter summary:
  - Dust grain parameters
    - Silica
    - Mass density $\rho_{\rm d} = 2.2$ g/cm^3
    - Radius $a_{\rm d} = 0.25$ μm
  - RF parameters
    - Frequency $f_{\rm RF} = 13.56$ MHz
    - Power $P_{\rm RF} \approx 2$ W
  - Neutral gas parameters
    - Argon
    - Pressure $p_{\rm n} = 0.67$ Pa = 5 mTorr

Table 4.1: A summary of the graphical results shown in Fig. (4.20) including the peak to peak voltage of the RF signal applied to the bottom electrode. There is no clear pattern between the RF voltage and the charge measurement.

Magnetic Field Strength B (T)	0.512	0.768	1.024	1.248	1.504	1.760	2.016	2.240
Dust Charge $Z_{\rm d}$	41	35	23	28	9	7	19	6
RF Voltage V_A (V)	116	111	149	147	149	133	144	180

Table 4.2: A summary of the rotation angle $\varphi = \arctan(m_{\rm slope})$ used to find the direction of gravity in the camera coordinate system. There is no clear pattern between the correction angle and the magnetic field strength.

Magnetic Field Strength B (T)	0.512	0.768	1.024	1.248	1.504	1.760	2.016	2.240
Correction Angle φ (deg)	0.871	0.710	0.844	0.792	0.829	0.752	0.786	0.889

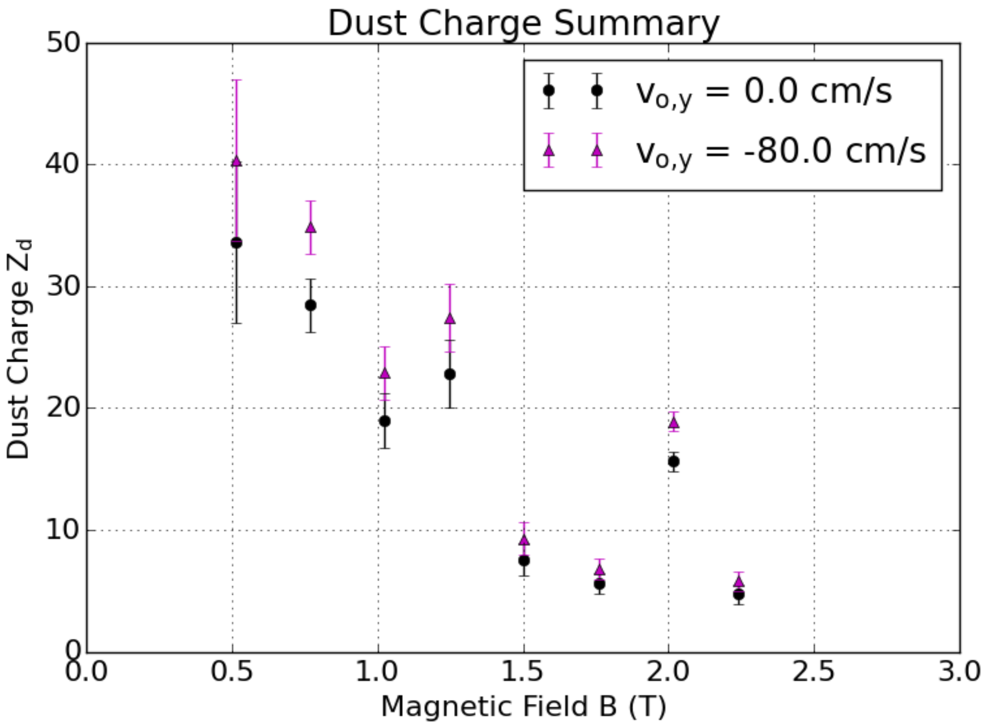

Figure 4.20: A summary of the dust charge obtained from each case shown in Figs. (4.18 – 4.19). The number of electrons residing on the dust grain, Z_{d}, versus magnetic field strength for the limiting cases of $v_{\mathrm{o,y}} = 0.0$ (black dots) and $v_{\mathrm{o,y}} = -80$ cm/s (purple dots).

4.3 Discussion

The relatively small amount of horizontal deflection shown in Figs. (4.18 – 4.19) indicates a much lower dust grain charge than predicted by the OML theory. The dust grain charge Z_{d} at all magnetic field strengths is summarized in Fig. (4.20). At the lowest magnetic field strength of B_{z} = -0.512 T, the dust grain charge was calculated to be $Z_{\mathrm{d}} \approx 50$, which is only about 6% of the OML predicted value $Z_{\mathrm{d,OML}} = 840$. Tables (4.1 – 4.2) summarize the RF peak-to-peak voltage and the correction angle used to find the direction of gravity in the camera coordinate system and show that there is no pattern between them and the dust grain charge measurements.

The dust grain charge measurements were significantly less than predicted by the OML charging theory. This experimental result may provide insight into a new understanding of dust grain charging in strong magnetic fields. Modifications to the dust grain charging dynamics are likely tied to the onset of strong electron magnetization. In the experiments performed here, the electron Larmor radius is comparable to the grain size which could modify the collection efficiency of electrons by the dust grain. However, before diving into a discussion of modifications to grain charging dynamics in magnetic fields, it is important to address some additional effects that could have influenced the measurement. The following questions are addressed:

- Does the net deflection obtained from the collimation averaging technique closely correspond to a trajectory that a single dust grain would otherwise follow?
- Although the dust grains are falling through the plasma bulk where quasi-neutrality should apply, what effect could a radial electric field have? Are there any other forces present?
- When several thousand dust grains are falling vertically downward, the bulk dust grain motion may "knock" a substantial fraction of the neutral gas particles out of the collimation region. This depletion of neutral gas could reduce the neutral drag on the dust grains trailing behind the bulk motion. How would a reduced neutral gas drag in the y-direction affect our measurements?
- What are some possible mechanisms leading to dust grain charge reduction when the electrons are so strongly magnetized that their Larmor orbit size becomes comparable to the dust grain dimension?

4.3.1 Simulations of collimated falling dust grains

The glass funnel collimation technique could, in cases where a grain collides with the funnel wall immediately before exiting, cause a non-zero initial x-velocity in the $\pm\hat{\mathbf{x}}$ direction. If the initial x-velocity $v_{\mathrm{o,x}}$ was in the same direction as the dust grain $\mathbf{g} \times \mathbf{B}$ drift motion, then the amount of drift could be greatly exaggerated. This effect would result in an artificially large calculated grain charge. On the other hand, if the initial x-velocity $v_{\mathrm{o,x}}$ were opposite the dust grain $\mathbf{g} \times \mathbf{B}$ drift direction, then the calculated grain charge may be artificially small. The role of non-zero initial x-velocities is discussed in this section by simulating several different sets of initial conditions.

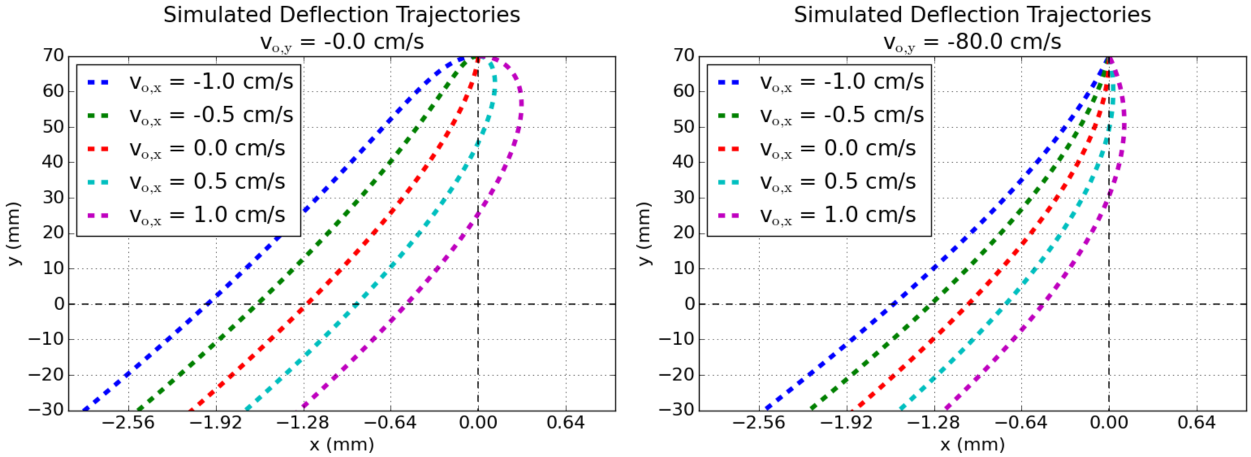

(a)　　　　　　　　　　(b)

Figure 4.21: Parameters: B_{z} = -0.5 T, a_{d} = 0.25 μm, $Z_{\mathrm{d,OML}}$ = 840, and p_{n} = 0.67 Pa. Five cases are plotted for initial x-velocities on the interval (-1,1) cm/s. The dust grains are assumed to fall independently with no inter-dust interactions. a) Possible trajectories for the case where the grains exiting the funnel are starting with $v_{\mathrm{o,y}} = 0$. b) Possible trajectories for the case where the grains exiting the funnel are starting with initial y-velocity of $v_{\mathrm{o,y}} =$ -80 cm/s at approximately terminal speed.

To start, the dust grain motion is simulated for several possible values of the initial x-velocity on the interval $v_{\mathrm{o,x}} = (-1, 1)$ cm/s while assuming the dust grains originate at the initial position $(x_{\mathrm{o}}, y_{\mathrm{o}}) = (0, 70)$ mm. The initial y-velocity is assigned the limiting cases $v_{\mathrm{o,y}} = 0$ cm/s and $v_{\mathrm{o,y}} = -80$ cm/s. The results are summarized in Fig. (4.21) and show that regardless of the initial y-velocity, when the grains have a large initial x-velocity $v_{\mathrm{o,x}} = 1$ cm/s opposite the $\mathbf{g} \times \mathbf{B}$ drift motion, the grains quickly turn around and begin deflecting in the expected $-\hat{\mathbf{x}}$ direction.

The analysis above does not include the possibility that several thousand dust grains are exiting the funnel outlet at x-positions anywhere within the 1.6 mm ID of the funnel outlet. In order to address this issue, we apply a Monte-Carlo technique to randomly assign

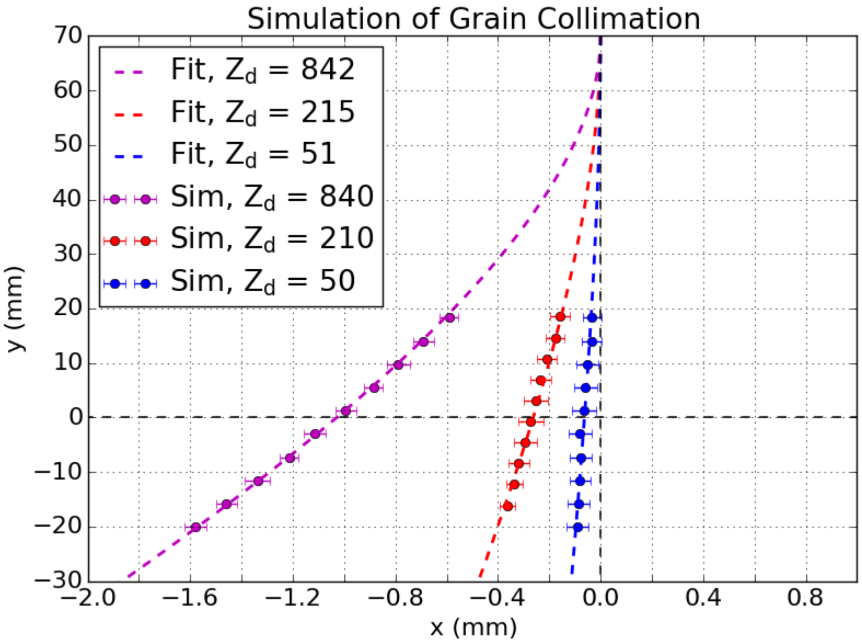

Figure 4.22: Parameters: B_{z} = -0.5 T (into the page), a_{d} = 0.25 μm, $v_{\mathrm{o,y}}$ = -80 cm/s, and p_{n} = 0.67 Pa. Possible dust grain deflection trajectories obtained from the Monte-Carlo analysis. Three cases are plotted for different assumed dust grain charges of $Z_{\mathrm{d}} = (840, 210, 50)$. The points with error bars are the Monte-Carlo simulation trajectories of several thousand particles. The dashed colored lines are the best fit ODE solutions obtained by applying the curve fit according to Eq. (4.27).

the initial conditions of the falling dust grains. The initial x-position x_{o} was randomly sampled from a uniform distribution on the interval (-0.8,0.8) mm and the initial x-velocity was randomly sampled from a uniform distribution on the interval (-1,1) cm/s. The initial y and $v_{\mathrm{o,y}}$ values are the same as the previous analysis. The equations of motion were integrated for these randomly assigned sets of initial conditions. The simulation data was processed according to the same procedure discussed in Sec. (4.2.2). The simulation and analysis procedure were repeated for several values of the dust grain charge. The results are summarized in Fig. (4.22) and show that even when a substantial fraction of the dust grains, on average, have a non-zero initial x-velocity and x-position, their net deflection will represent a trajectory very similar to that of a single grain with an equivalent average charge. The difference between the input charge used in the simulation versus the charge obtained using the data analysis technique of Sec. (4.2.2) differs by, at most, approximately

2%. Therefore, the grain collimation technique and histogram averaging procedure is a valid method to obtain the average deflection of many falling grains — thus providing a measure of an average grain charge that closely corresponds with that of a single grain.

4.3.2 Modifications to the $\mathbf{g} \times \mathbf{B}$ drift model

Radial electric fields

In the model developed in Sec. (2.2), quasi-neutrality was assumed in the plasma bulk where $n_\mathrm{e} \approx n_\mathrm{i}$ and thus $\mathbf{E} \approx 0$ far from the chamber walls, electrodes, and their corresponding space charge sheaths. In the experiment performed in Sec. (4.2.3), the falling dust grains were approximately 54 mm from both the driven RF electrode and the grounded electrode along the axial direction. The camera observation region was approximately 4 x 4 cm^2 and was centered on the geometric center of the chamber so that the grains were approximately 150 mm away from the chamber walls along the radial direction. Since the falling grains were a substantial distance from both the axial space charge sheaths near the electrodes and the radial space charge sheaths near the chamber walls, it is unlikely that sheath electric fields are influencing the dust grain motion. However, due to the presence of the strong magnetic field, it may be possible that the sheath electric fields were able to penetrate deeper into the plasma bulk and influencing the falling dust grain motion directly through the electrostatic force. In this section, the influence of both the radial plasma sheath electric fields as well as ambipolar electric fields on falling grain $\mathbf{g} \times \mathbf{B}$ drift motion is considered.

For an assumed 15 mm thick space charge sheath near each electrode, the grains were approximately 40 mm away from the electrode sheath boundaries. Although this distance is quite large, some possible upper limits on the radial electric field strength can be estimated from previous sheath measurements. [50] observed rotating dust crystals in a plasma sheath at a neutral pressure of $p_\mathrm{n} = 50$ Pa and magnetic field strength of B = 0.014 T. They found that the radial component of the sheath electric field was well approximated by $E_r(r) = 0.3r[cm]$ V/cm where r is the radial distance in cm. Using this expression with $r = 7$ cm, the radial electric field in the MDPX device for the **g** x **B** drift experiment was 2.1 V/cm. This value is also in agreement with a DC glow discharge experiment done by [134] where it was shown that the electric field strength was approximately 2.4 V/cm over the neutral pressure range (10 – 100) Pa. Furthermore, when analyzing the radial confinement of the center of mass of a six particle dust cluster, it has also been shown that the radial electric field does not have a strong dependence on the RF power [135]. Therefore, even though the **g** × **B** experiments were performed at a lower neutral gas pressure and with possibly different RF discharge conditions, the work of [50, 134, 135] provide a useful estimation of an upper limit on possible radial electric field values.

While keeping in mind that the radial electric field strengths above are likely an overestimate of the actual electric fields in the plasma bulk, the **g** x **B** model of Sec. (2.2) is modified to include a linear radial electric field of the form

$$\mathbf{E}_{\mathrm{r}}(r) = E_{\mathrm{o}}\frac{r[cm]}{7}\hat{\mathbf{r}} \tag{4.28}$$

where $E_{\mathrm{o}} > 0$ is a positive constant and r is the radial distance in cm. The analysis is restricted to a radially outward electric field such that the electric force $\mathbf{F}_{\mathrm{E}} = q_{\mathrm{d}}\mathbf{E} = -eZ_{\mathrm{d}}\mathbf{E}$ experienced by the dust grain is radially inward. If the force were radially outward, the grain would be pushed away from the origin, which would increase the amount of deflection. Furthermore, the work of [136, 137, 138] showed that for the case of unmagnetized ions (at least to the extent that their Larmor radius is much larger than the scale of interest) and magnetized electrons in a finite cylindrical geometry, the plasma potential will peak at r = 0 and slowly decay in the radial direction such that a radially outward electric field is present. The equations of motion were numerically integrated for several possible values of E_{o} at B_{z} = -0.512 T and B_{z} = -2.016 T. The dust grain charge was assumed to be $Z_{\mathrm{d}} = 210$ (0.25% of the OML value). Fig. (4.23) summarizes the results and shows for a magnetic field strength of B_{z} = -0.512 T, a radial electric field strength of E_{o} = 2.5 V/cm is required to approximately bring the dust grain trajectory in line with the deflection measurements. At B_z = -2.016 T, E_o = 2.5 V/cm is insufficient to align the simulation results with the measured data. $E_\mathrm{o} \approx 2.5$ V/cm is most likely substantially larger than typical values in the plasma bulk. In order to verify that the electric field has likely been over-estimated, a radial double Langmuir probe scan taken in the plasma bulk of the MDPX device at p_n = 1.33 Pa with an RF power of 2 Watts and zero magnetic field is shown in Fig. (4.24). The maximum electric field strength obtained from a cubic spline fit of the space potential profile was $E_\mathrm{o} \approx 0.25$ V/cm.

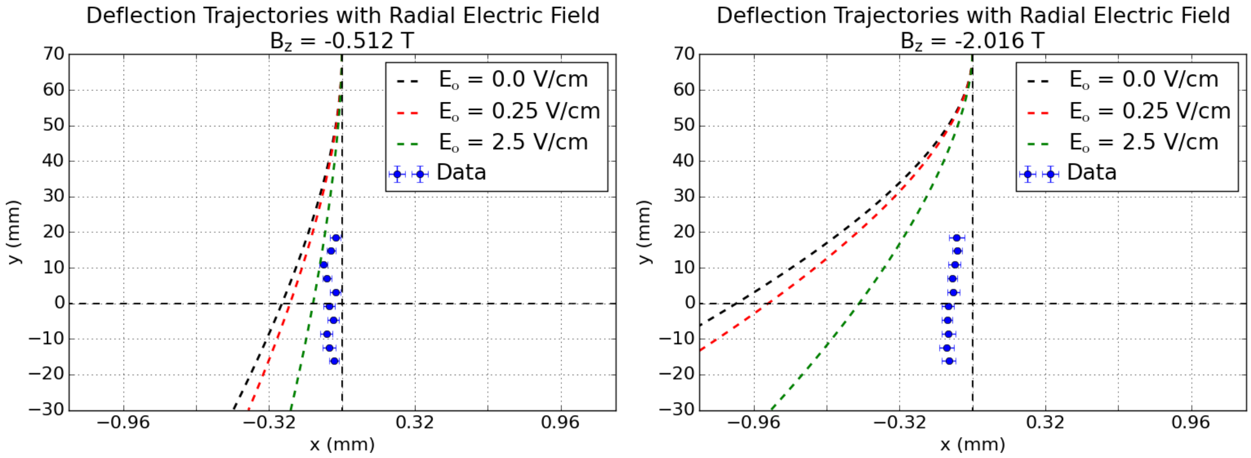

(a) (b)

Figure 4.23: Parameters: a_d = 0.25 μm, Z_d = 210, and $v_\mathrm{o,y}$ = -80 cm/s. Single grain trajectories according to a radially outward electric field given by Eq. (4.28). The blue data points are the measurement data from Sec. (4.2.3) and were plotted for reference. a) $B_\mathrm{z} = -0.512$ T. b) $B_\mathrm{z} = -2.016$ T.

The radially outward electric field and corresponding central peak in the plasma potential is largely due to the so called "Simon short-circuit" effect [139] where ions are driven radially outward and accelerated up to the Bohm speed to maintain flux balance. In the Simon short-circuit model, there is a radially outward flow of ions from the central region of the plasma to maintain flux balance. This radially outward flow of ions would exert a radially outward drag force on the dust grains, which would oppose the inward electrostatic force. However, theory has shown that for small dust grains such as the a_d = 0.25 μm

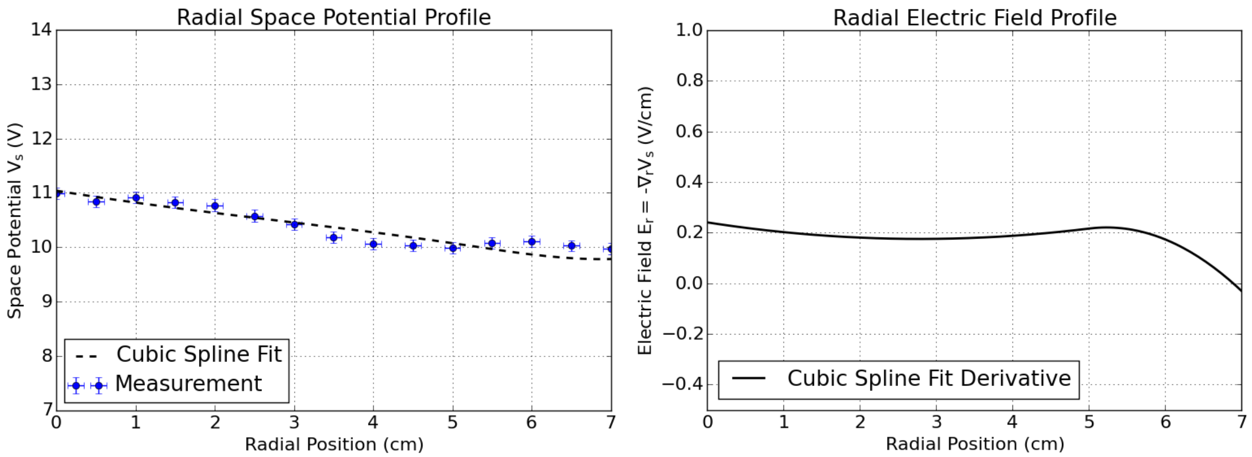

(a)

(b)

Figure 4.24: Parameters: $p_\mathrm{n} = 1.33$ Pa, and $P_{RF} = 2$ W ($\sim$ 110 V peak-to-peak voltage). A radial scan using a double-tip Langmuir probe. a) Radial profile of the space potential (blue points) provided by S. LeBlanc of the Plasma Sciences Laboratory at Auburn University. The dashed black line is the corresponding cubic spline fit to the space potential data. The radial position was assumed to have 10% error. b) The radial electric field profile (solid black line) obtained from the first derivative of the cubic spline fit in part a).

dust grains used in the $\mathbf{g} \times \mathbf{B}$ drift experiment, the direct electric force will exceed the ion drag [63, 60, 140, 141]. As a result, a radial ion drag force is unlikely to play a significant role in the measurements. Although it is unlikely that radially outward ion flows have a strong influence on our results, it is important to note that the Simon short-circuit model is not fully applicable because even at the minimum B_z = -0.5 T magnetic field, the ions are already strongly magnetized with Larmor radii on the order of millimeters. Due to ion magnetization, it could be possible that there are more localized electric fields existing on length scales of the order of tens of ion Larmor radii. However, at the present time, there is no comprehensive model that includes strongly magnetized ions. Despite the unknown role of ion magnetization, if we crudely assume that ions are born at rest and accelerated to the Bohm speed at the outer radial regions of the device, energy balance gives

$$E_\mathrm{amb} \approx \frac{k_\mathrm{b} T_\mathrm{e}}{2 e r_\mathrm{max}} \tag{4.29}$$

where $r_{\mathrm{max}} = 15$ cm in MDPX device. For $k_{\mathrm{b}}T_{\mathrm{e}} = 2$ eV electrons, Eq. (4.29) gives $E_{\mathrm{amb}} \approx 0.06$ V/cm, which is far below electric field values that would significantly affect the dust grain $\mathbf{g} \times \mathbf{B}$ drift motion.

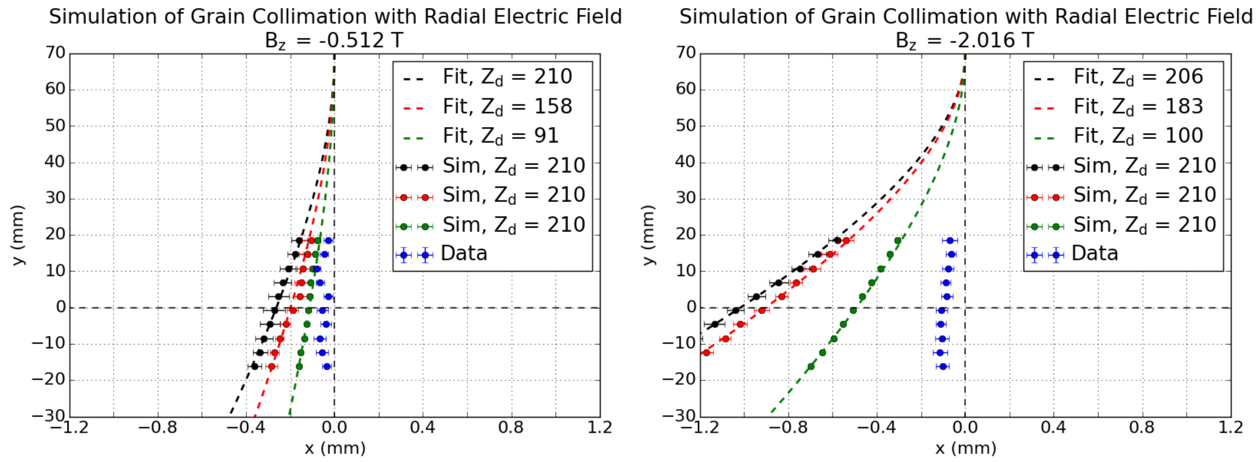

(a)

(b)

Figure 4.25: Parameters: $a_{\mathrm{d}} = 0.25$ μm, $Z_{\mathrm{d}} = 210$, $v_{\mathrm{o,y}} =$ -80 cm/s. Monte Carlo simulation trajectories according to the method described in Sec. (4.3.1) for a radially outward electric field given by Eq. (4.28). The values of the radial electric field are $E_{\mathrm{o}} =$ (0, 0.25, and 2.5) V/cm colored with black, red, and green. The blue data points are the measurement data from Sec. (4.2.3) and were provided for reference. a) $B_{\mathrm{z}} = -0.512$ T, b) $B_{\mathrm{z}} = -2.016$ T.

The trajectories shown in Fig. (4.23) are for only a single falling dust grain. The shape of the trajectories are also qualitatively similar to the data, so it could be possible that the collimation technique is not valid when a radial electric field is present. For this reason, we repeat the Monte Carlo analysis of the grain collimation technique discussed in Sec. (4.3.1) with the addition of the radial electric field given by Eq. (4.28). The results are summarized in Fig. (4.25) and clearly show that even when applying the Monte Carlo analysis to the collimated dust grains, the simulated deflection curves do not align with the data. Therefore, we conclude that even in the unlikely case that radial plasma sheath electric fields with a strength of the order 2.5 V/cm were able to penetrate deep into the plasma bulk, the influence of the radially inward electric force on the dust grains does not explain the large reduction in the dust grain $\mathbf{g} \times \mathbf{B}$ deflection measurement.

An azimuthal force

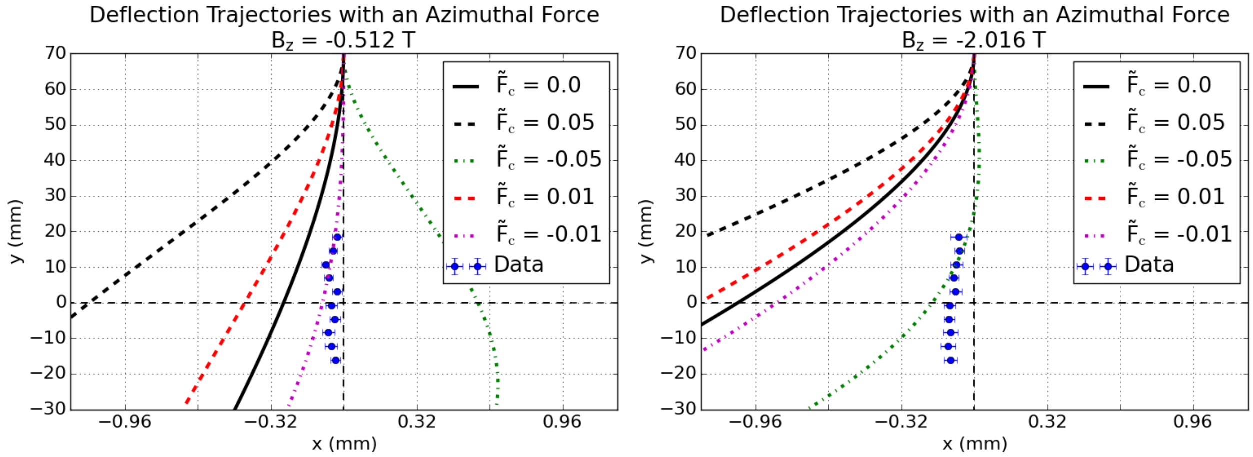

(a) (b)

Figure 4.26: Parameters: a_d = 0.25 μm, Z_d = 210, $v_\mathrm{o,y}$ = -80 cm/s. Grain trajectories for an azimuthal force with either a CW ($F_\mathrm{o} > 0$) or CCW ($F_\mathrm{o} < 0$) rotation according to Eq. (4.30). a) $B_\mathrm{z} = -0.512$ T, b) $B_\mathrm{z} = -2.016$ T.

In this section, the equations of motion from Sec. (2.2) are modified with an additional azimuthal force. The azimuthal force is assumed to have a linear radial dependence that pushes the falling dust grains either clockwise (CW) or counter-clockwise (CCW). The linear radial dependence was chosen because the presence of an azimuthal force may correspond to, for example, an **E** × **B** driven ion drag force such as those observed in [142, 50, 143]. Depending on the direction of the radial electric field, this azimuthal drag force may either be clockwise or counter-clockwise. The azimuthal force was modeled as

$$\mathbf{F}_\mathrm{c}(r) = F_\mathrm{o}\frac{r[cm]}{7}\hat{\phi} \tag{4.30}$$

where F_o is a constant that can either be positive for CCW rotation or be negative for CW rotation, and r is the radial distance in cm.

The equations of motion were numerically integrated for several possible values of F_o at B_z = -0.512 T and B_z = -2.016 T. The dust charge was assumed to be $Z_\mathrm{d} = 210$. Fig. (4.26) summarizes the results where the azimuthal force was normalized to the gravitational force according to

$$\tilde{\mathbf{F}}_{\mathrm{c}}(r) = \frac{\mathbf{F}_{\mathrm{c}}(r)}{m_{\mathrm{d}} g}. \tag{4.31}$$

These results clearly show that the presence of an azimuthal force (whether resulting from an **E** x **B** driven ion drag or not), does not result in dust grain trajectories that align closely with the measured data. Therefore, the possibility of the presence of an azimuthal force has been ruled out.

Neutral drag reduction

In this section, the role of possibly anisotropic neutral gas drag is investigated. Anisotropy of the neutral gas drag could be caused by the continual downward stream of collimated dust grains pushing neutral gas particles out of the collimation region. If the grains are falling with sufficient frequency that the natural diffusion of the neutral gas is no longer able to repopulate the collimation region, then the neutral gas drag could be significantly modified. In particular, the neutral drag could be decreased in the y-direction due to a lack of neutrals and possibly increased in the x-direction because the neutral density would be slightly increased along the collimation zone walls. This possibility was explored by applying the following modification of the Epstein drag that was presented in Sec. (1.2.5):

$$\mathbf{F}_{\mathrm{D}} = -\frac{4}{3}\pi a_{\mathrm{d}}^{2} m_{\mathrm{n}} v_{\mathrm{th,n}} n_{\mathrm{n}} \boldsymbol{\delta} \cdot \mathbf{v}\hat{\mathbf{v}} \tag{4.32}$$

where $\boldsymbol{\delta} = (\delta_{\mathrm{x}}, \delta_{\mathrm{y}})$ is used to alter the magnitudes of the x and y components of neutral drag.

The equations of motion were numerically integrated for several possible values of $(\delta_{\mathrm{x}}, \delta_{\mathrm{y}})$ at B_{z} = -0.512 T and B_{z} = -2.016 T. The dust charge was assumed to be $Z_{\mathrm{d}} = 210$. Fig. (4.27) summarizes the results. In the extreme limiting case where $\delta_{\mathrm{y}} = 0$ and $\delta_{\mathrm{x}} = 2.88$, the simulated grain motion still does not closely align with the measured data. In this limiting case, the y-motion is in near free-fall, but due to the coupling between the x and y components of the motion through the magnetic force (i.e., $F_{\mathrm{x}} = -\omega_{\mathrm{d}} v_{\mathrm{y}}$ and $F_{\mathrm{y}} = \omega_{\mathrm{d}} v_{\mathrm{x}}$), the force in the x-direction is also substantially increased. Therefore, the depletion of neutral gas in the grain collimation zone does not affect the dust grain motion enough to cause a false observation of substantially reduced dust grain charge as shown in Sec. (4.2.3).

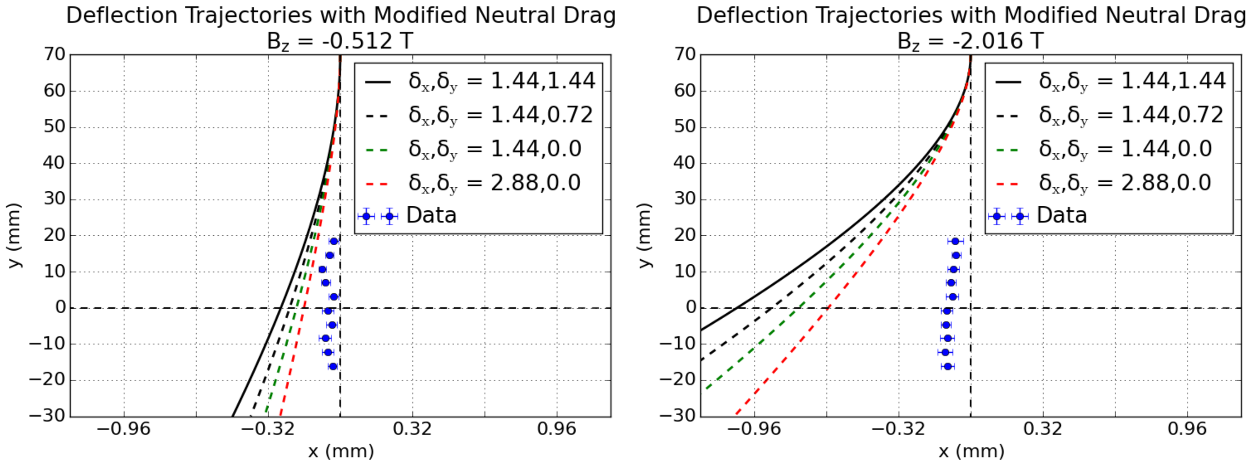

(a)

(b)

Figure 4.27: Parameters: $a_{\mathrm{d}} = 0.25\ \mu$m, $Z_{\mathrm{d}} = 210$, and $v_{\mathrm{o,y}}$ = -80 cm/s. Grain trajectories for a modified neutral drag according to Eq. (4.32). a) $B_{\mathrm{z}} = -0.512$ T, b) $B_{\mathrm{z}} = -2.016$ T.

4.3.3 Possible mechanisms for grain charge reduction

It has been demonstrated that the effects of radial electric fields, azimuthal forces, and neutral gas depletion are not able to explain the deflection measurements obtained from the $\mathbf{g} \times \mathbf{B}$ drift experiment. As a result, it is important to consider possible mechanisms for the apparent reduction of the dust charge in strong magnetic fields. There are effectively two possible ways in which the grain charge could be reduced in the plasma bulk in strong magnetic fields: First, the ion current to the grain is significantly increased. Second, the electron current to the grain is significantly decreased. Both of these situations will be examined in the following discussion.

$\mathbf{E} \times \mathbf{B}$ ion flows

As discussed in Sec. (1.3.2), there exists a slight modification to the usual OML theory to account for an ion drift speed [22]. For ions with a flow speed u_{f}, the shifted Maxwellian ion velocity distribution is

$$f_i(v_{\rm i}; u_{\rm f}) = \left(\frac{m_{\rm i}}{2\pi k_{\rm b} T_{\rm i}}\right)^{\frac{3}{2}} \exp - \left(\frac{m_{\rm i}(v_{\rm i} - u_{\rm f})^2}{2k_{\rm b} T_{\rm i}}\right). \tag{4.33}$$

When substituting Eq. (1.38) and Eq. (4.33) into Eq. (1.39) and completing the integration, the ion current to the grain becomes

$$I_{\rm i} = I_{\rm o,i} \left[F_1(\tilde{u}) + F_2(\tilde{u}) \frac{e^2 Z_{\rm d}}{4\pi\epsilon_{\rm o} a_{\rm d} k_{\rm b} T_{\rm i}}\right] \tag{4.34}$$

where $I_{\rm o,i}$ is given by Eq. (1.45), $\tilde{u} = u_{\rm f}/\sqrt{2k_{\rm b}T_{\rm i}/m_{\rm i}}$ is the normalized flow speed,

$$F_1(\tilde{u}) = \sqrt{\pi}\frac{(1 + 2\tilde{u}^2)\mathrm{erf}(4\tilde{u})}{4\tilde{u}} + \frac{\exp(-\tilde{u}^2)}{2}, \tag{4.35}$$

$$F_2(\tilde{u}) = \sqrt{\pi}\frac{\mathrm{erf}(\tilde{u})}{2\tilde{u}}, \tag{4.36}$$

and

$$\mathrm{erf}(\tilde{u}) = \frac{2}{\sqrt{\pi}} \int_0^{\tilde{u}} \exp{(-x^2)} dx \tag{4.37}$$

is the error function [28] that must be numerically integrated. In the limit $\tilde{u} \ll 1$, $\mathrm{erf}(\tilde{u}) \approx 2\tilde{u}/\sqrt{\pi}$ and Eq. (4.34) collapses to the usual OML current given by Eq. (1.44). In the fast flow speed limit where $\tilde{u} \gg 1$, $\mathrm{erf}(\tilde{u}) \approx 1$ and Eq. (4.34) becomes

$$I_{\rm i} = \pi a_{\rm d}^2 e n_{\rm o} u_{\rm f} \left[1 + \frac{e^2 Z_{\rm d}}{4\pi\epsilon_{\rm o} a_{\rm d} m_{\rm i} u_{\rm f}^2}\right], \tag{4.38}$$

which means that for very large values of the ion flow speed, the ion current no longer depends on the grain charge and increases linearly in $u_{\rm f}$.

Fig. (4.28) shows the ion charging current as a function of the flow speed $u_{\rm f}$ for several values of the grain charge $Z_{\rm d}$. At small values of $u_{\rm f}$, the ion current is only slightly decreased whereas when $u_{\rm f}$ increases to several tens of times the ion thermal speed, the ion currents

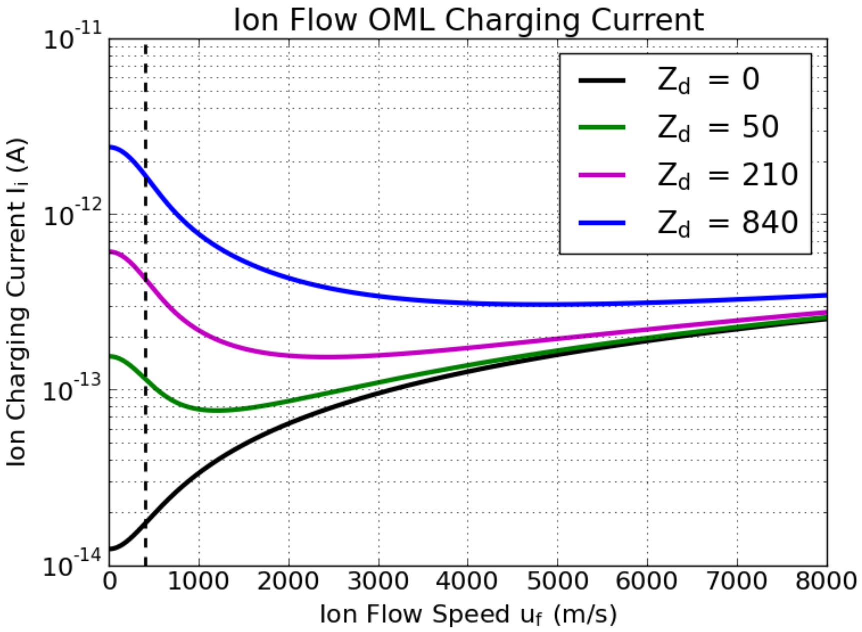

Figure 4.28: Parameters: $a_{\rm d} = 0.25$ μm, $k_{\rm b}T_{\rm i} = 0.025$ eV, $k_{\rm b}T_{\rm e} = 2.0$ eV, $n_{\rm e} = n_{\rm i} = 10^{15}$ m^{-3}. a) The ion charging current Eq. (4.34) versus ion flow speed for several fixed values of the grain charge $Z_{\rm d}$. The black dashed vertical line marks the thermal speed of room temperature ions where $k_{\rm b}T_{\rm i} = 0.025$ eV.

approach a linear dependence on $u_{\rm f}$ and become independent of the grain charge. For $\mathbf{E} \times \mathbf{B}$ driven ion flows in radial electric fields of the order $E_{\rm o} \approx 1$ V/cm, the flow speed is $u_{\rm f} \approx 100$ m/s. Ion flow speeds this small do not substantially change the ion current to the grain. Therefore, we conclude that possible $\mathbf{E} \times \mathbf{B}$ driven ion flows in the plasma bulk are unlikely to cause a significant deviation from the OML predicted value of the grain charge.

Ion magnetization effects

Recall that the $\mathbf{g} \times \mathbf{B}$ drift experiments were performed at a neutral gas pressure of $p_{\rm n} = 0.67$ Pa and magnetic field strengths of $B \geq 0.5$ T. At these neutral gas pressures and magnetic fields strengths, the ion Hall parameter is $H_{\rm i} \sim 100$ as shown in Fig. (1.1). This means that the ions undergo approximately 100 Larmor orbits before undergoing a collision with a neutral gas particle that may significantly alter the ion trajectory. Strictly speaking, the ions are quite magnetized. However, the ion Larmor radius is of the order $r_{\rm L,i} = 300$ μm, which is substantially larger than the dust grain radius $a_{\mathrm{d}} = 0.25\ \mu\mathrm{m}$. Therefore, the ions are still effectively unmagnetized on spatial scales comparable to the grain dimension. As a result, the physics of the ion current to the grain should still be relatively OML-like and is well described by Eq. (1.44).

Electron charging current reduction

During the discussion of the OML charging theory in Sec. (1.3.1), it was assumed that the electrons obey the Boltzmann relation given by Eq. (1.5). The Boltzmann relation bares the underlying assumption that the electrons quickly reach steady state and that the electric field force dominates the magnetic force on dust grains. However, it is very likely that the Boltzmann relation for the electrons is no longer true in the presence of strong magnetic fields. At the moment, it is an active area of research debate as to whether or not the Boltzmann relation still applies for strongly magnetized electrons in low temperature plasmas [144, 145, 146, 147]– although some authors have shown evidence that the Boltzmann relation is true in the sheath region but not in the pre-sheath or the bulk [148, 149, 150, 151]. For these reasons, in the authors opinion, it is unclear whether or not an OML-like dust grain charge should be expected in a magnetized plasma bulk. Therefore, possible mechanisms for grain charge reduction via the reduction of electron current to the grain are discussed for the remainder of this dissertation.

In order to examine the effect of electron current reduction, we modify the OML grain charging equation given by Eq. (1.53) to include an electron current reduction factor β^{-1}. The ion current is left unchanged. The new temporal dust charging equation then becomes

$$\frac{dZ_{\mathrm{d}}}{dt} = -4\pi a_{\mathrm{d}}^2 n_{\mathrm{o}} \sqrt{\frac{k_{\mathrm{b}} T_{\mathrm{e}}}{2\pi m_{\mathrm{e}}}} \left[\sqrt{\frac{m_{\mathrm{e}} T_{\mathrm{i}}}{m_{\mathrm{i}} T_{\mathrm{e}}}} \left(1 + \frac{e^2 Z_{\mathrm{d}}}{4\pi \epsilon_{\mathrm{o}} a_{\mathrm{d}} k_{\mathrm{b}} T_{\mathrm{i}}} \right) - \beta^{-1} \exp\left(-\frac{e^2 Z_{\mathrm{d}}}{4\pi \epsilon_{\mathrm{o}} a_{\mathrm{d}} k_{\mathrm{b}} T_{\mathrm{e}}} \right) \right]. \quad (4.39)$$

Before proceeding, it is important to note that the insertion of the reduction factor β is purely ad-hoc and at the current time, there is no first principles derivation of β. Nevertheless, β

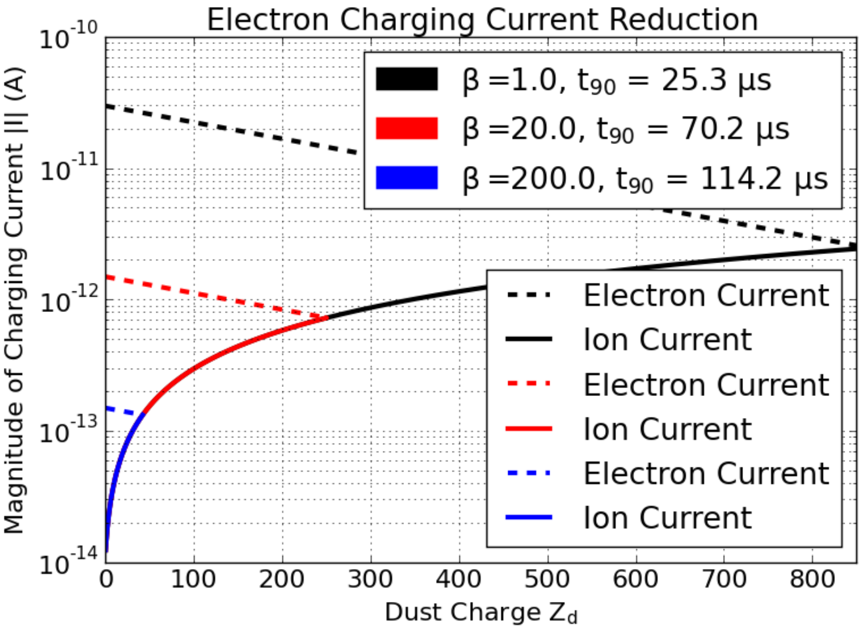

Figure 4.29: Parameters: $a_\mathrm{d} = 0.25\ \mu$m, $k_\mathrm{b}T_\mathrm{i} = 0.025$ eV, $k_\mathrm{b}T_\mathrm{e} = 2.0$ eV, $n_\mathrm{e} = n_\mathrm{i} = 10^{15}$ m^{-3}. The magnitude of the electron and ion charging currents are plotted as a function of the dust grain charge by solving Eq. (1.53) for several values of β. The time t_{90} is the time taken for the dust grain charge to reach 90% of its equilibrium value. The electron currents are dashed lines. The ion currents are the solid lines.

is used to determine to what extent the dust charge can be reduced by means of electron current reduction.

Eq. (4.39) was numerically integrated for several values of the electron current reduction factor β and is summarized in Fig. (4.29). When $\beta = 200$, the electron current is drastically reduced such that the equilibrium charge of the dust grain is only $Z_\mathrm{d} \approx 50$, which is in approximate agreement with the B = 0.512 T results shown in Sec. (4.2.3). The equilibrium charging timescale is approximately 25 μs for the $\beta = 1$ case and increases to 115 μs for the $\beta = 200$ case which shows that the charging timescale of the dust grains may also be increased in strong magnetic fields; however, in the $\mathbf{g} \times \mathbf{B}$ drift experiments performed in this dissertation, the dust grains were in the plasma for tens of milliseconds which is much larger than the equilibrium charging timescale estimation presented in this model. Based on the results shown in Fig. (4.29), a reduced electron charging current may be able to explain the reduced grain charge observations. For the remainder of this dissertation, we hypothesize about mechanisms through which the electron current can be reduced.

Electron magnetization and flux tubes

The electrons are significantly more magnetized than the ions and have a Hall parameter of $H_\mathrm{e} \sim 10^4$ with a Larmor radius at B = 0.5 T of $r_\mathrm{L,e} = 10$ μm (see Fig. (1.2)) that is comparable to the grain dimensions. Also, recall that the electron mean free path at $p_\mathrm{n} = 0.67$ Pa is $\lambda = 15$ cm. This means that the electrons are effectively collisionless between the 11 cm spacing of the MDPX electrodes. As a result, there is very little electron diffusion perpendicular to the magnetic field and the electron charging currents to the grain become flux-tube limited. This means that electrons beyond 1 Larmor diameter away from the dust grain are unlikely to strike the dust grain. This effect is illustrated in Fig. (4.30).

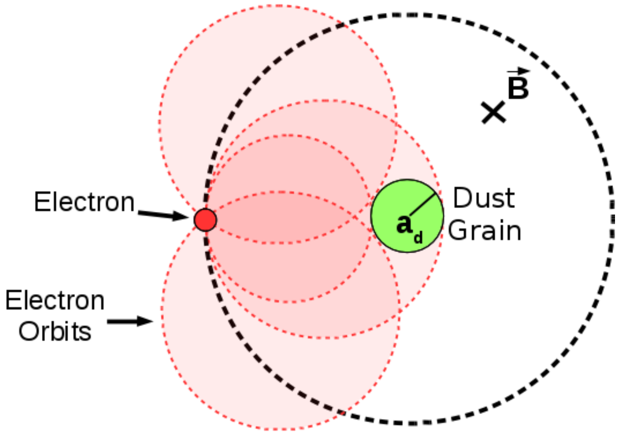

Figure 4.30: A 2D cartoon illustration of flux-tube limited dust grain charging. At a fixed radial position, there is only a very small range of perpendicular velocities corresponding to Larmor orbits that will intersect with the grain. This most probable Larmor radius is given by $r_\mathrm{L,e} = m_\mathrm{e} v_\mathrm{th,e}/(eB)$.

In addition to flux-tube limited charging, the characteristic inter-electron spacing when $n_\mathrm{e} \approx 10^{15}$ m^{-3} is $d_\mathrm{e} \approx 10$ μm, which is of the order the Larmor radius at B = 0.5 T. In the unmagnetized case, this fact goes relatively unnoticed due to the large electron thermal speed leading to a large flux of electrons to the grain from anywhere within a mean free path of the dust grain. However, when the electrons become magnetized, they are no longer able to freely move perpendicular to the magnetic field and the volume from which they originate is significantly reduced. The characteristic spatial scales for the electrons are summarized in Fig. (4.31).

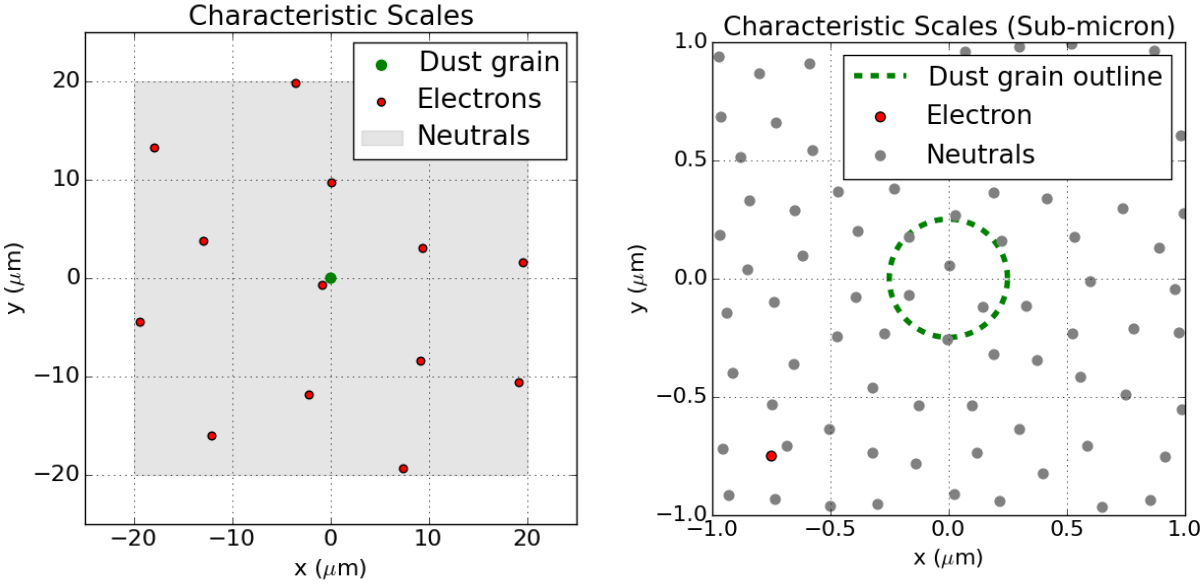

(a)

(b)

Figure 4.31: Parameters: $n_{\mathrm{e}} = 10^{15}$ m^{-3} at $p_{\mathrm{n}} = 0.67$ Pa. a) The electron (red dots) inter-particle spacing is to scale. The inter-neutral spacing is so small that it appears continuously gray in color. The electron size and dust grain size (green dot) are not to scale. b) This is part a) zoomed in to the sub-micron scale and was adapted from Fig. (2.1b). The electron (red dot in the lower left hand corner) is the only one present on this small scale due to the large inter-electron spacing. The inter-neutral spacing can now be seen as a random distribution of gray dots. The dust grain outline (green dashes) is to scale whereas the electron (red dot) size and the neutral (gray dots) sizes are not to scale.

The flux-tubes can be better understood by considering the Lagrangian of an electron in both the centrally repulsive electric field of the negatively charged dust grain and an axial magnetic field. The Lagrangian in polar coordinates (ρ, ϕ) is

$$\mathcal{L} = \frac{1}{2} m_{\mathrm{e}} \dot{\rho}^2 + \frac{1}{2} m_{\mathrm{e}} \rho^2 \dot{\phi}^2 - e\rho\dot{\phi}A_{\phi} + e\Phi_{\mathrm{d}}(\rho) \tag{4.40}$$

where $\Phi_{\mathrm{d}}(\rho)$ is given by Eq. (1.11) and

$$A_{\phi} = \frac{\rho B_{\mathrm{z}}}{2}\hat{\phi} \tag{4.41}$$

is the vector magnetic potential satisfying $\mathbf{B} = \nabla \times \mathbf{A}$ for an axial magnetic field pointing along the $\hat{\mathbf{z}}$ direction. When substituting Eq. (4.41) into Eq. (4.40), we get

$$\mathcal{L} = \frac{1}{2}m_{\mathrm{e}}\dot{\rho}^2 + \frac{1}{2}m_{\mathrm{e}}\rho^2\dot{\phi}^2 - \frac{1}{2}m_{\mathrm{e}}\rho^2\omega_{\mathrm{c,e}}\dot{\phi} + e\Phi_{\mathrm{d}}(\rho). \tag{4.42}$$

Eq. (4.42) is the standard Lagrangian function commonly found in textbooks such as [152, 153]. The Lagrangian does not contain explicit dependence on the coordinate ϕ, so we immediately know that the canonical angular momentum

$$p_{\phi} = \frac{\partial \mathcal{L}}{\partial \dot{\phi}} = m_{\mathrm{e}}\rho^2\left(\dot{\phi} - \frac{\omega_{\mathrm{c,e}}}{2}\right) \tag{4.43}$$

is a constant of the motion. It is important to note here that p_{ϕ} here is analogous to J in Sec. (1.3.2). This is an unfortunate notational clash that could not be avoided because the literature pertaining to the ion trapping discussed in Sec. (1.3.2) historically uses J as opposed to the canonical angular momentum p_{ϕ}. In the absence of a magnetic field (i.e. $\omega_{\mathrm{c,e}} = 0$), the canonical angular momentum is the angular momentum. However, since $\omega_{\mathrm{c,e}}$ is nonzero, p_{ϕ} is the appropriate notation. The canonical radial momentum is given by

$$p_{\rho} = \frac{\partial \mathcal{L}}{\partial \dot{\rho}} = m_{\mathrm{e}}\dot{\rho}. \tag{4.44}$$

Eqs. (4.42 – 4.44) can be used to derive the Hamiltonian of the system

$$\mathcal{H} = \frac{1}{2m_{\mathrm{e}}}p_{\rho}^2 + U_{\mathrm{eff}}(\rho) \tag{4.45}$$

where

$$U_{\text{eff}}(\rho) = \frac{1}{2m_{\text{e}}\rho^2}\left(p_\phi + m_{\text{e}}\rho^2\frac{\omega_{\text{c,e}}}{2}\right)^2 - e\Phi_{\text{d}}(\rho) \tag{4.46}$$

is the 2D effective potential. Eq. (4.46) tells us that for each particular value of the canonical angular momentum p_ϕ, there is a corresponding effective potential U_{eff} that depends only on the polar radial coordinate ρ. Several possible U_{eff} curves are shown in Fig. (4.32).

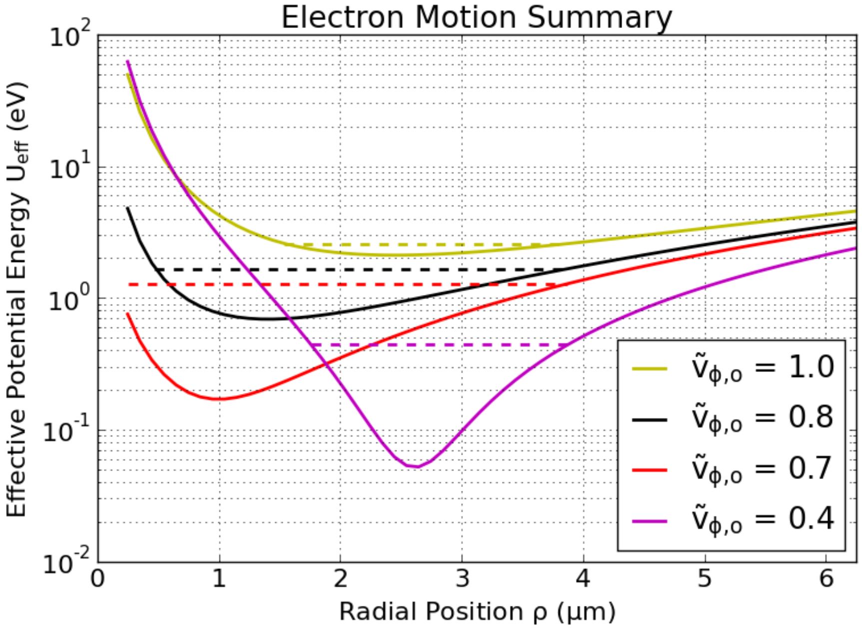

Figure 4.32: Parameters: $B_z = 2$ T, $Z_{\text{d}} = 100$, $n_{\text{e}} = n_{\text{i}} = 10^{15}$ m^{-3}. Several possible effective potentials governing the electron motion. The angular speeds are normalized such that $\tilde{v}_{o,\phi} = v_{o,\phi}/v_{\text{th,e}}$. The color scheme used here is also applied to Fig. (4.33) where more detail about simulation parameters is given.

In order to better understand the electron dynamics, the equations of motion for the electron were solved and their trajectories superimposed onto their corresponding effective potential given by Eq. (4.46). A summary of the results is shown in Fig. (4.33). Recall that the canonical momentum p_ϕ is related to the angular speed $v_\phi = \rho\dot{\phi}$ through Eq. (4.43). By strategically choosing the initial starting location of the electron to be at $(x_{\text{o}}, y_{\text{o}}) = (-3.88, 0)$ μm such that $\phi = \pi$ and giving the electron an initial velocity vertically downward, the angular speed at the starting location will be given by $v_{o,\phi} = \rho_{\text{o}}\dot{\phi}_{\text{o}} = v_{o,y}\cos\phi$ where ρ_{o}

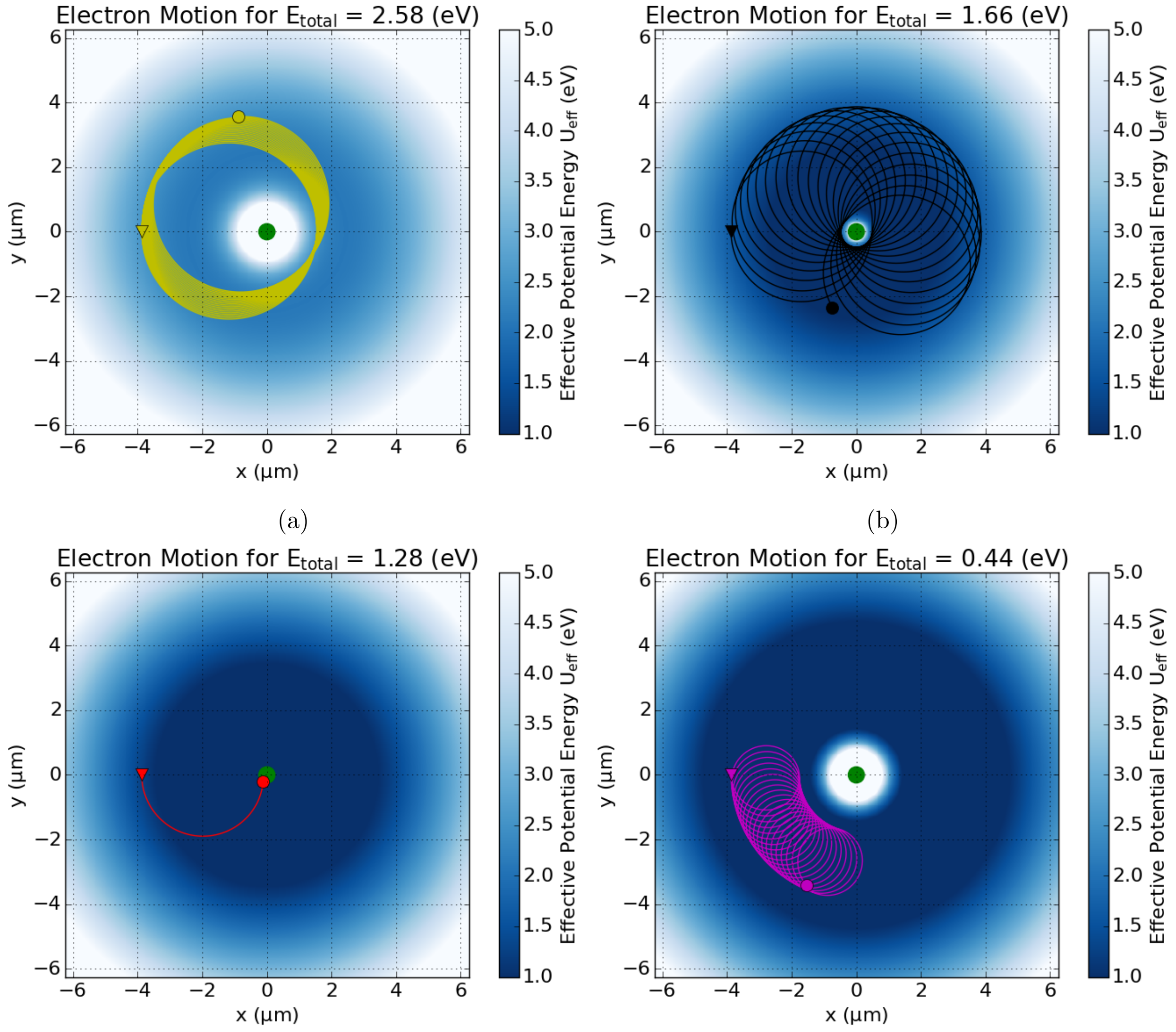

(a) (b)

(c) (d)

Figure 4.33: Parameters: $B_z = 2$ T, $Z_\mathrm{d} = 100$, $n_\mathrm{e} = n_\mathrm{i} = 10^{15}$ m^{-3}, $(x_\mathrm{o}, y_\mathrm{o}) = (-3.88, 0)$ μm, and $v_\mathrm{o,x} = 0$. Several electron trajectories are plotted and superimposed on top of their respective effective potential $U_\mathrm{eff}(\rho)$ given by Eq. (4.46). The angular speeds are normalized such that $\tilde{v}_{o,\phi} = v_{o,\phi}/v_\mathrm{th,e} = v_{o,y}/v_\mathrm{th,e}$ since $v_{o,y}$ was initially chosen to be straight down from an initial position that was on the x-axis. a) $\tilde{v}_{o,\phi} = 1.0$. b) $\tilde{v}_{o,\phi} = 0.8$. c) $\tilde{v}_{o,\phi} = 0.7$. d) $\tilde{v}_{o,\phi} = 0.4$.

$= 3.88$ μm. The initial condition specifies p_ϕ (a constant of the motion), and the effective potential U_{eff} can then be plotted for that particular value of p_ϕ.

The electron trajectories for several values of the angular velocity $v_{\phi,\mathrm{o}}$ are summarized in Fig. (4.33). Based on the electron trajectories, it becomes obvious that at a particular location in space, only a very small range of electron perpendicular velocities correspond to Larmor orbits which intersect with the dust grain. The curves in Fig. (4.33c) are color-coded according to Fig. (4.32). In most cases, the electron trajectory will either encompass the grain as shown by the yellow and black curves or never come close to the grain as shown in the purple curve. The red curve is the only case for which the total energy of the electron exceeds the repulsive effective potential and is able to hit the dust grain. In principle, there exists many more possible sets of initial conditions that are able to strike the dust grain for the particular value of $\tilde{v}_{\phi,\mathrm{o}} = 0.7$; however, recall that the electrons are usually treated as Maxwellian distributed with an energy of approximately $k_{\mathrm{b}}T_{\mathrm{e}} = 2$ eV, which places a limit on the most probable values for the components of the electron velocity.

When the concept of electrons being trapped in 2D effective potential wells is extended into the z-direction, the 2D circular orbit becomes a 3D flux tube. Electrons with a perpendicular distance from the grain $\rho > 2r_{\mathrm{L,e}}$ have trajectories that, regardless of their z-position, will never intersect with the dust grain. In this way, each dust grain has a corresponding cylindrical flux-tube volume from which electrons may be collected. Conversely, in the OML theory case with unmagnetized electrons, the collection volume is a sphere. Therefore, the total collection volume from which electrons may strike the dust grain is reduced from a spherical to cylindrical shape when the electrons become strongly magnetized. As a very crude geometric argument, consider the ratio of the volume of a flux-tube limited cylinder to the volume of the Debye sphere surrounding a typical dust grain. This ratio can be expressed as

$$\tilde{V} = \frac{V_{\mathrm{B}}}{V_{\mathrm{d}}} = \frac{\pi r_{\mathrm{L,e}}^2 h}{\frac{4}{3}\pi L_{\mathrm{d}}^3} \tag{4.47}$$

where the height of the flux-tube cylinder is h and $L_{\mathrm{d}} \approx L_{\mathrm{i}} \approx 30\ \mu$m for ions at $k_{\mathrm{b}}T_{\mathrm{i}} = 0.025$ eV and $n_{\mathrm{i}} = 10^{15}$ m^{-3}. When substituting Eq. (1.17) for $r_{\mathrm{L,e}}$ of $k_{\mathrm{b}}T_{\mathrm{e}} = 2$ eV electrons, Eq. (4.47) becomes

$$\tilde{V} \approx \frac{0.05}{B^2[T]} \tag{4.48}$$

where the magnetic field strength B is given in Tesla and the height of the flux-cylinder was assumed to be $h = L_\mathrm{d}$. Although this approximation is crude, it clearly illustrates that the volume from which electrons may come from to be collected by the dust grain is reduced by a factor of approximately 20. Furthermore, in reality the electrons may stream in to strike the grain from well outside the dust Debye sphere which further decreases the ratio given by Eq. (4.48). This simple geometric argument shows that there is a large reduction in the collection volume from which the electrons may be collected by the dust grain; however, the flux of electrons within the cylindrical flux tube volume is unknown and will be the subject of future investigations.

Kinetic electron charging

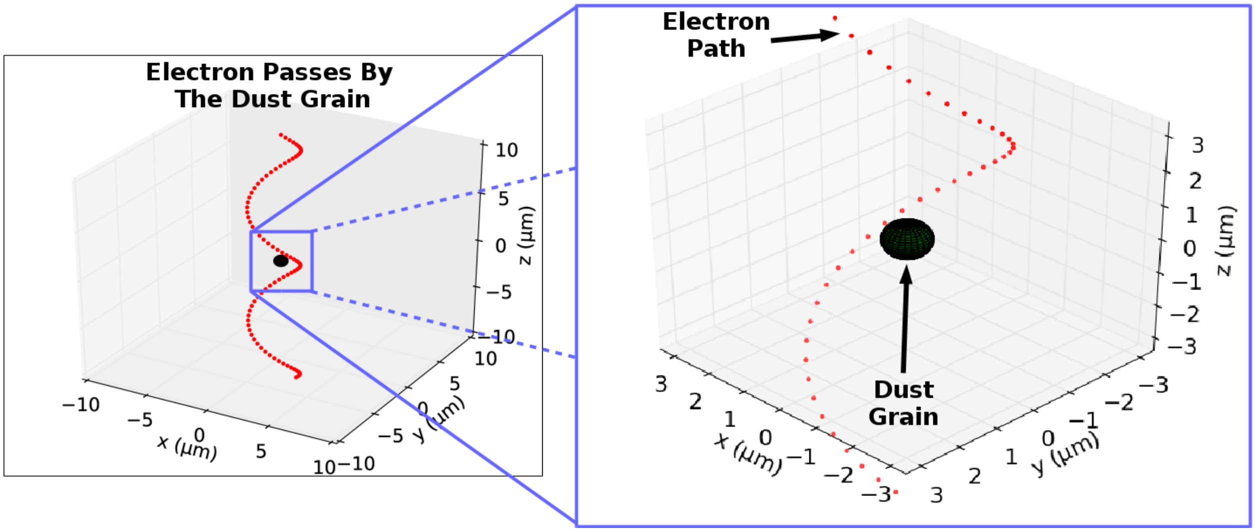

Figure 4.34: An example 3D simulation of an electron spiraling around a magnetic field. Because the electron's pitch angle is large, the electron orbit skips over the dust grain as it travels along the z-direction.

To further illustrate the idea that the electron charging current to the grain is significantly reduced, the z-component of the electron motion within a flux tube also needs to be taken into account. Even if the electron has the correct Larmor orbit such that geometrically speaking, it can intersect with the dust grain, a large parallel velocity will cause the electron to effectively skip over the dust grain while spiraling along the magnetic field. This is illustrated in Fig. (4.34). The maximum distance traveled along the magnetic field can be approximated as

$$\Delta z = v_{\mathrm{th,e}} \Delta t = v_{\mathrm{th,e}} \frac{2\pi}{\omega_{\mathrm{c,e}}} \tag{4.49}$$

where Δz is the distance traveled along the field. In this case, assuming $k_{\mathrm{b}} T_{\mathrm{e}} = 2.0$ eV to obtain the electron thermal speed,

$$\Delta z \approx \frac{34}{B[T]} \mu\mathrm{m} \tag{4.50}$$

where the magnetic field strength B is given in Tesla. Based on Eq. (4.50), it is easy to see that for an electron spiraling along the magnetic field line, if the parallel velocity is even 1/10th of the thermal speed, then the Δz is still much larger than the $a_{\mathrm{d}} = 0.25$ μm dust grains used in the $\mathbf{g} \times \mathbf{B}$ drift experiments.

4.3.4 Closing remarks and directions for future work

Some additional insight into the nature of electron motion and dust grain charging in strong magnetic fields is provided by extending the effective potential given by Eq. (4.46) to include the z-component such that

$$U_{\mathrm{eff}}(\rho, z) = \frac{1}{2 m_{\mathrm{e}} \rho^2} \left(p_\phi + m_{\mathrm{e}} \rho^2 \frac{\omega_{\mathrm{c,e}}}{2} \right)^2 - e \Phi_{\mathrm{d}}(\rho, z) \tag{4.51}$$

where Φ_{d} is given by Eq. (1.11) while making the substitution $r = \sqrt{\rho^2 + z^2}$ and noting that $\Phi_{\mathrm{d}} < 0$ so that the potential is repulsive between the negatively charged grain and the electron. Two possible electron trajectories in the effective potential given by Eq. (4.51) are shown in Fig. (4.35). The initial conditions of the two electrons are identical except the initial y-position y_{o}, which is changed by $1.3 \cdot 10^{-5}$ %. The two electrons follow the same trajectory while traveling in the $-\hat{\mathbf{z}}$ direction. They scatter off the dust grain and undergo approximately three Larmor orbits in the z = 0 plane after which one electron scatters backwards and the other scatters forward. Fig. (4.35b) is a superposition of the electron motion and the effective potential given by Eq. (4.51) where the unstable equilibrium in the z = 0 plane is clearly shown.

This example shows extreme sensitivity to initial conditions and further highlights the complicated dynamics that electrons will undergo at the micron scale when scattering off of micron sized dust grain in a strong magnetic field where the Larmor orbit is only a few microns in diameter. A detailed study of the electron scattering function for various values of the impact parameter needs to be performed. Chaotic electron motion in strong magnetic fields has been simulated for the attractive Coulomb potential between an electron and positively charged ion [154]; however, to the best of the author's knowledge, no such analysis has been done for strongly magnetized electrons interacting with the Debye potential of a negatively charged dust grain. Furthermore, this same analysis could be further extended to ion motion in the vicinity of the dust grain where the interaction is attractive. It may be possible for ions to become trapped — similar to the discussion in at the beginning of Sec. (1.3.2).

In addition to the Hamiltonian analysis performed above, a Monte Carlo analysis of electron trajectories could also be performed by randomly sampling sets of initial conditions for the electron motion. The electron velocity components could be randomly sampled from a Maxwellian distribution at temperature $k_\mathrm{b}T_\mathrm{e}$ and the initial positions randomly sampled from a uniform distribution within a defined simulation volume. If the space of initial conditions were sampled densely enough at several values of magnetic field strength, the ratio of electrons striking the grain could be used to gain an understanding of dust grain charging in strong magnetic fields.

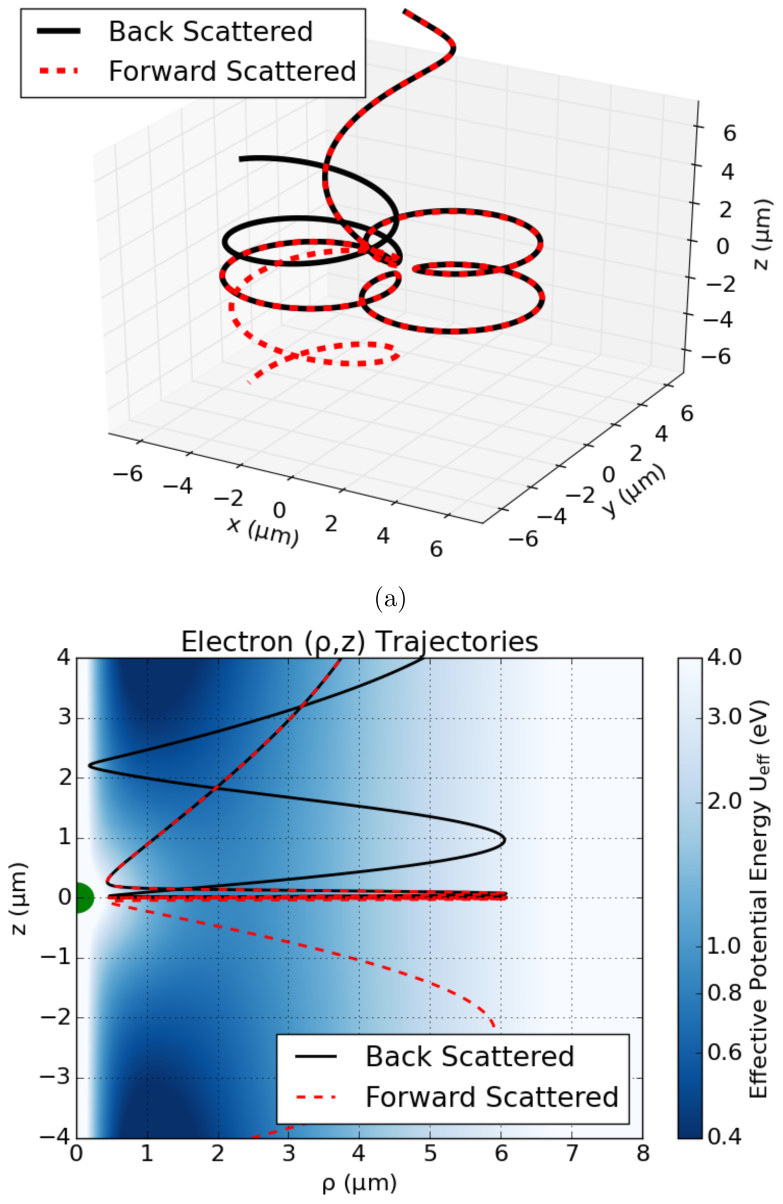

(a)

(b)

Figure 4.35: Parameters: a_d = 0.25 μm, Z_d = 1000, B = 2 T, $(x_\mathrm{o}, z_\mathrm{o}) = (0, 12.89141)$ μm, $(v_\mathrm{o,x}, v_\mathrm{o,y}, v_\mathrm{o,z}) = (0.5, 0.5, -\sqrt{2}/2)v_\mathrm{th,e}$, $y_\mathrm{o} = 0.3174858$ μm (black solid line), and $y_\mathrm{o} = 0.3174860$ μm (red dashed line). The equations of motion for each electron were integrated separately and there was no interaction between the electrons. Both figures have been spatially magnified and the initial locations of the electrons is not in view. The red and black electrons are "launched" in the $-\hat{\mathbf{z}}$ direction with nearly the same initial conditions. The overlapping trajectories appear as a red and black dashed line at the upper portion of the plots. The trajectories do not separate until they come close to the $z = 0$ plane. a) Trajectories in (x, y, z) space of two electrons. The red electron is forward scattered into the $-\hat{\mathbf{z}}$ direction and the black electron back scattered into the $\hat{\mathbf{z}}$ direction. b) Trajectories in cylindrical (ρ, z) space where $\rho = \sqrt{x^2 + y^2}$ of the electrons superimposed on the effective potential given by Eq. (4.51).

Chapter 5

Summary and Outlook

This experimental investigation into the nature of dust grain charging in strong magnetic fields has two primary results. First, the measurements presented here are based on observations of dust grain $\mathbf{g} \times \mathbf{B}$ deflection, which is a direct magnetization effect on the dust grains. To the best of the author's knowledge, this is the first observation of a direct magnetization effect on dust grains in a low temperature RF plasma bulk. One of the primary physics missions of the Magnetized Dusty Plasma Experiment (MDPX) was, arguably, to observe direct magnetization effects on the dust grains. In addition, this magnetization effect was observed with a very small dust grain Hall parameter (of the order 10^{-4}), which is a value far below which one would have a reasonable expectation of observing dust grain Larmor motion in a plasma sheath. The $\mathbf{g} \times \mathbf{B}$ magnetization effect was observable because of the unique geometry of this experiment where the dust grains were falling through the plasma bulk under the influence of the gravitational force. The gravitational force was a large external driving force that prevented the neutral gas drag from bringing the dust grains to rest — thus allowing for the measurement of very small magnetization effects over a vertical distance traveled of approximately 4 cm.

Second, the measured dust grain charge was significantly less than the value predicted by the unmagnetized OML charging theory. A careful analysis of the dust grain deflection and some initial modeling was presented in Sec. (4.3.3) and showed that a reduced dust grain charge is consistent with the experimental observations. In addition, the initial modeling also showed that the equilibrium charging timescale for the dust grains could be increased compared to the OML theory predictions. However, it was also shown that the increased equilibrium charging timescale cannot fully explain the reduced grain charge measurement presented in this work because the falling dust grains were in the plasma bulk for tens of milliseconds before entering the camera observation region. The dynamics of dust grain charging is significantly modified by the strong magnetization of electrons which could reduce the electron current to the dust grain and thus decrease the equilibrium charge. In particular, when the electron Larmor radii become comparable to the dust grain dimension, the charging volume surrounding a dust grain becomes flux-tube limited. A substantial fraction of the electrons within the flux-tube volume may also miss the dust grain as they undergo cycloidal motion along the magnetic field. These two factors may lead to a significantly reduced dust grain charge in comparison to the OML model.

The measurements performed in this experimental work provide new insight into the nature of dust grain charging dynamics in strongly magnetized plasmas. At this time, very little theoretical work has been done in this area. It is the author's hope that, as a result of the measurements presented in this dissertation, further theoretical and experimental investigations will be performed.

Bibliography

[1] V. Vahedi, G. DiPeso, C. K. Birdsall, M. A. Lieberman, and T. D. Rognlien, "Capacitive rf discharges modelled by particle-in-cell monte carlo simulation. i: Analysis of numerical techniques," *Plasma Sources Science and Technology*, vol. 2, no. 4, p. 261, 1993.

[2] V. Vahedi, G. DiPeso, C. K. Birdsall, M. A. Lieberman, and T. D. Rognlien, "Capacitive rf discharges modelled by particle-in-cell monte carlo simulation. ii: comparisons with laboratory measurements of electron energy distribution functions," *Plasma Sources Science and Technology*, vol. 2, no. 4, p. 273, 1993.

[3] M. Surendra, D. B. Graves, and G. M. Jellum, "Self-consistent model of a direct-current glow discharge: Treatment of fast electrons," *Phys. Rev. A*, vol. 41, pp. 1112–1125, 1990.

[4] W. Cramer, "Elastic and inelastic scattering of lowvelocity ions: Ne+ in a, a+ in ne, and a+ in a," *The Journal of Chemical Physics*, vol. 30, no. 3, pp. 641–642, 1959.

[5] D. Maoz, *Astrophysics in a Nutshell.* In a Nutshell, Princeton University Press, 2011.

[6] V. Dikarev, O. Preu, S. Solanki, H. Krger, and A. Krivov, "The local dust foregrounds in the microwave sky. i. thermal emission spectra," *The Astrophysical Journal*, vol. 705, pp. 670–682, 2009.

[7] L. Mestel and L. Spitzer, Jr, "Star formation in magnetic dust clouds," *Monthly Notices of the Royal Astronomical Society*, vol. 116, no. 5, pp. 503–514, 1956.

[8] J. Blum, G. Wurm, S. Kempf, T. Poppe, H. Klahr, T. Kozasa, M. Rott, T. Henning, J. Dorschner, R. Schräpler, H. U. Keller, W. J. Markiewicz, I. Mann, B. A. S. Gustafson, F. Giovane, D. Neuhaus, H. Fechtig, E. Grün, B. Feuerbacher, H. Kochan, L. Ratke, A. El Goresy, G. Morfill, S. J. Weidenschilling, G. Schwehm, K. Metzler, and W.-H. Ip, "Growth and form of planetary seedlings: results from a microgravity aggregation experiment," *Phys. Rev. Lett.*, vol. 85, pp. 2426–2429, 2000.

[9] B. A. Sargent, W. J. Forrest, C. Tayrien, M. K. McClure, D. M. Watson, G. C. Sloan, A. Li, P. Manoj, C. J. Bohac, E. Furlan, K. H. Kim, and J. D. Green, "Dust processing and grain growth in protoplanetary disks in the taurus-auriga star-forming region," *The Astrophysical Journal Supplement Series*, vol. 182, no. 2, pp. 477–508, 2009.

[10] T. W. Hartquist, O. Havnes, and G. E. Morfill, "The effects of charged dust on saturn's rings," *Astronomy & Geophysics*, vol. 44, no. 5, pp. 5.26–5.30, 2003.

[11] S. I. Popel, S. I. Kopnin, A. P. Golub', G. G. Dol'nikov, A. V. Zakharov, L. M. Zelenyi, and Y. N. Izvekova, "Dusty plasma at the surface of the moon," *Solar System Research*, vol. 47, no. 6, pp. 419–429, 2013.

[12] E. A. Lisin, V. P. Tarakanov, S. I. Popel, and O. F. Petrov, "Lunar dusty plasma: A result of interaction of the solar wind flux and ultraviolet radiation with the lunar surface," *Journal of Physics: Conference Series*, vol. 653, no. 1, p. 012139, 2015.

[13] E. C. Whipple, "Potentials of surfaces in space," *Reports on Progress in Physics*, vol. 44, no. 11, pp. 1197–1250, 1981.

[14] S. Barabash and R. Lundin, "On a possible dust-plasma interaction at mars," *IEEE Transactions on Plasma Science*, vol. 22, no. 2, pp. 173–178, 1994.

[15] D. S. Schmidt, J. D. Dent, and R. A. Schmidt, "Charge-to-mass ratio of individual blowing-snow particles," *Annals of Glaciology*, vol. 26, pp. 207–211, 1998.

[16] A. Michau, G. Lombardi, C. Arnas, L. C. Delacqua, M. Redolfi, X. Bonnin, and K. Hassouni, "Modelling of dust grain formation in a low-temperature plasma reactor used for simulating parasitic discharges expected under tokamak divertor domes," *Plasma Sources Science and Technology*, vol. 19, no. 3, p. 034023, 2010.

[17] G. Counsell, P. Coad, C. Grisola, C. Hopf, W. Jacob, A. Kirschner, A. Kreter, K. Krieger, J. Likonen, V. Philipps, J. Roth, M. Rubel, E. Salancon, A. Semerok, F. L. Tabares, A. Widdowson, and J. E. contributors, "Tritium retention in next step devices and the requirements for mitigation and removal techniques," *Plasma Physics and Controlled Fusion*, vol. 48, no. 12B, p. B189, 2006.

[18] G. S. Selwyn, J. E. Heidenreich, and K. L. Haller, "Particle trapping phenomena in radio frequency plasmas," *Applied Physics Letters*, vol. 57, no. 18, pp. 1876–1878, 1990.

[19] M. A. Lieberman, A. J. Lichtenberg, and S. E. Savas, "Model of magnetically enhanced, capacitive rf discharges," *IEEE Transactions on Plasma Science*, vol. 19, no. 2, pp. 189–196, 1991.

[20] H. Setyawan, M. Shimada, Y. Hayashi, and K. Okuyama, "Removal of particles during plasma processes using a collector based on the properties of particles suspended in the plasma," *Journal of Vacuum Science and Technology A: Vacuum, Surfaces and Films*, vol. 23, no. 3, pp. 388–393, 2005.

[21] Y. F. Li, U. Konopka, K. Jiang, T. Shimizu, H. Höfner, H. M. Thomas, and G. E. Morfill, "Removing dust particles from a large area discharge," *Applied Physics Letters*, vol. 94, no. 8, p. 081502, 2009.

[22] P. Shukla and A. Mamun, *Introduction to Dusty Plasma Physics.* Series in Plasma Physics, CRC Press, 2015.

[23] M. Bonitz, N. Horing, and P. Ludwig, *Introduction to Complex Plasmas.* Springer Series on Atomic, Optical, and Plasma Physics, Springer Berlin Heidelberg, 2010.

[24] G. Colonna, "Boltzmann and Vlasov equations in plasma physics," in *Plasma Modeling*, 2053-2563, pp. 1–1 to 1–23, IOP Publishing, 2016.

[25] P. Bellan, *Fundamentals of Plasma Physics.* Cambridge University Press, 2008.

[26] V. N. Tsytovich, G. E. Morfill, and H. Thomas, "Complex plasmas: I. complex plasmas as unusual state of matter," *Plasma Physics Reports*, vol. 28, no. 8, pp. 623–651, 2002.

[27] R. Haberman, *Applied Partial Differential Equations: With Fourier Series and Boundary Value Problems.* Pearson Prentice Hall, 2004.

[28] D. Zwillinger, *CRC Standard Mathematical Tables and Formulae, 31st Edition.* Advances in Applied Mathematics, CRC Press, 2002.

[29] J. Chu and L. I, "Direct observations of coulomb crystals and liquids in strongly coupled rf dusty plasmas," *Physical Review Letters*, vol. 72, p. 4009, 1994.

[30] H. Thomas, G. Morfill, V. Demmel, J. Goree, B. Feuerbacher, and D.Mohlmann, "Plasma crystal: Coulomb crystallization in a dusty plasma," *Physical Review Letters*, vol. 73, p. 652, 1994.

[31] V. A. Schweigert, I. V. Schweigert, A. Melzer, A. Homann, and A. Piel, "Alignment and instability of dust crystals in plasmas," *Phys. Rev. E*, vol. 54, pp. 4155–4166, 1996.

[32] I. V. Schweigert, V. A. Schweigert, A. Melzer, and A. Piel, "Melting of dust plasma crystals with defects," *Phys. Rev. E*, vol. 62, pp. 1238–1244, 2000.

[33] A. Melzer, V. A. Schweigert, I. V. Schweigert, A. Homann, S. Peters, and A. Piel, "Structure and stability of the plasma crystal," *Phys. Rev. E*, vol. 54, pp. R46–R49, 1996.

[34] G. Morfill, M. Rubin-Zuzic, H. Rothermel, A. Ivlev, B. Klumov, H. Thomas, and U. Konopka, "Highly resolved fluid flows: liquid plasmas at the kinetic level," *Physical Review Letters*, vol. 92, pp. 175004–1, 2004.

[35] C. Chan, Y. Lai, W. Woon, H. Chu, and L. I, "Dusty plasma liquids," *Plasma Physics and Controlled Fusion*, vol. 47, p. 273, 2005.

[36] P. Shukla, "Nonlinear waves and structures in dusty plasmas," *Physics of Plasmas*, vol. 10, p. 1619, 2003.

[37] E. Thomas, R. Fisher, and R. Merlino, "Observations of dust acoustic waves driven at high frequencies: Finite dust temperature effects and wave interference," *Physics of Plasmas*, vol. 10, p. 1619, 2003.

[38] A. Piel, O. Arp, M. Klindworth, and A. Melzer, "Obliquely propogating dust-density waves," *Physical Review E*, vol. 77, p. 026407, 2008.

[39] R. Merlino, "Dust-acoustic waves driven by an ion-dist streaming instability in laboratory discharge dusty plasma experiments," *Physics of Plasmas*, vol. 16, pp. 124501–01, 2009.

[40] E. Thomas, "Observations of high speed particle streams in dc glow discharge dusty plasmas," *Physics of Plasmas*, vol. 8, p. 329, 2001.

[41] Y. Feng, J. Goree, and B. Liu, "Energy transport in a shear flow of particles in a two-dimensional dusty plasma," *Physical Review E*, vol. 86, p. 056403, 2012.

[42] V. Nosenko, S. K. Zhdanov, A. V. Ivlev, G. E. Morfill, J. Goree, and A. Piel, "Heat transport in a two-dimensional complex (dusty) plasma at melting conditions," *Physical Review Letters*, vol. 100, pp. 1–4, 2008.

[43] J. Williams and E. Thomas, "Measurement of the kinetic dust temperature of a weakly coupled dusty plasma," *Physics of Plasmas*, vol. 13, p. 063509, 2006.

[44] V. Hohreiter, S. T. Wereley, M. G. Olsen, and J. N. Chung, "Cross-correlation analysis for temperature measurement," *Measurement Science and Technology*, vol. 13, p. 1072, 2002.

[45] S. Adachi, H. Totsuji, K. Takahashi, Y. Hayashi, and M. Takayanagi, "Particle temperature measurement using pair distribution function in complex plasmas," *Journal of Physics: Conference Series*, vol. 327, p. 012043, 2011.

[46] E. Thomas, J. D. Williams, and C. Rath, "Benchmarking particle image velocimetry measurements applied to dusty plasmas," *IEEE Transactions on Plasma Science*, vol. 38, pp. 892–896, 2010.

[47] S. Vladimirov, K. Ostrikov, and A. Samarian, *Physics and Applications of Complex Plasmas.* Imperial College Press, 2005.

[48] Epstein, P., "On the resistance experienced by spheres in their motion through gases," *Physical Review*, vol. 23, p. 710, 1924.

[49] K. Jiang, Y.Li, T. Shimizu, and et al., "Controlled particle transport in a plasma chamber with striped electrode," *Physics of Plasmas*, vol. 16, p. 123702, 2009.

[50] U. Konopka, D. Samsonov, A. Ivlev, J. Goree, V. Steinberg, and G. Morfill, "Rigid and differential plasma crystal rotation induced by magnetic fields," *Physical Review E*, vol. 61, no. 2, pp. 1890–8, 2000.

[51] J. Carstensen, H. Jung, F. Greiner, and A. Piel, "Mass changes of microparticles in a plasma observed by a phase-resolved resonance method," *Physics of Plasmas*, vol. 18, no. 3, 2011.

[52] G. Ivlev, A. andZhdanov, S. and Khrapak, S. and Morfill, "Ion drag force in dusty plasmas," *Plasma Phys. Control. Fusion*, vol. 46, 2004.

[53] G. E. Morfill, V. N. Tsytovich, and H. Thomas, “Complex plasmas: Ii. elementary processes in complex plasmas,” *Plasma Physics Reports*, vol. 29, no. 1, pp. 1–30, 2003.

[54] M. S. Barnes, J. H. Keller, J. C. Forster, J. A. O’Neill, and D. K. Coultas, “Transport of dust particles in glow-discharge plasmas,” *Phys. Rev. Lett.*, vol. 68, pp. 313–316, 1992.

[55] T. H. Hall and E. Thomas, “A study of ion drag for ground and microgravity dusty plasma experiments,” *IEEE Transactions on Plasma Science*, vol. 44, no. 4, pp. 463–468, 2016.

[56] C. Zafiu, A. Melzer, and A. Piel, “Measurement of the ion drag force on falling dust particles and its relation to the void formation in complex (dusty) plasmas,” *Physics of Plasmas*, vol. 10, no. 5, pp. 1278–1282, 2003.

[57] C. Zafiu, A. Melzer, and A. Piel, “Response to comment on measurement of the ion drag force on falling dust particles and its relation to the void formation in complex (dusty) plasmas [phys. plasmas 10, 4579 (2003)],” *Physics of Plasmas*, vol. 10, no. 11, pp. 4582–4583, 2003.

[58] V. Yaroshenko, S. Ratynskaia, S. Khrapak, M. H. Thoma, M. Kretschmer, H. Hfner, G. E. Morfill, A. Zobnin, A. Usachev, O. Petrov, and V. Fortov, “Determination of the ion-drag force in a complex plasma,” *Physics of Plasmas*, vol. 12, no. 9, p. 093503, 2005.

[59] V. Nosenko, R. Fisher, R. Merlino, S. Khrapak, G. Morfill, and K. Avinash, “Measurement of the ion drag force in a collisionless plasma with strong ion-grain coupling,” *Physics of Plasmas*, vol. 14, no. 10, p. 103702, 2007.

[60] S. Khrapak, a. Ivlev, G. Morfill, and H. Thomas, “Ion drag force in complex plasmas,” *Physical Review E*, vol. 66, no. 4, p. 046414, 2002.

[61] S. Khrapak and G. Morfill, “Dusty plasma in a constant electric field: Role of the electron drag force,” *Physical Review E*, vol. 69, p. 066411, 2004.

[62] E. Ivlev, S. Zhdanov, S. Khrapak, and G. Morfill, “Kinetic approach for the ion drag force in a collisional plasma,” *Physical Review E*, vol. 71, p. 016405, 2005.

[63] S. a. Khrapak, a. V. Ivlev, G. E. Morfill, H. M. Thomas, S. K. Zhdanov, U. Konopka, M. H. Thoma, and R. a. Quinn, “Comment on Measurement of the ion drag force on falling dust particles and its relation to the void formation in complex (dusty) plasmas [Phys. Plasmas 10, 1278 (2003)],” *Physics of Plasmas*, vol. 10, no. 11, p. 4579, 2003.

[64] H. M. Mott-Smith and I. Langmuir, “The Theory of Collectors in Gaseous Discharges,” *Physical Review*, vol. 28, pp. 727–763, 1926.

[65] Chen FF, *Plasma Diagnostic Techniques.* New York: New York : Academic, 1965.

[66] A. Piel, *Plasma Physics: An Introduction to Laboratory, Space, and Fusion Plasmas.* Springer Berlin Heidelberg, 2010.

[67] T. Matsoukas and M. Russell, "Particle charging in lowpressure plasmas," *Journal of Applied Physics*, vol. 77, no. 9, pp. 4285–4292, 1995.

[68] W. H. Press, S. A. Teukolsky, W. T. Vetterling, and B. P. Flannery, *Numerical Recipes 3rd Edition: The Art of Scientific Computing.* New York, NY, USA: Cambridge University Press, 3 ed., 2007.

[69] J. Goree, "Charging of particles in a plasma," *Plasma Sources Science and Technology*, vol. 3, no. 3, pp. 400–406, 1994.

[70] C. Cui and J. Goree, "Fluctuations of the charge on a dust grain in a plasma," *IEEE Transactions on Plasma Science*, vol. 22, p. 151, 1994.

[71] K. Lee and T. Matsoukas, "Can charge fluctuations explain particle growth in low-pressure plasmas?," *Journal of Applied Physics*, vol. 85, no. 4, pp. 2085–2092, 1999.

[72] I. B. Bernstein and I. N. Rabinowitz, "Theory of electrostatic probes in a lowdensity plasma," *The Physics of Fluids*, vol. 2, no. 2, pp. 112–121, 1959.

[73] J. E. Allen, B. M. Annaratone, and U. Angelis, "On the orbital motion limited theory for a small body at floating potential in a maxwellian plasma," *Journal of Plasma Physics*, vol. 63, no. 4, p. 299309, 2000.

[74] J. Goree, "Ion trapping by a charged dust grain in a plasma," *Physical Review Letters*, vol. 69, no. 2, pp. 277–280, 1992.

[75] M. Lampe, V. Gavrishchaka, G. Ganguli, and G. Joyce, "Effect of trapped ions on shielding of a charged spherical object in a plasma," *Physical Review Letters*, vol. 86, no. 23, pp. 5278–5281, 2001.

[76] M. Lampe, "Limits of validity for orbital-motion-limited theory for a small floating collector," *Journal of Plasma Physics*, vol. 65, no. 3, p. 171180, 2001.

[77] C. T. N. Willis, M. Coppins, M. Bacharis, and J. E. Allen, "The effect of dust grain size on the floating potential of dust in a collisionless plasma," *Plasma Sources Science and Technology*, vol. 19, no. 6, p. 065022, 2010.

[78] P. C. Stangeby, "Plasma sheath transmission factors for tokamak edge plasmas," *The Physics of Fluids*, vol. 27, no. 3, pp. 682–690, 1984.

[79] C. T. N. Willis, M. Coppins, M. Bacharis, and J. E. Allen, "Floating potential of large dust grains in a collisionless flowing plasma," *Phys. Rev. E*, vol. 85, p. 036403, 2012.

[80] R. V. Kennedy and J. E. Allen, "The floating potential of spherical probes and dust grains . II : Orbital motion theory," *Journal of Plasma Physics*, vol. 69, no. 6, pp. 485–506, 2003.

[81] J. E. Allen, "Probe theory - The orbital motion approach," *Physica Scripta*, vol. 45, pp. 497–503, 1992.

[82] J. E. Allen, R. L. F. Boyd, and P. Reynolds, "The collection of positive ions by a probe immersed in a plasma," *Proceedings of the Physical Society. Section B*, vol. 70, no. 3, p. 297, 1957.

[83] C. M. C. Nairn, B. M. Annaratone, and J. E. Allen, "On the theory of spherical probes and dust grains," *Plasma Sources Science and Technology*, vol. 7, no. 4, p. 478, 1998.

[84] R. V. Kennedy and J. E. Allen, "The floating potential of spherical probes and dust grains. Part 1. Radial motion theory," *Journal of Plasma Physics*, vol. 69, no. 6, pp. 485–506, 2002.

[85] U. Konopka, L. Ratke, and H. Thomas, "Central collisions of charged dust particles in a plasma," *Physical Review Letters*, vol. 79, p. 1269, 1997.

[86] A. Melzer, "Mode spectra of thermally excited two-dimensional dust coulomb clusters," *Phys. Rev. E*, vol. 67, p. 016411, 2003.

[87] A. Melzer, "Laser manipulation of particles in dusty plasmas," *Plasma Sources Science and Technology*, vol. 10, no. 2, p. 303, 2001.

[88] A. Homann, A. Melzer, and A. Piel, "Measuring the charge on single particles by laser-excited resonances in plasma crystals," *Phys. Rev. E*, vol. 59, pp. R3835–R3838, 1999.

[89] A. Piel, A. Homann, M. Klindworth, A. Melzer, C. Zafiu, V. Nosenko, and J. Goree, "Waves and oscillations in plasma crystals," *Journal of Physics B: Atomic, Molecular and Optical Physics*, vol. 36, no. 3, p. 533, 2003.

[90] H. Schollmeyer, A. Melzer, A. Homann, and A. Piel, "Dustdust and dust-plasma interactions of monolayer plasma crystals," *Physics of Plasmas*, vol. 6, no. 7, pp. 2693–2698, 1999.

[91] Y. Nakamura and O. Ishihara, "Measurements of electric charge and screening length of microparticles in a plasma sheath," *Physics of Plasmas*, vol. 16, no. 4, p. 043704, 2009.

[92] J. Carstensen, F. Greiner, and A. Piel, "Ion-wake-mediated particle interaction in a magnetized-plasma flow," *Physal Review Letters*, vol. 109, p. 135001, 2012.

[93] T. J. Sommerer, W. N. G. Hitchon, R. E. P. Harvey, and J. E. Lawler, "Self-consistent kinetic calculations of helium rf glow discharges," *Phys. Rev. A*, vol. 43, pp. 4452–4472, 1991.

[94] P. Belenguer, J. P. Blondeau, L. Boufendi, M. Toogood, A. Plain, A. Bouchoule, C. Laure, and J. P. Boeuf, "Numerical and experimental diagnostics of rf discharges in pure and dusty argon," *Phys. Rev. A*, vol. 46, pp. 7923–7933, 1992.

[95] A. V. Ivlev, R. Sütterlin, V. Steinberg, M. Zuzic, and G. Morfill, "Nonlinear vertical oscillations of a particle in a sheath of a rf discharge," *Phys. Rev. Lett.*, vol. 85, pp. 4060–4063, 2000.

[96] E. B. Tomme, B. M. Annaratone, and J. E. Allen, "Damped dust oscillations as a plasma sheath diagnostic," *Plasma Sources Science and Technology*, vol. 9, no. 2, p. 87, 2000.

[97] U. Gülan, B. Lüthi, M. Holzner, A. Liberzon, A. Tsinober, and W. Kinzelbach, "Experimental study of aortic flow in the ascending aorta via Particle Tracking Velocimetry," *Exp. in Fluids*, vol. 53, pp. 1469–1485, 2012.

[98] P. C. Nelson, C. Zurla, D. Brogioli, J. F. Beausang, L. Finzi, and D. Dunlap, "Tethered particle motion as a diagnostic of DNA tether length.," *The journal of physical chemistry. B*, vol. 110, 2006.

[99] S. Brinkers, H. R. C. Dietrich, F. H. de Groote, I. T. Young, and B. Rieger, "The persistence length of double stranded DNA determined using dark field tethered particle motion.," *The Journal of chemical physics*, vol. 130, 2009.

[100] S. Liu, B. Zhao, D. Zhang, C. Li, and H. Wang, "Imaging of nonuniform motion of single DNA molecules reveals the kinetics of varying-field isotachophoresis.," *Journal of the American Chemical Society*, vol. 135, 2013.

[101] Y. Chung, S. Hsiau, H. Liao, and J. Ooi, "An improved PTV technique to evaluate the velocity field of non-spherical particles," *Powder Technology*, vol. 202, pp. 151–161, 2010.

[102] J. K. M. Raffel,C. Willert, *Particle Image Velcimetry : A Practical Guide*. Germany: Springer, 1998.

[103] R. Adrian and J. Westerweel, *Particle Image Velocimetry*. Cambridge Aerospace Series, Cambridge University Press, 2011.

[104] R. E. S. Challa, M.R. Morelande, D.Musicki, *Fundamentals of object tracking*. New York: Cambridge University Press, 2011.

[105] R. Adrian, "Twenty years of particle image velocimetry," *Experiments in Fluids*, vol. 39, pp. 159–169, 2005.

[106] R. J. Adrian and C. S. Yao, "Pulsed laser technique application to liquid and gaseous flows and the scattering power of seed materials.," *Applied optics*, vol. 24, pp. 44–52, 1985.

[107] Y. Feng, J. Goree, and B. Liu, "Errors in particle tracking velocimetry with high-speed cameras.," *The Review of scientific instruments*, vol. 82, 2011.

[108] Keane, R. and Adrian, R. and Zhang, Y., "Super-resolution particle imaging velocimetry," *Measurement Science and Technology*, vol. 6, pp. 754–768, 1995.

[109] C. J. Kähler, S. Scharnowski, and C. Cierpka, "On the resolution limit of digital particle image velocimetry," *Experiments in Fluids*, vol. 52, pp. 1629–1639, 2012.

[110] C. J. Kähler, S. Scharnowski, and C. Cierpka, "On the uncertainty of digital PIV and PTV near walls," *Experiments in Fluids*, vol. 52, pp. 1641–1656, 2012.

[111] Lynch, B. and Konopka, U. and Thomas, E., "Real-time particle tracking in complex plasmas," *IEEE Transactions on Plasma Science*, vol. 44, no. 4, pp. 553–557, 2016.

[112] A. R. Joan S. Weszka, "Histogram modification for threshold selection," *IEEE Transactions of Systems, Man, and Cybernetics.*, vol. 9, pp. 38–52, 1979.

[113] N. Otsu, "A threshold selection method from gray-level histograms," *IEEE Transactions of Systems, Man, and Cybernetics.*, vol. 9, pp. 62–66, 1979.

[114] Y. Feng, J. Goree, and B. Liu, "Accurate particle position measurement from images.," *The Review of scientific instruments*, vol. 78, 2007.

[115] A. Glassner, "Fill 'er up![Graphics filling algorithms]," *IEEE Computer Graphics and Applications*, vol. 21, pp. 78–85, 2002.

[116] E. Thomas Jr, R. L. Merlino, and M. Rosenberg, "Magnetized dusty plasmas: the next frontier for complex plasma research," *Plasma Phys. Control. Fusion*, vol. 54, no. 54, pp. 124034–7, 2012.

[117] C. E. Miller, A. Radovinsky, and S. Pourrahimi, "Structural analyses of the cold mass for high field dusty plasma experiment," *IEEE Transactions on Applied Superconductivity*, vol. 24, no. 3, 2014.

[118] E. Thomas, A. M. DuBois, B. Lynch, S. Adams, R. Fisher, D. Artis, S. LeBlanc, U. Konopka, R. L. Merlino, and M. Rosenberg, "Preliminary characteristics of magnetic field and plasma performance in the Magnetized Dusty Plasma Experiment (MDPX)," *J. Plasma Phys.*, vol. 80, no. 06, pp. 803–808, 2014.

[119] E. Thomas and M. Merlino, R. Rosenberg, "Design criteria for the Magnetized Dusty Plasma eXperiment," *IEEE Transactions on Plasma Science*, vol. 41, 2013.

[120] H. Freeman, *Machine Vision for Three-Dimensional Scenes.* Acad. Press, 1990.

[121] Y. Wang, J. Zhang, L. Wu, and Z. Zhou, "Mean shift tracking algorithm based on multi-feature space and grey model," *Journal of Computational Information Systems*, vol. 6, pp. 3731–3739, 2010.

[122] T. Boggs, R. Byrd, J. Rogers, and R. Schnabel, "User's reference guide for odrpack version 2.01 software for weighted orthogonal distance regression nistir 4834," tech. rep., National Institute of Standards and Technology, 1992.

[123] D. Gurnett and A. Bhattacharjee, *Introduction to Plasma Physics: With Space and Laboratory Applications.* Cambridge University Press, 2005.

[124] J. Goedbloed and S. Poedts, *Principles of Magnetohydrodynamics: With Applications to Laboratory and Astrophysical Plasmas.* Cambridge University Press, 2004.

[125] H. Lorentz, "The motion of electrons in metallic bodies i," *Proceedings of the Royal Netherlands Academy of Arts and Sciences (KNAW)*, vol. 7, pp. 438–453, 1905.

[126] H. Lorentz, "The motion of electrons in metallic bodies ii," *Proceedings of the Royal Netherlands Academy of Arts and Sciences (KNAW)*, vol. 7, pp. 585–593, 1905.

[127] H. Lorentz, "The motion of electrons in metallic bodies iii," *Proceedings of the Royal Netherlands Academy of Arts and Sciences (KNAW)*, vol. 7, pp. 684–691, 1905.

[128] M. Lieberman and A. Lichtenberg, *Principles of Plasma Discharges and Materials Processing.* Wiley, 1994.

[129] S. Samukawa, T. Nakamura, T. Ishida, and A. Ishitani, "Optimally stable electron cyclotron resonance plasma generation and essential points for compact plasma source," *Japanese Journal of Applied Physics*, vol. 31, no. 12S, p. 4348, 1992.

[130] H. Akazawa, "Note: Easy-to-maintain electron cyclotron resonance (ecr) plasma sputtering apparatus featuring hybrid waveguide and coaxial cables for microwave delivery," *Review of Scientific Instruments*, vol. 87, p. 066104, 2016.

[131] M. Lieberman, "Analytical solution for capacitive RF sheath," *IEEE Transactions on Plasma Science*, vol. 16, no. 6, pp. 638–644, 1988.

[132] Y. Watanabe, M. Shiratani, H. Kawasaki, S. Singh, T. Fukuzawa, Y. Ueda, and H. Ohkura, "Growth processes of particles in high frequency silane plasmas," *Journal of Vacuum Science & Technology A: Vacuum, Surfaces, and Films*, vol. 14, no. 2, pp. 540–545, 1996.

[133] A. A. Howling, J. Dorier, C. Hollenstein, U. Kroll, and F. Finger, "Frequency effects in silane plasmas for plasma enhanced chemical vapor deposition," *Journal of Vacuum Science & Technology A: Vacuum, Surfaces, and Films*, vol. 10, no. 4, pp. 1080–1085, 1992.

[134] S. Khrapak, S. Ratynskaia, a. Zobnin, a. Usachev, V. Yaroshenko, M. Thoma, M. Kretschmer, H. Höfner, G. Morfill, O. Petrov, and V. Fortov, "Particle charge in the bulk of gas discharges," *Physical Review E*, vol. 72, no. 1, p. 016406, 2005.

[135] T. E. Sheridan, "Effect of radio frequency discharge power on dusty plasma parameters," *Journal of Applied Physics*, vol. 106, no. 3, 2009.

[136] D. Curreli and F. Chen, "Equilibrium theory of cylindrical discharges with special application to helicons," *Physics of Plasmas*, vol. 18, no. 11, p. 113501, 2011.

[137] F. Chen and D. Curreli, "Central peaking of magnetized gas discharges," *Physics of Plasmas*, vol. 20, no. 5, p. 057102, 2013.

[138] D. Curreli and F. Chen, “Cross-field diffusion in low-temperature plasma discharges of finite length,” *Plasma Sources Science and Technology*, vol. 23, 2014.

[139] A. Simon, “Ambipolar diffusion in a magnetic field,” *Phys. Rev.*, vol. 98, pp. 317–318, 1955.

[140] R. Bharuthram, I. U. of Pure, and A. Physics, *Dusty Plasmas in the New Millennium: Third International Conference on the Physics of Dusty Plasmas, Durban, South Africa, 20-24 May 2002*. AIP Conference Proceedings, American Inst. of Physics, 2002.

[141] D. Samsonov and J. Goree, “Instabilities in a dusty plasma with ion drag and ionization,” *Phys. Rev. E*, vol. 59, pp. 1047–1058, 1999.

[142] S. Nunomura, N. Ohno, and S. Takamura, “Effects of ion flow by E x B drift on dust particle behavior in magnetized cylindrical electron cyclotron resonance plasmas,” *Japanese Journal of Applied Physics, Part 1: Regular Papers and Short Notes and Review Papers*, vol. 36, no. 2, pp. 877–883, 1997.

[143] K. Matyash, M. Frhlich, H. Kersten, G. Thieme, R. Schneider, M. Hannemann, and r. Hippler, “Rotating dust ring in an rf discharge coupled with a dc-magnetron sputter source: Experiment and simulation,” *Journal of Physics D: Applied Physics*, vol. 37, no. 19, p. 2703, 2004.

[144] N. Sternberg, V. Godyak, and D. Hoffman, “Magnetic field effects on gas discharge plasmas,” *Physics of Plasmas*, vol. 13, no. 6, p. 063511, 2006.

[145] J. E. Allen, “Comment on magnetic field effects on gas discharge plasmas [phys. plasmas 13, 063511 (2006)],” *Physics of Plasmas*, vol. 14, no. 2, p. 024701, 2007.

[146] N. Sternberg, V. Godyak, and D. Hoffman, “Response to comment on magnetic field effects on gas discharge plasmas [phys. plasmas 13, 063511 (2006)],” *Physics of Plasmas*, vol. 14, no. 2, p. 024702, 2007.

[147] V. Godyak, N. Sternberg, and D. Hoffman, “Response to comment on magnetic field effects on gas discharge plasmas [phys. plasmas 13, 063511 (2006)],” *Physics of Plasmas*, vol. 14, no. 8, p. 084704, 2007.

[148] T. M. G. Zimmermann, M. Coppins, and J. E. Allen, “The effect of a magnetic field on a cylindrical object in a plasma,” *Physics of Plasmas*, vol. 16, no. 4, p. 043501, 2009.

[149] T. M. G. Zimmermann, M. Coppins, and J. E. Allen, “Erratum: the effect of a magnetic field on a cylindrical object in a plasma [phys. plasmas 16, 043501 (2009)],” *Physics of Plasmas*, vol. 16, no. 12, p. 129905, 2009.

[150] L. Nasi and J.-L. Raimbault, “On the boltzmann relation in a cold magnetized plasma,” *Physics of Plasmas*, vol. 17, no. 11, p. 113513, 2010.

[151] T. M. G. Zimmermann, M. Coppins, and J. E. Allen, “Coaxial discharge with axial magnetic field: Demonstration that the boltzmann relation for electrons generally does not hold in magnetized plasmas,” *Physics of Plasmas*, vol. 17, no. 2, p. 022301, 2010.

[152] H. Goldstein, C. Poole, and J. Safko, *Classical Mechanics.* Addison Wesley, 2002.

[153] S. Thornton and J. Marion, *Classical Dynamics of Particles and Systems.* Brooks/Cole, 2004.

[154] B. Hu, W. Horton, and T. Petrosky, "Coulomb scattering in a very strong magnetic field," *Physics of Plasmas*, vol. 9, no. 4, 2002.

[155] Boyce E. and DiPrima R.C., *Elementary Differential Equations and Boundary Value Problems.* Wiley, 2005.

Appendices

Appendix A

Dimensional schematics

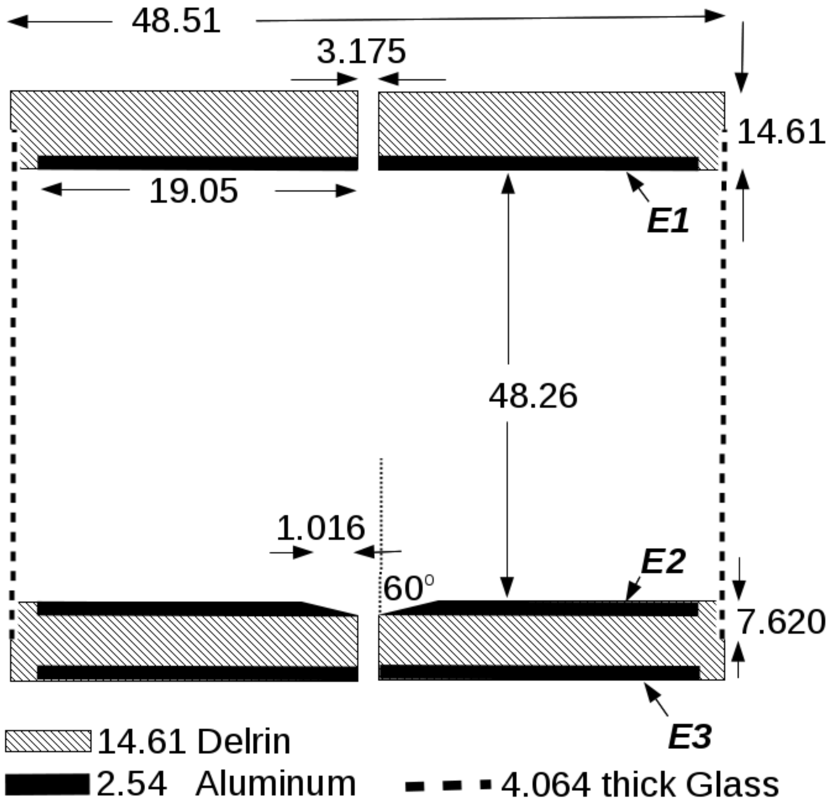

Figure A.1: A side-view dimensional schematic of the dropper electrodes and glass cylinder discussed in Sec. (4.1.1). All dimensions are given in units of millimeters. From top to bottom: Electrode 1 (E1) is grounded. Electrode 2 (E2) has an applied RF signal. Electrode 3 (E3) is an auxiliary electrode through which a DC signal may be applied to manipulate the plasma sheath as well as assist in confining the plasma to the dropper volume.

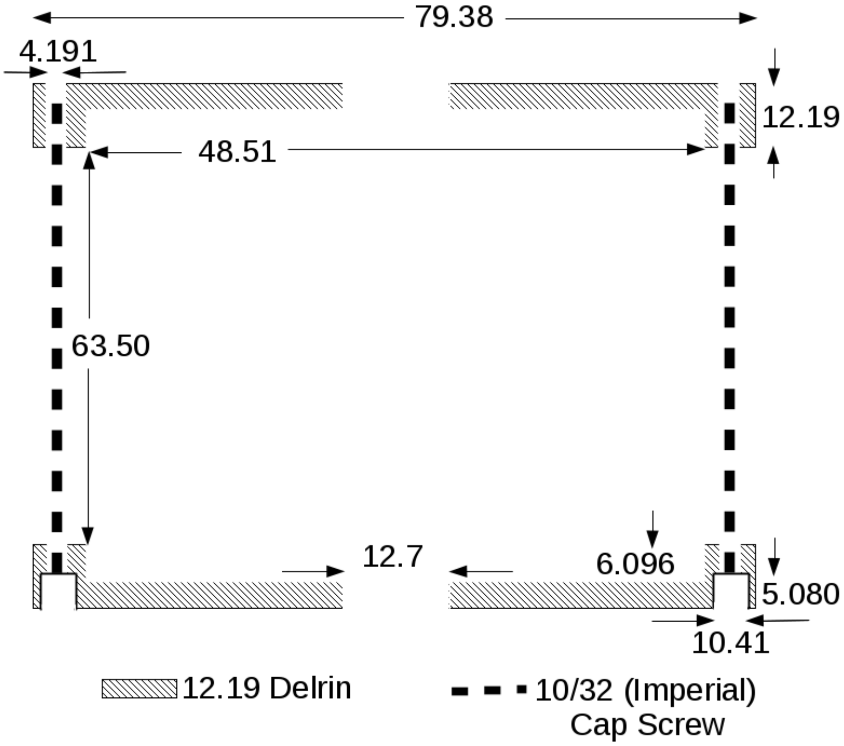

Figure A.2: A side-view dimensional schematic of the dropper mounting hardware used to attach the dropper to an ISO-100 vacuum port as discussed in Sec. (4.1.1). All dimensions are given in units of millimeters. The dropper electrodes (E1, E2, E3) and the glass cylinder pictured in Fig. (A.1) is placed between the Delrin brackets pictured in the schematic above. Four 10/32 (Imperial) cap screws are used to hold the entire assembly together as well as attach it to an ISO-100 vacuum port.

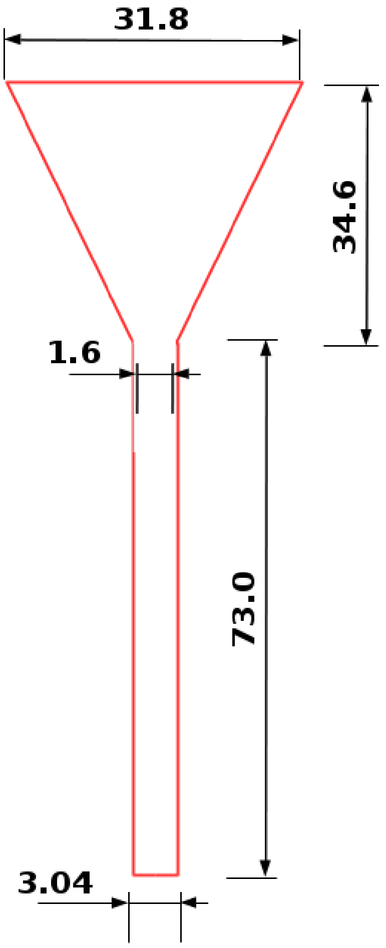

Figure A.3: A schematic view of the (measured) glass funnel dimensions that was used to collimate dust grains as discussed in Sec. (4.2.1). All dimensions are given in units of millimeters.

Appendix B

Solution derivation for a falling grain with neutral gas drag

The equation of motion for an isolated falling dust grain according to the force diagram in Fig. (4.6) is

$$m_{\mathrm{d}}\frac{dv_{\mathrm{y}}}{dt} = -m_{\mathrm{d}}g - \gamma v_{\mathrm{y}} \tag{B.1}$$

where m_{d} is the mass of the grain, $v_{\mathrm{y}} = v_{\mathrm{y}}(t)$ is the velocity of the grain, g is the gravitational acceleration, and γ is the constant Epstein drag coefficient. By Dividing Eq. (B.1) by m_{d}, defining $\Gamma = \gamma/m_{\mathrm{d}}$, the equation of motion becomes:

$$\frac{dv_{\mathrm{y}}}{dt} = -g - \Gamma v_{\mathrm{y}}. \tag{B.2}$$

Eq. (B.2) is a first-order separable differential equation. Each side can be separated and integrated as follows:

$$\int_{v_{\mathrm{o}}}^{v} \frac{dv_{\mathrm{y}}}{\Gamma v_{\mathrm{y}} + g} = -\int_{t_{\mathrm{o}}}^{t} dt \tag{B.3}$$

$$\frac{1}{\Gamma}\ln\left(\frac{\Gamma v_{\mathrm{y}} + g}{\Gamma v_{\mathrm{o}} + g}\right) = -(t - t_{\mathrm{o}}) \tag{B.4}$$

where v_{o} is the initial velocity at the initial time t_{o}. Exponentiate both sides of Eq. (B.4) and solve for v_{y} to show that

$$v_{\mathrm{y}}(t) = \frac{1}{\Gamma}(\Gamma v_{\mathrm{o}} + g)\exp\left(-\Gamma(t - t_{\mathrm{o}})\right) - \frac{g}{\Gamma}. \tag{B.5}$$

Recall that $v_{\mathrm{y}} = dy/dt$ and hence Eq. (B.5) can be integrated once more to obtain the general solution to Eq. (B.2):

$$y - y_{\mathrm{o}} = -\frac{1}{\Gamma^2}(\Gamma v_{\mathrm{o}} + g)\exp(-\Gamma(t - t_o)) - \frac{g}{\Gamma}(t - t_{\mathrm{o}}) \tag{B.6}$$

where y_{o} is the initial position at the initial time t_{o}.

Appendix C

Solution derivation for a $\mathbf{g} \times \mathbf{B}$ drifting grain with neutral gas drag

The equation of motion for a dust grain according to the force diagram in Fig. (2.4a) is given by the following coupled system of equations:

$$m_{\mathrm{d}} \frac{dv_{\mathrm{x}}}{dt} = q_{\mathrm{d}} B_{\mathrm{z}} v_{\mathrm{y}} - \gamma v_{\mathrm{x}} \tag{C.1}$$

and

$$m_{\mathrm{d}} \frac{dv_{\mathrm{y}}}{dt} = -q_{\mathrm{d}} B_{\mathrm{z}} v_{\mathrm{x}} - \gamma v_{\mathrm{y}} - m_{\mathrm{d}} g \tag{C.2}$$

where m_{d} is the mass of the dust grain, $v_{\mathrm{x}} = v_{\mathrm{x}}(t)$ and $v_{\mathrm{y}} = v_{\mathrm{y}}(t)$ are the horizontal and vertical velocities, q_{d} is the dust grain charge, B_{z} is the magnetic field strength, γ is the constant Epstein drag coefficient, and g is the gravitational acceleration. Dividing Eqs. (C.1 – C.2) through by m_{d} and defining $\omega_{\mathrm{d}} = -q_{\mathrm{d}} B_{\mathrm{z}} / m_{\mathrm{d}}$, the system of equations above can be written as:

$$\frac{d}{dt} \begin{pmatrix} v_{\mathrm{x}} \\ v_{\mathrm{y}} \end{pmatrix} = \begin{pmatrix} -\Gamma & -\omega_{\mathrm{d}} \\ \omega_{\mathrm{d}} & -\Gamma \end{pmatrix} \begin{pmatrix} v_{\mathrm{x}} \\ v_{\mathrm{y}} \end{pmatrix} + \begin{pmatrix} 0 \\ -g \end{pmatrix}. \tag{C.3}$$

Eq. (C.3) is a non-homogeneous linear first order system of coupled ODE's that can be expressed more concisely as:

$$\frac{d\mathbf{v}}{dt} = \mathbf{A} \cdot \mathbf{v} + \mathbf{F}_{\mathrm{o}} \tag{C.4}$$

where

$$\mathbf{A} = \begin{pmatrix} -\Gamma & -\omega_{\mathrm{d}} \\ \omega_{\mathrm{d}} & -\Gamma \end{pmatrix}, \tag{C.5}$$

$$\mathbf{F}_{\mathrm{o}} = \begin{pmatrix} 0 \\ -g \end{pmatrix}, \tag{C.6}$$

and

$$\mathbf{v} = \begin{pmatrix} v_{\mathrm{x}} \\ v_{\mathrm{y}} \end{pmatrix}. \tag{C.7}$$

Eq. (C.4) can be solved using the standard techniques of ordinary differential equations such as those found in [155]. We start by considering only the following homogeneous system:

$$\frac{d\mathbf{v}_{\mathrm{h}}}{dt} = \mathbf{A} \cdot \mathbf{v}_{\mathrm{h}}. \tag{C.8}$$

The first step in solving Eq. (C.8) is to consider the following eigen-system:

$$(\mathbf{A} - \lambda \mathbf{I}) \cdot \eta = 0 \tag{C.9}$$

where λ are the eigenvalues and η are the eigenvectors. We solve Eq. (C.9) by finding the characteristic equation and solving for its roots. The characteristic equation is:

$$|\mathbf{A} - \lambda \mathbf{I}| = (\Gamma + \lambda)^2 + \omega_{\mathrm{d}}^2 = 0 \tag{C.10}$$

and its corresponding roots (i.e. the eigenvalues) are

$$\lambda_{\pm} = -\Gamma \pm i\omega_{\mathrm{d}}. \tag{C.11}$$

The presence of *real* and *imaginary* components of the roots indicate that, as expected, there is a damped oscillation. The imaginary term corresponds to oscillations (i.e. the usual Larmor motion) whereas the real component corresponds to damped motion (i.e. the neutral drag). The first eigenvector, η_+, is calculated by back substituting the root, λ_+, into

Eq. (C.9) and then solving the corresponding homogeneous system to obtain the following:

$$\eta_+ = \begin{pmatrix} i \\ 1 \end{pmatrix}. \tag{C.12}$$

The partial solution to Eq. (C.8) from the first eigenvalue and eigenvector is:

$$\mathbf{v}_+(t) = \exp(-\Gamma t + i\omega_\mathrm{d} t) \begin{pmatrix} i \\ 1 \end{pmatrix} \tag{C.13}$$

When the coefficient matrix, Eq. (C.5), is real and the eigenvalues, Eq. (C.11), occur on a conjugate pair, such as the case presented here, the solution to the homogeneous system, Eq. (C.8), can now be obtained directly using only the first eigenvector and its corresponding solution by separating the *real* and *imaginary* components of the v_+ eigenvector such that

$$\mathbf{v}_+(t) = \mathbf{a}(t) + i\mathbf{b}(t). \tag{C.14}$$

When the *real* and *imaginary* components of Eq. (C.13) are separated according to Eq. (C.14), the general solution to the original homogeneous equation for the velocity of the falling grain, Eq. (C.8), can be written as the following linear combination:

$$\mathbf{v}_\mathrm{h}(t) = C_1\mathbf{a}(t) + C_2\mathbf{b}(t) \tag{C.15}$$

Applying Euler's formula to Eq. (C.13) to isolate the real and imaginary components gives:

$$\mathbf{a}(t) = \exp(-\Gamma t) \begin{pmatrix} -\sin(\omega_\mathrm{d} t) \\ \cos(\omega_\mathrm{d} t) \end{pmatrix} \tag{C.16}$$

and

$$\mathbf{b}(t) = \exp(-\Gamma t) \begin{pmatrix} \cos(\omega_{\mathrm{d}} t) \\ \sin(\omega_{\mathrm{d}} t) \end{pmatrix} \tag{C.17}$$

so that

$$\mathbf{v}_h(t) = C_1 \exp(-\Gamma t) \begin{pmatrix} -\sin(\omega_{\mathrm{d}} t) \\ \cos(\omega_{\mathrm{d}} t) \end{pmatrix} + C_2 \exp(-\Gamma t) \begin{pmatrix} \cos(\omega_{\mathrm{d}} t) \\ \sin(\omega_{\mathrm{d}} t) \end{pmatrix}. \tag{C.18}$$

In summary, for the homogeneous solution (i.e., the absence of external forces such as gravity), the velocities exponentially decay to zero. For the limiting case, where neutral drag is removed such that $\Gamma = 0$, we get the expected oscillating Larmor motion solutions for a charged particle oscillating in an external magnetic field.

Now that the homogeneous solution to Eq. (C.4) has been found, the final step is to find the particular solution. In order to find the particular solution, using the usual method of solving ODE's, we guess a particular solution of the form:

$$\mathbf{v}_p(t) = \mathbf{u}_{\mathrm{o}} + t\mathbf{w}_{\mathrm{o}} \tag{C.19}$$

where $\mathbf{u}_{\mathrm{o}}$ and $\mathbf{w}_{\mathrm{o}}$ are constant vectors and t time. We differentiate Eq. (C.19) according to Eq. (C.4) and get the following:

$$\frac{d\mathbf{v}_{\mathrm{p}}}{dt} = \mathbf{A} \cdot \mathbf{v}_{\mathrm{p}} + \mathbf{F}_{\mathrm{o}} = \mathbf{w}_o = \mathbf{A} \cdot \mathbf{u}_{\mathrm{o}} + t\mathbf{A} \cdot \mathbf{w}_{\mathrm{o}} + \mathbf{F}_{\mathrm{o}}. \tag{C.20}$$

Collecting like-terms and rearranging them all on the LHS gives:

$$t[\mathbf{A} \cdot \mathbf{w}_{\mathrm{o}}] + [\mathbf{A} \cdot \mathbf{u}_{\mathrm{o}} - \mathbf{w}_o + \mathbf{F}_{\mathrm{o}}] = 0. \tag{C.21}$$

Referring back to Eq. (C.5), in order for Eq. (C.21) to be true for all values of t, each term in square brackets ([...]) must vanish identically. Consider the first term on the RHS side:

$$t[\mathbf{A} \cdot \mathbf{w}_{\mathrm{o}}] = 0 \tag{C.22}$$

In order for the above equation to be true, we require that the determinant of $\mathbf{A}$ must vanish, $|\mathbf{A}| = \Gamma^2 - \omega_{\mathrm{d}}^2 = 0$. In general, this is not the case. Therefore, we can conclude that $\mathbf{w}_o = 0$ (meaning that $\mathbf{A}$ is a nonsingular matrix). The second term on the LHS of Eq. (C.21) is now:

$$[\mathbf{A} \cdot \mathbf{u}_{\mathrm{o}} + \mathbf{F}_{\mathrm{o}}] = 0 \tag{C.23}$$

Eq. (C.23) is the 2-dimensional system of equations:

$$\begin{pmatrix} \Gamma & \omega_{\mathrm{d}} \\ \omega_{\mathrm{d}} & -\Gamma \end{pmatrix} \begin{pmatrix} u_{\mathrm{o,x}} \\ u_{\mathrm{o,y}} \end{pmatrix} = \begin{pmatrix} 0 \\ -g \end{pmatrix} \tag{C.24}$$

with a solution of

$$u_{\mathrm{o,x}} = \frac{g}{\omega_{\mathrm{d}}(1 + \Gamma^2/\omega_{\mathrm{d}}^2)} \tag{C.25}$$

and

$$u_{\mathrm{o,y}} = -\frac{\frac{\Gamma}{\omega_{\mathrm{d}}} g}{\omega_{\mathrm{d}}(1 + \Gamma^2/\omega_{\mathrm{d}}^2)} \tag{C.26}$$

Combining the particular solution with the homogeneous solution, we get:

$$\begin{aligned} \mathbf{v}(t) = D_1 \exp(-\Gamma t) \begin{pmatrix} -\sin(\omega_{\mathrm{d}} t) \\ \cos(\omega_{\mathrm{d}} t) \end{pmatrix} &+ D_2 \exp(-\Gamma t) \begin{pmatrix} \cos(\omega_{\mathrm{d}} t) \\ \sin(\omega_{\mathrm{d}} t) \end{pmatrix} \\ &+ \frac{g}{\omega_{\mathrm{d}}(1 + \Gamma^2/\omega_{\mathrm{d}}^2)} \begin{pmatrix} 1 \\ -\Gamma/\omega_{\mathrm{d}} \end{pmatrix}. \end{aligned} \tag{C.27}$$

The arbitrary constants, D_1 and D_2 are set by the initial conditions of the falling particle.

Appendix D

Diagram of the flood fill technique

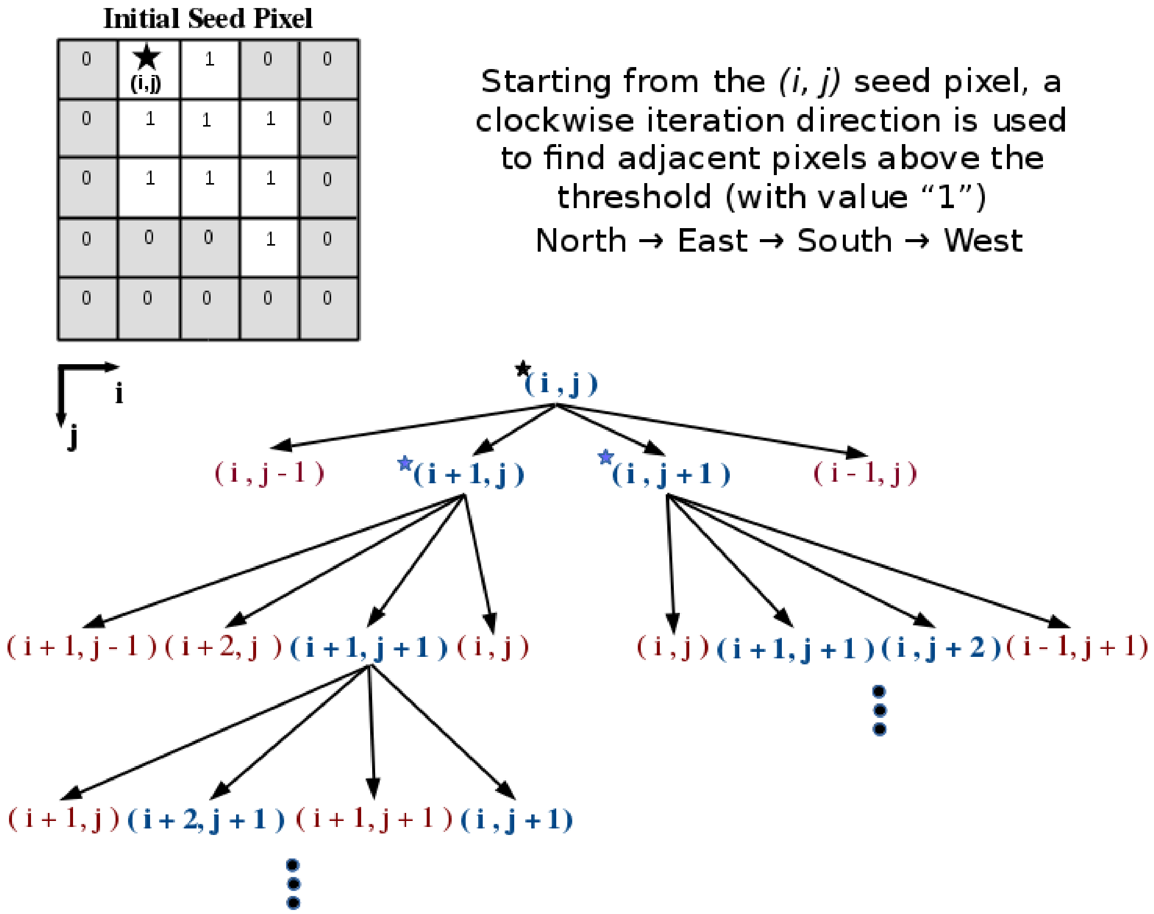

Initial Seed Pixel

0	★ (i,j)	1	0	0
0	1	1	1	0
0	1	1	1	0
0	0	0	1	0
0	0	0	0	0

Starting from the *(i, j)* seed pixel, a clockwise iteration direction is used to find adjacent pixels above the threshold (with value "1")

North → East → South → West

Figure D.1: An illustration of the flood fill technique. All pixels above the intensity threshold are labeled with a 1 (i.e., True). All pixels below the intensity threshold are labeled with a 0 (i.e., False). The black star located at pixel (i, j) marks the seed pixel. Starting from the seed pixel, all local neighbors (north, east, south, and west) are examined to see if their intensity is above the threshold. If above the threshold, the pixels are added to a stack data structure. In this example, the east and south pixels are above the threshold and are marked by blue stars and text in the tree diagram. In the next step, the algorithm chooses a pixel location (i.e., the locations marked by blue stars) from the stack data structure and then examines that pixel's local neighbors to see if they satisfy the threshold condition. In this way, the flood-fill algorithm iterates until the stack is empty and all connected pixels above the intensity threshold are found.